ABSTRACT

CRINER, AMANDA KECK. Nondestructive Evaluation of Porous Materials. (Under the direction of H. T. Banks.)

We report here on the use of the heat equation to simulate a thermal interrogation method for detecting damage in a heterogeneous porous material. We first use probability schemes to randomly generate pores in a sample material; then we simulate flash heating of the compartment along one of its boundaries. Temperature data along the source and back boundaries are recorded and then analyzed to distinguish differences between the undamaged and damaged materials. These results suggest that it is possible to detect damage of a certain size within a porous medium using thermal interrogation.

We discuss a mathematical model for the flash heat experiment in homogeneous isotropic media. We then use this model to investigate the use of homogenization techniques in approximating models for interrogation via flash-heating in porous materials. We represent porous materials as both randomly perforated domains and periodically perforated domains.

In this effort, we investigate the behavior of a model derived from homogenization theory as the model solution in parameter estimation procedures for simulated data. We consider data simulated from a model on a perforated domain with isotropic flow and data simulated from a model on a homogeneous domain with anisotropic flow. We consider both ordinary and generalized least squares parameter estimation procedures.

We then use these methodologies along with a method of maps to detect damage using a hypothesis test. Finally, we consider using the homogenization approximation to characterize elliptical damage.

Nondestructive Evaluation of Porous Materials

by
Amanda Keck Criner

A dissertation submitted to the Graduate Faculty of
North Carolina State University
in partial fulfillment of the
requirements for the Degree of
Doctor of Philosophy

Applied Mathematics

Raleigh, North Carolina

2011

APPROVED BY:

_____   _____
Mansoor Haider   Robert Martin

_____   _____
Ralph Smith   H. T. Banks
                                                    Chair of Advisory Committee

BIOGRAPHY

Amanda Keck Criner was raised with her brother Ryan George Criner by their parents George and Francie Criner in Maine. She graduated from the University of Maine under the advisement of Dr. David Hiebeler in 2007. She began the Ph.D. program in Applied Mathematics at North Carolina State University under the advisement of Dr. H.T. Banks.

ACKNOWLEDGEMENTS

There have been so many blessings in my life that to acknowledge them all would be a trilogy. Here, I will present the summary. First, I would like to thank Dr Banks for his mentorship. He has given knowledge, care and patience very graciously to me. I have learned a lot about mathematics, statistics and people (including myself) from him.

Many other teachers and advisors have helped me. My advising committee Dr Haider, Dr Martin and Dr Smith have taught me so much. They have also been very patient, understanding and encouraging. Other teachers have helped throughout my life. Dr Hiebeler gave me the first opportunity to do research, insisted that I learned how to program well, and gave me insight into the research process. Dr Chavez encouraged me to go to graduate school, and through his program I learned about mathematical biology. Sharon Crook encouraged me to pursue mathematics in my undergraduate education. Other teachers that have helped me significantly have been Tad Johnson, V.K. Balakrishnan, and Sergey Lvin.

My mother, father and brother have always been a source of love, comfort, encouragement, and entertainment. I do not know how I could smile so much without them and have missed them while I have been working on my Ph.D. at North Carolina State University.

I would also like to thank Grandma Mary Frances, Aunt Florence, Uncle Wayne, cousins Matthew and Luke, Aunt Dee, Uncle Dan, Grandpa, Randi, Grandma Ruth and Opa, cousins Liz, Bob, Lara, Willie, Dustin, and Austin.

I have also had very many friends and colleagues that have helped me in my life and education including Bonnie, Milos, Heather, Jessie, Kit, Brittany, Heidi, Caitlin, Emma, Deena, Anne, Catherine, Karyn, Ariel, Krista, Garret, Thom, Clay, Keri, Zack, Adam,

Matt-Matt, Erin, Jim Young, Steve Smith, Matt-Joe, Steve Hickle, Cerena and Sean.

There are also the dogs that have helped me not throw computers out of windows and not lose my mind just by being cute. Frisky I still miss and Mr. Rosco is a joy every day.

All of these blessings are thanks to the Grace and Love of God and his Son Jesus Christ. I pray that I can take these gifts of love and grace and give them away.

TABLE OF CONTENTS

LIST OF TABLES

LIST OF FIGURES

Chapter 1

Intoduction

Nondestructive evaluation (NDE) is a very useful tool that enjoys widespread use in testing structures, especially as they age beyond their design life. Proper use of NDE can increase the safety and service life of components in aircraft, spacecraft, automobiles, trains, and piping. There are numerous viable NDE methods including ultrasound, magnetic particle imaging, eddy current, acoustic emission, and radiology to mention a few [27]. These techniques have been developed in a large number of applications, particularly for homogeneous metallic materials [10]–[11]. Composite materials are lighter and stronger than metallic materials so they are increasingly popular in many structures. Composite materials are made with an acceptable level of porosity. This porosity causes a certain amount of noise in the interrogation signal of any NDE technique. These materials are used in many critical structures including aeronautical and aerospace vehicles, so there is a need to develop and evaluate NDE techniques for these materials [21, 31].

Active thermography is a particularly appropriate technique for materials with significant porosity. Active thermography measures the spatial and temporal evolution of the surface temperature following an input heat flux to detect subsurface anomalies.

This evolution is a result of heat diffusion in the material. Since heat diffuses around porosity, rather than strongly interacting with it, thermography is able to detect large anomalies deep in a porous material. Additional advantages of thermal NDE are that it is a single sided, noncontacting and a large area technique making in-service evaluation feasible. It is also possible to embed temperature sensors in the material [28] for continuous structural heath monitoring. We treat here the problem of thermal NDE in porous materials.

We describe a mathematical model for thermal transport in a two dimensional (2-D) porous material domain in Chapter 2. Using ideas based on the efforts in [13], we generate families of porous sample domains through various random geometry schemes. We also discuss methods for generation of these geometries Section 2.2. We then discuss briefly the numerical solutions and convergence of the numerical solutions of the model on such domains in Section 2.3. In Section 2.4 we report on subsequent use of the random geometry schemes with added damage due to oxidation of increasing sizes to the sample. For samples with and without damage due to oxidation, we carried out simulations to compare the resulting temperature profiles in space and time at both the source and back boundary. These methods are too computationally intensive to use in the sophisticated parameter estimation routines needed to characterize damage. After examining the results of these simulations, we go on to use these methods in Chapters 3–5 to generate data.

We then investigate a less computationally intensive model in Chapter 3 which is derived from the results of homogenization theory. We consider a more general version of the heat equation, relaxing the assumption of no heat loss on the boundaries and the assumption that there is no heat loss in the direction orthogonal to the two dimensional sample. We further discuss the finite element method, which is used to solve all of the

2

partial differential equations in this document. We also discuss the procedures used in homogenization to approximate the flow of heat over a domain with random pores by the flow of heat over a domain with many periodically placed pores. One passes this periodic domain to a limit using homogenization theory [16]–[23] to gain a limit partial differential equation which replaces the periodically perforated domain with a homogeneous domain that has *anisotropic* flow which approximates the effect of the porosity. With the results of homogenization theory developed in Section 3.3 we then summarize and compare the results of simulations of the flash heat experiment on a randomly perforated domain, a periodically perforated domain, and a homogeneous domain with the anisotropic flow derived from homogenization theory in Section 3.4. We also graphically analyze example simulations in Section 3.4.

Though the results of Chapter 3 are encouraging, the behavior of an approximation in the forward problem is not necessarily indicative of the behavior of the approximation in inverse problems. Also, in Chapters 2 and 3, we did not consider random error which is often associated with experimental data. In Chapter 4 we discuss the results from performing the inverse problem using the mathematical models developed in Chapters 2 and 3, and parameter estimation procedures discussed and developed in [7], [22] on simulated data. We consider data simulated with absolute error in Section 4.2 and relative error in Section 4.3. This first investigation of parameter estimation procedures focuses on estimating parameters in the partial differential equations. Though this is an important part of characterizing abnormalities, we must estimate domain parameters (the geometry of the domain on which the partial differential equation is solved) to characterize damage. Based on the results of Chapter 4, we go on to estimate parameters which determine elliptical damages (meant to represent damage due to oxidation) in Chapter 5.

In Chapter 5, we use the methods described in Chapters 2–4 to simulate data. We then

analyze this data in a damage detection problem using a hypothesis test in Section 5.2. In Section 5.3, we consider characterizing elliptical damage by estimating the location of the center of the ellipse and its vertical and horizontal semi-axes lengths.

Chapter 2

Heat Equation on Porous Domains

2.1   Flash heat experiment on a perforated domain

In this chapter we will model the 2-D problem as a proof of concept. Our 2-D geometries represent a small slice of a 3-D specimen as a rectangle with elliptical pores, as described in Section 2.2. We model thermal diffusion as the sample is heated along an edge for a short time with a laser or flash lamp on the front boundary, which we will refer to as the source boundary. We record the temperature on both the source boundary and the boundary opposite the source boundary (referred to as the back boundary) during and after the heating.

We examine a 2 mm × 1 mm rectangle $\hat{\Omega} = \{(x, y)|0 \leq x \leq L_1, 0 \leq y \leq L_2\} = [0, 2] \times [0, 1]$ with randomly placed pores. Let Ω denote the rectangle minus n_r pores, which are given by $\Omega_1, \Omega_2, \ldots \Omega_{n_r}$. The domain of interest is then $\hat{\Omega} = \Omega \cup (\cup_{i=1}^{n_r} \Omega_i)$. The exterior boundary of Ω has 4 edges, which we denote by ω_j where $j=1, \ldots, 4$; thus $\partial\hat{\Omega} = \cup_{j=1}^{4} \omega_j$. It is assumed that each pore Ω_i has a smooth boundary with Ω given by $\partial\Omega_i$, as depicted in Figure 2.1.
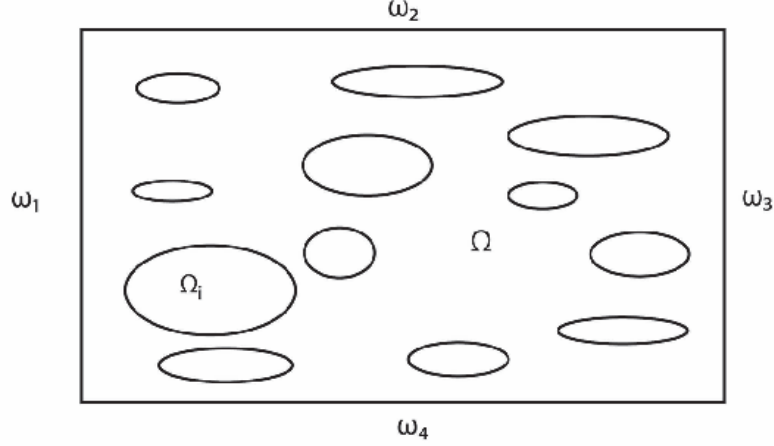
Figure 2.1: A typical example of a 2-D specimen

The 2-D heat diffusion equation, which describes heat as it diffuses through a region, is based on Fourier's law and is given [14, 24] by

$$\rho(x,y)c_p(x,y)\frac{\partial u(t,x,y)}{\partial t} = \nabla \cdot (k(x,y)\nabla u(t,x,y)). \tag{2.1}$$

Here $u(t,x,y)$ is the temperature, $\rho(x,y)$ is the material density of the sample, $c_p(x,y)$ is the specific heat of the material, and $k(x,y)$ is the thermal conductivity. In materials with particles, rather than pores, the thermal conductivity is typically piecewise defined as

$$k(x,y) = \begin{cases} k_p, & (x,y) \in \Omega_i, i = 1, \ldots n_r, \\ k_m, & (x,y) \in \Omega, \end{cases} \tag{2.2}$$

where k_p denote the thermal conductivity of the pores and k_m denote that of the material as in [13]. In many applications, the assumption that there is zero flux across the pores or particles is a very good approximation. Throughout this document, we will be making

6

this assumption. We will now denote Ω_i as perforations and c_p, ρ, and k as the material properties specific heat, density and thermal conductivity of the domain Ω.

We will use finite element solutions which may be derived in several different ways including Galerkin methods. We will discuss the Galerkin derivation of these methods in Section 3.2 which are based on a variational or weak formulation. In this section, we will focus on the physical derivation and motivation for this formulation. These models have been used in detecting damage in many examples including [11].

Consider test functions $\phi \in H^1(\Omega)$, in an integrated form of (2.1) given by

$$\int_\Omega c_p \rho \frac{\partial u}{\partial t} \phi(x,y) dA = \int_\Omega \phi(x,y) \nabla \cdot (k \nabla u) dA. \tag{2.3}$$

We use Green's first identity to obtain

$$\int_\Omega c_p \rho \frac{\partial u}{\partial t} \phi(x,y) dA$$

$$= \sum_{j=1}^{4} \left(k \int_{\omega_j} \phi(x,y)(\nabla u \cdot \vec{n}) ds \right) - k \int_\Omega \nabla u \cdot \nabla(\phi(x,y)) dA \tag{2.4}$$
$$+ k \sum_{i=1}^{n_R} \left(\int_{\partial \Omega_i} \phi(x,y)(\nabla u \cdot \vec{n}) ds \right),$$

where as convention $\vec{n}$ refers to the unit exterior normal. Again using the zero flux assumptions on the pore boundaries, the term

$$k \sum_{i=1}^{n_r} \left(\int_{\partial \Omega_i} \phi(x,y)(\nabla u \cdot \vec{n}) ds \right) = 0.$$

7

Combining the three remaining terms from (2.4), we find

$$
\begin{aligned}
\int_{\hat{\Omega}} c_p \rho \frac{\partial u}{\partial t} \phi(x,y) dA \\
= \sum_{j=1}^{4} \left(k \int_{\omega_j} \phi(x,y)(\nabla u \cdot \vec{n}) ds \right) - \int_{\Omega} k \nabla u \cdot \nabla \phi(x,y) dA.
\end{aligned}
\tag{2.5}
$$

Excluding the source boundary, we assume an insulated rectangle so that $\nabla u = 0$ on the boundaries $\omega_1, \omega_2,$ and ω_3. The ω_4 or source boundary, which consists of the region $\{(x,0)|0 \le x \le L_1\}$, acts as a source for an initial period and is subsequentially insulated. We represent the corresponding boundary condition with the characteristic function

$$
k \nabla u \Big|_{\omega_4} = S_0 \mathcal{I}_{[t_0,t_s]}(t) =
\begin{cases}
S_0, & t \in [t_0, t_s] \\
0, & \text{otherwise.}
\end{cases}
\tag{2.6}
$$

Thus we have

$$
\int_{\hat{\Omega}} c_p \rho \frac{\partial u}{\partial t} \phi \, dA = \int_0^{L_1} \phi(x,0) S_0 \mathcal{I}_{[t_0,t_s]}(t) \, dx - \int_{\hat{\Omega}} k \nabla u \cdot \nabla \phi \, dA.
\tag{2.7}
$$

This weak formulation is employed in the MATLAB Partial Differential Equation Toolbox (PDE toolbox) to derive the numerical solutions to the system (a finite element method); we consider this method and its convergence in Section 2.3.

The classical partial differential equation which is equivalent to (2.7) in some cases

and which we will use throughout is the given by

$$
\begin{cases}
c_p \rho \dfrac{\partial}{\partial t} u - k \Delta u = 0 & \text{in } \Omega \\[2mm]
k \dfrac{\partial}{\partial \eta} u = 0 & \text{on } \cup_{i=1}^{n_r} \partial \Omega_i \\[2mm]
k \dfrac{\partial}{\partial \eta} u = 0 & \text{on } \cup_{i=1}^{3} \omega_i \\[2mm]
k \dfrac{\partial}{\partial \eta} u = S_0 \mathcal{I}_{0,t_s}(t) & \text{on } \omega_4,
\end{cases}
\tag{2.8}
$$

where $\dfrac{\partial}{\partial \eta} u$ denotes the external unit normal or $\vec{n} \cdot \nabla u$. The solution u of (2.8) is unique in $H^1(\Omega)$.

2.2 Generation of Random Geometries

A major component of the effort reported on here involves generation of domains with randomly placed pores of different sizes as depicted in Figure 2.1 and Figures 2.3-2.6. We concentrated our efforts on elliptical shaped pores with semi-major axes in the horizontal (x) direction. This was motivated by visual inspection of material samples at NASA as depicted in Figure 2.2.

We model porosity by randomly placing pores in an $L_1 = 2$ mm by $L_2 = 1$ mm rectangle $\hat{\Omega} = [0,2] \times [0,1]$ employing ideas developed in [13]. The pores are ellipses to represent voids in a two-dimensional slice of any piece of porous material. For simplicity in algorithm development, we began carrying out our simulations with circles (see [4] and [3] for discussions) but subsequently used ellipses for more realistic representations. Even though pores coalesce when they intersect physically, we assume that the pores do not overlap with each other or the boundaries of the rectangular compartment (more

9
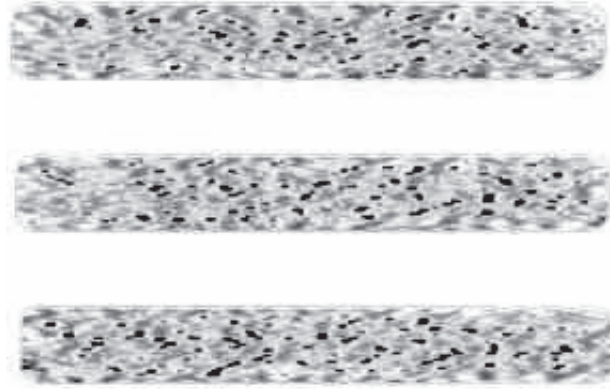
Figure 2.2: An example of a porous specimen.

irregular shapes in pores could be achieved by allowing overlaps). To do this, in our algorithms we first generate a pore using one of the probability schemes described below. The pore is then placed in the compartment if it does not overlap with an existing pore, and rejected if it does. Another pore is then randomly selected as described below, etc., until the desired porosity of the material is achieved. We considered several different distributions for generating the horizontal and vertical semi axes. We found that the temperature is not very sensitive to the choice of distribution with the number of pores and level of porosity that we consider. It is very important to note here that the results given in [30] are essential in determining wheter or not two ellipses intersect.

To simulate pore-like damages due to oxidation, we first generate one unusually large ellipse (see Section 2.4 for examples) to represent damage and then place pores using the algorithm described above. When generating various elliptical damages, the center was an input. The semi-major axis for damage was taken as an input, and the semi-minor axis was calculated so as to maintain a constant ratio between the two axes as we chose damages of different sizes.

Table 2.1: Parameter values

Heat transfer coefficient	S_0	$3.3 \times 10^{-3} \frac{\text{J}}{\text{mm}^2}$
Material thermal conductivity	k	$3.5 \times 10^{-3} \frac{\text{J}}{\text{mmK sec}}$
Heat capacity	c_p	$0.75 \frac{\text{J}}{\text{g K}}$
Density	ρ	$1.6 \times 10^{-3} \frac{\text{g}}{\text{mm}^3}$

2.3   Numerical Solutions

After generating a particular geometry, we solved the heat equation (2.7) using PDE Toolbox with the parameters summarized in Table 2.1.

As already noted, three of the compartment's four sides are insulated and defined by Neumann boundary conditions where heat flux is zero. The source boundary has a heat transfer coefficient of $3.3 \times 10^{-3} \dfrac{\text{J}}{\text{mm}^2}$ during flash heating and zero flux later. There is also zero heat flux on the boundaries between the material and the pores represented as perforations. PDE Toolbox creates a mesh using the Delaunay triangulation algorithm; see [25] for details.

We validated the convergence of PDE Toolbox's numerical solution and sensitivity to changes in the randomness in the porous domain by taking the supremum norm of the difference in source boundary temperatures after successive mesh iterations with 30 random geometries for each of the percent porosities 2%, 5% and 10% investigated. Example results for 2% porosity are given in Table 2.2 (similar tables for examples with 5% and 10% porosity can be found in [4] and [3]). At 2% porosity, 0.04 K in precision is gained by quadrupaling the number of mesh points, and tripling the amount of time to mesh, as seen in Table 2.2. We see similar increases in number of points and

11

Table 2.2: The average values (evaluated on 30 random geometries with 2% porosity) of: absolute error $||u_{i+1} - u_i||_\infty$, relative error $\dfrac{||u_{i+1} - u_i||_\infty}{||u_i||_\infty}$, number of mesh points, and the amount of time to generate the mesh. **Note**: u_i indicates the ith mesh iteration.

		Means		
Mesh Iteration	Absolute Error (K)	Relative Error	# of Mesh Points	Time(s)
1	0.059	7.89×10^{-4}	7500	42.0
2	0.019	6.70×10^{-5}	29639	87.1
3			118424	303.9
		Standard deviations		
1	0.0020	6.74×10^{-6}	410	4.4
2	0.0008	2.31×10^{-4}	7535	3.4
3			5676	25.0

computational time to mesh at 5% and 10%, but the precision gained is 0.1 K and 0.2 K, respectively. In all of the reported computations, in this chapter, in [3] and in [4], we refine the mesh once.

2.4 Simulations

We generated numerous samples with varying levels of porosity including 2%, 5% and 10% and with a single damage of varying size located near the source surface, the back surface or mid sample. A large number of results for simulations with these geometries are given in [3].

We present here a sampling of graphical results from [3]. Each group of figures below depicts a compartment both with and without damage and the corresponding
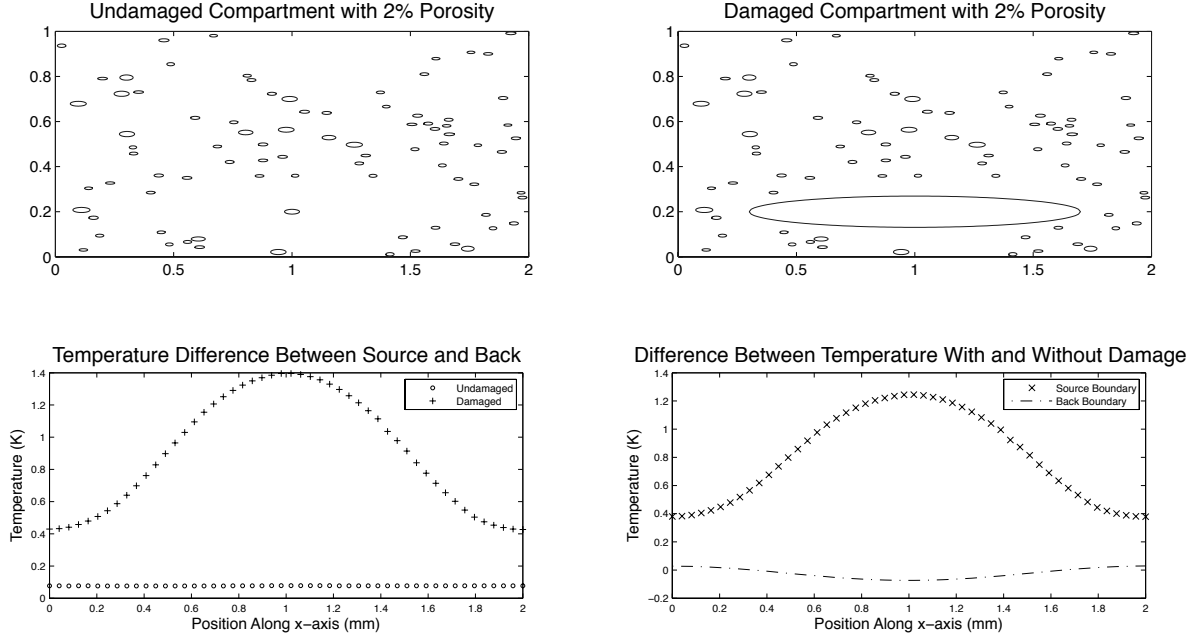
Figure 2.3: Sample with 2% porosity, damage centered at $(1, 0.2)$, semi-major axis $a = 0.7$ mm, semi-minor axis $b = 0.0692$ mm.

temperature profiles. Observe that the pores surrounding the damage are identical to those in the undamaged compartment. In every case, we heat the source boundary for 0.6 seconds ($t_s = 0.6$) and record the temperature a total of 1.3 seconds (including heating time). Figures 2.3-2.6 present results for samples of varying percent porosity with damages of various size located in different locations.

We observed several general trends in our temperature profile graphs. First, we tracked temperatures at the source and back boundaries so as to shed light on possible sensor placement if options were available. As might be expected, we found that the absolute value of the difference between damaged and undamaged material is greatest at the center of the damage due to oxidation. As shown in Figure 2.3, at a damage width of 1.4 mm due to oxidation, the maximum difference is 1.2 K at the source boundary
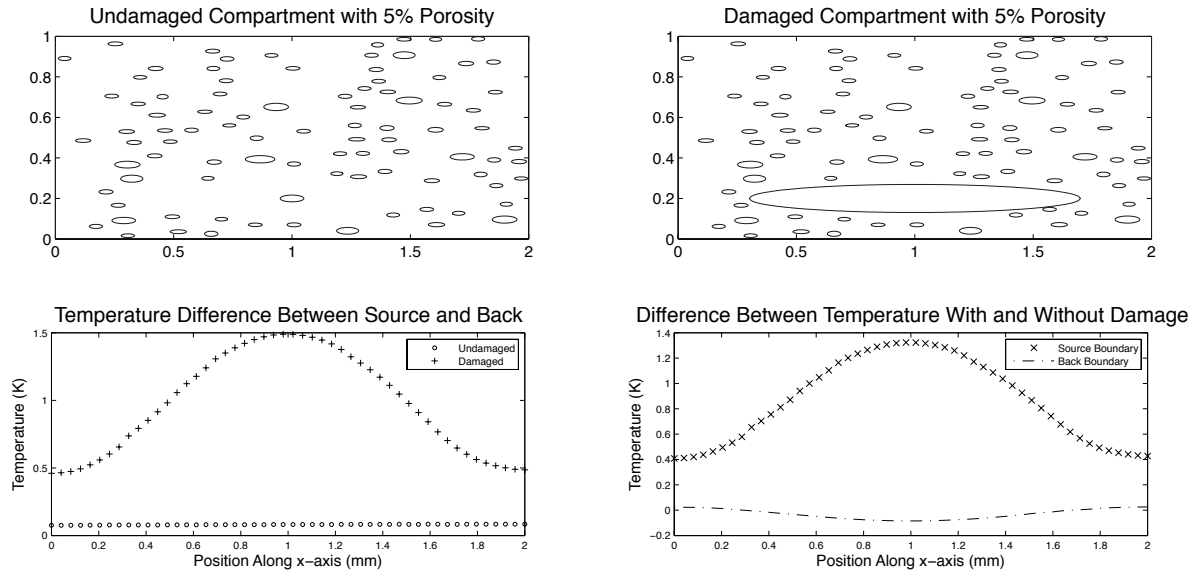
Figure 2.4: Sample with 5% porosity, damage centered at $(1, 0.2)$, semi-major axis $a = 0.7$ mm, semi-minor axis $b = 0.0692$ mm.
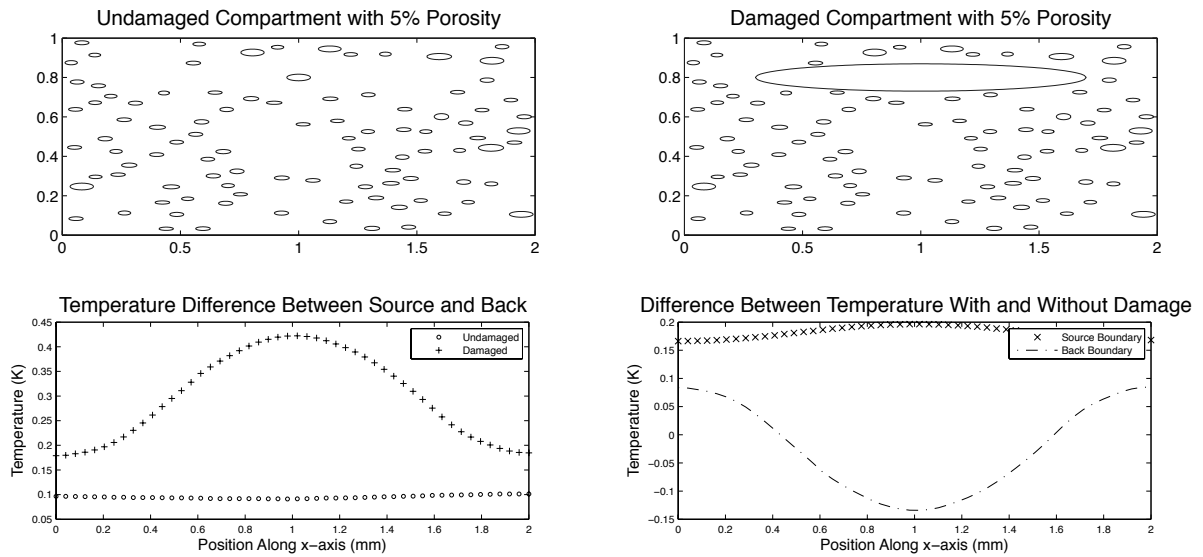
Figure 2.5: Sample with 5% porosity, damage centered at $(1, 0.8)$, semi-major axis $a = 0.7$ mm, semi-minor axis $b = 0.0692$ mm.

14
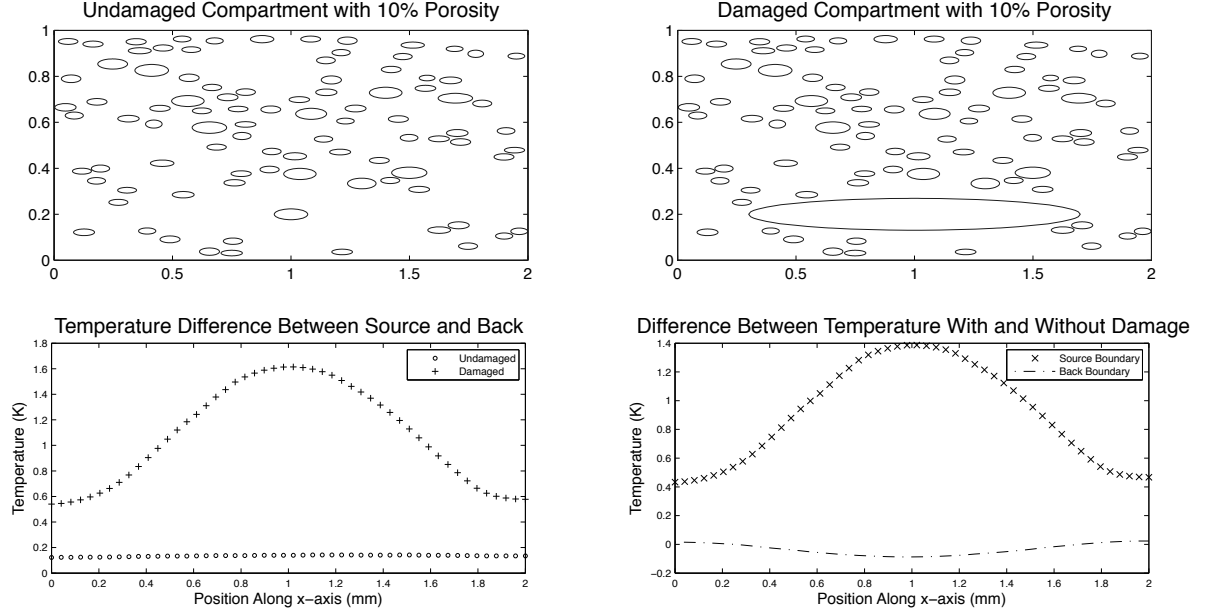
Figure 2.6: Sample with 10% porosity, damage centered at (1, 0.2), semi-major axis $a = 0.7$ mm, semi-minor axis $b = 0.0692$ mm.

and 0.03 K at the back boundary. In Figure 2.4, when the damage width increases to 1.4 mm, the maximum difference is 1.35 K at the source boundary and 0.08 K at the back boundary. At 10% porosity, when the size of the damage is increased to a width of 1.4 mm, we find in Figure 2.6 that maximum temperature difference is 1.4 K at the source boundary and 0.09 K at the back boundary. These observations demonstrate that the maximum temperature difference between damaged and undamaged material at the source boundary is larger than at the back boundary when the damage is placed near the source boundary. We anticipate that with a sensor that has 0.1 K resolution, placed on the source boundary, we will be able to detect 1.4 mm damages due to oxidation in materials with 2, 5, or 10% porosity. With the same sensor placed on the back boundary, we would not expect to be able to detect these damages in any of the materials.

The difference between damaged and undamaged material is greatest at the center of the damage due to oxidation for both the source and back boundary measurements in most of our computations. The source boundary temperature is always higher with damage, whereas the back boundary temperature is lower with damage in most of our computations. When the damage is placed near the source boundary, the absolute value of the temperature difference resulting from the damage is much greater for the source boundary than the back boundary. When the damage is placed at the center of the compartment, the absolute value of the temperature difference is approximately the same for the source and back boundaries. And lastly, when the damage is placed near the back boundary, the absolute value of the temperature difference is much greater for the back boundary than the source boundary. In Figure 2.5, at the same porosity, a damage of width 1.4 mm near the back boundary gives an equal temperature difference. When we consider the change in temperature (the maximum difference minus the minimum difference), however, we are able to determine the location of the damage. When the damage is centered near the back, the change in temperature is 0.22 K for the back boundary and only 0.03 K for the source boundary. As depicted in Figure 2.4, when the damage is centered near the source, the change in temperature at the source is 0.89 K, and 0.11 K for the back boundary. Thus, by comparing sensors at the back surface with those at the source surface, one should be able to discern the depth of the damage if it is of sufficient size.

We also observed two general trends in the temperature vs. time graphs (in results given in [3] but not depicted here). As the size of the damage due to oxidation grows, it takes longer for the system to reach thermal equilibrium. The farther away the damage is from the source boundary, the closer together the source and back boundary temperatures are for both $x = 1$ and $x = 0$.

This method will be used in subsequent chapters to simulate data. Though these results are useful in detecting damage without noise, collected data also includes noise from the measurement procedure. In order to detect damage, in the presence of this type of noise, there must also be a confidence associated with the prediction of data. Beyond detecting damage due to oxidation, we would also like to be able to characterize these kinds of damage. In order to preform both of these tasks, we must preform sophisticated parameter estimation procedures. These require the use of minimization routines in which solutions must be computed many times. These solutions take far too long to use in these procedures. Also, these geometries are not known in the material a priori. Homogenization theory can approximate the flow of heat in a porous material but does not require knowledge of the exact pore locations and size. Homogenization also requires an order of magnitude less time to compute numerical solutions. In the next chapter, we will consider how well the results of homogenization theory approximate the flow of heat over porous domains.

Chapter 3

Homogenization

In this chapter, we consider an approximation derived from homogenization theory for the flash heat experiment in porous materials. This approach approximates the isotropic flow of heat around the pores in the perforated rectangle with anisotropic flow in a homogeneous rectangle. We consider these results for a more general class of flash heat experiment by relaxing the insulation assumptions of the previous chapter. We first develop a flash heat experiment with anisotropic flow on a homogeneous rectangle, then we consider the finite element solutions of these models. After we discuss the solution methods employed, we discuss the homogenization theory as an approximation of models similar to those developed in Chapter 2.

3.1 Flash heat experiment with anisotropic flow

We first recall the system (3.1) which corresponds to the physical flash-heat experiment described in [4]. This experiment assumes that the temperature of the specimen is within the solid state phase and the boundaries are perfectly insulated [26]. We model
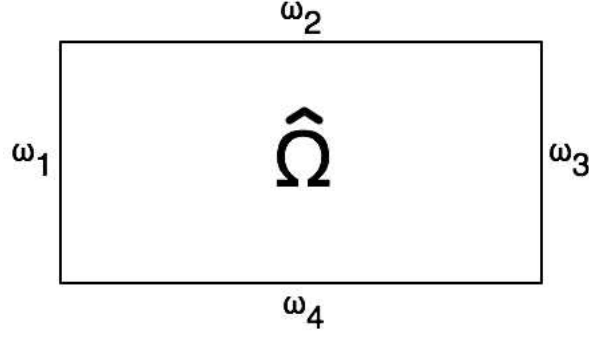
Figure 3.1: The homogeneous rectangle with boundaries.

the flash-heat experiment on an L_2 (length in the y direction) by L_1 (length in the x direction) rectangle during the time interval $t \in (0, T)$ with $T < \infty$. We refer to the L_1 by L_2 rectangle as $\hat{\Omega}$ and the four boundaries ω_i, for $i \in \{1, 2, 3, 4\}$. When referring to the entire boundary of $\hat{\Omega}$, we use $\partial\hat{\Omega} = \cup_{i=1}^{4}\omega_i$. We take, $L_2 = 1$ mm and $L_1 = 2$ mm. The bottom boundary, $\omega_4 = \{(x, y)|y = 0, x \in (0, L_1)\}$, is heated with heat flux $S_0 = 3.3 \times 10^{-3}\dfrac{W}{mm^2}$ from the initial time, $t_0 = 0$, until t_s and insulated for $t > t_s$. We use an indicator function to describe the flash-heating of the boundary,

$$
\mathcal{I}_{[t_0,t_s]}(t) =
\begin{cases}
1 & \text{for } t \in [t_0, t_s] \\
0 & \text{otherwise.}
\end{cases}
$$

The other boundaries are insulated throughout the experiment. The boundary locations are given in Figure 3.1. This experiment can be described by the system

19

$$
\begin{cases}
c_p\rho\hat{u}_t - k\Delta\hat{u} = 0 & \text{in } \hat{\Omega} \times (0,T) \\[2mm]
k\dfrac{\partial\hat{u}}{\partial\eta} = S_0\mathcal{I}_{[t_0,t_s]}(t) & \text{on } \omega_4 \times (0,T) \\[2mm]
k\dfrac{\partial\hat{u}}{\partial\eta} = 0 & \text{on } \bigcup\limits_{i=1}^{3}\omega_i \times (0,T) \\[2mm]
\hat{u}(0,\vec{x}) = u_0 & \text{for all } \vec{x} \in \hat{\Omega},
\end{cases}
\tag{3.1}
$$

with thermal conductivity $k = 3.5 \times 10^{-3}$ J/(mm K sec), specific heat $c_p = 0.75$ J/(g K), material density $\rho = 1.6 \times 10^{-3}$ g/(mm^3), and the dependent variable $\hat{u}$ is temperature in degrees Kelvin. The values used throughout this chapter are summarized in Table 3.1. We will now make a few changes to the above system. In the partial differential equation, Δu may be written more generally as $\nabla \cdot (A^0\nabla u)$, where A^0 is the 2×2 identity matrix I_2 in the present section and Section 3.1. We make this change because subsequently we will replace the identity with another positive definite matrix, which will be derived from homogenization theory. Corresponding to this change, we must also change the boundary conditions, so that the boundary conditions still specify the flux when A^0 is not the identity matrix. Specifically, $\dfrac{\partial u}{\partial \eta} = \vec{n} \cdot \nabla u$, where $\vec{n}$ is the exterior unit normal vector, is replaced with $\dfrac{\partial u}{\partial \eta_{A^0}} = \vec{n} \cdot A^0\nabla u$. For convenience and without loss of generality, we will also translate the temperature so that the initial temperature, which we will take to also be the surrounding temperature, is zero. This corresponds to the change $u = \hat{u} - u_0$. We wish to use the thermal diffusivity, $\alpha = \dfrac{k}{c_p\rho}$, as a characteristic parameter

Table 3.1: Parameter values used throughout this document, unless otherwise mentioned. The 2×2 matrix, A^0 is a positive definite matrix arising from homogenization theory.

Parameter	Value	Units
$[t_0, t_s]$	$[0, 0.6]$	s
T	5	s
S_f	2.75	K mm/s
α	2.9167	mm^2/s
L_1	2	mm
L_2	1	mm
I_2	$\begin{bmatrix} 1 & 0 \\ 0 & 1 \end{bmatrix}$	

so our final system is

$$
\begin{cases}
u_t - \alpha \nabla \cdot \left(A^0 \nabla u \right) = 0 & \text{in } \hat{\Omega} \times (0, T) \\[2mm]
\alpha \dfrac{\partial u}{\partial \eta_{A^0}} = S_f \mathcal{I}_{[t_0, t_s]}(t) & \text{on } \omega_4 \times (0, T) \\[2mm]
\alpha \dfrac{\partial u}{\partial \eta_{A^0}} = 0 & \text{on } \displaystyle\bigcup_{i=1}^{3} \omega_i \times (0, T) \\[2mm]
u(\vec{x}, 0) = 0 & \text{for all } \vec{x} \in \hat{\Omega},
\end{cases}
\tag{3.2}
$$

where $S_f = \dfrac{S_0}{c_p \rho}$.

The zero flux boundary conditions of (3.2) correspond to the physical assumption of a perfectly insulated boundary, which is not reasonable in many cases. We relax this assumption by replacing the boundary condition with Robin boundary conditions that correspond to the assumption that Newton cooling occurs on the boundaries. This is succinctly incorporated into system (3.3), below, by including a $-\lambda u$ term in all of the boundary conditions. We further relax the assumptions associated with (3.2) by no longer

assuming that there is no heat flow in the direction orthogonal to the two dimensional representation of the specimen. The assumption that there is some small amount of heat loss over the entire specimen is modeled by adding a γu term in the partial differential equation. These changes yield the partial differential equation,

$$\begin{cases} u_t - \alpha \nabla \cdot \left(A^0 \nabla u \right) + \gamma u = 0 & \text{in } \hat{\Omega} \times (0, T) \\ \alpha \dfrac{\partial u}{\partial \eta_{A^0}} = S_f \mathcal{I}_{[t_0, t_s]}(t) - \lambda u & \text{on } \omega_4 \times (0, T) \\ \alpha \dfrac{\partial u}{\partial \eta_{A^0}} = -\lambda u & \text{on } \cup_{i=1}^3 \omega_i \times (0, T) \\ u(\vec{x}, 0) = 0. \end{cases} \tag{3.3}$$

It is important to recall that $u = \hat{u} - u_0$ where $\hat{u}$ is the temperature and u_0 is both the initial temperature and the temperature surrounding the specimen. System (3.3) is a generalization of (3.2) in that, (3.3) is identical to (3.2) for $(\gamma, \lambda) = (0, 0)$.

3.2 Numerical Solutions

We will use the finite element method to numerically solve (3.3). The finite element method approximates the infinite dimensional solution of a partial differential equation with a finite dimensional approximation. The domain ($\hat{\Omega}$) is discretized using the Delaunay triangulation. The finite dimensional solution is taken from the space of piecewise two dimensional affine functions, where the solution is affine on each mesh element (see [25] and [29] for details). Recall the notation $\vec{n} = (n_x, n_y)$, where n is the unit outward

normal and $\dfrac{\partial u}{\partial \eta_{A^0}} = \vec{n} \cdot \left(A^0 \nabla u \right)$. The boundary conditions can also be written as

$$
\alpha \frac{\partial u}{\partial \eta_{A^0}} = \alpha \left(a_{11} \frac{\partial u}{\partial x} + a_{12} \frac{\partial u}{\partial y} \right) = -\lambda u \qquad \text{on } \omega_3
$$

$$
\alpha \frac{\partial u}{\partial \eta_{A^0}} = \alpha \left(-a_{11} \frac{\partial u}{\partial x} - a_{12} \frac{\partial u}{\partial y} \right) = -\lambda u \qquad \text{on } \omega_1
$$

$$
\alpha \frac{\partial u}{\partial \eta_{A^0}} = \alpha \left(a_{21} \frac{\partial u}{\partial x} + a_{22} \frac{\partial u}{\partial y} \right) = -\lambda u \qquad \text{on } \omega_2
$$

$$
\alpha \frac{\partial u}{\partial \eta_{A^0}} = \partial \alpha \left(-a_{21} \frac{\partial u}{\partial x} - a_{22} \frac{\partial u}{\partial y} \right) = S_f \mathcal{I}_{[t_0, t_s]}(t) - \lambda u \quad \text{on } \omega_4.
$$

(3.4)

Using Green's identities, we obtain the weak form

$$
\int_{\hat{\Omega}} \phi(\vec{x}) u_t \, d\vec{x} \;+\; \alpha \int_{\hat{\Omega}} \phi(\vec{x}) \nabla \phi \cdot A^0 \nabla u \, d\vec{x} + \gamma \int_{\hat{\Omega}} \phi(\vec{x}) u \, d\vec{x}
$$

$$
- \int_{\omega_4} \phi(x, 0) S_f \mathcal{I}_{[t_0, t_s]}(t) \, dx + \lambda \int_{\partial \hat{\Omega}} \phi u \, ds = 0
$$

or

$$
\langle u_t, \phi \rangle + \alpha \langle \nabla \phi, A^0 u \rangle + \gamma \langle u, \phi \rangle - \int_{\omega_4} \phi(x, 0) S_f \mathcal{I}_{[t_0, t_s]}(t) \, dx + \lambda \int_{\partial \hat{\Omega}} \phi u \, ds = 0
$$

where $\langle \phi, v \rangle = \displaystyle\int_{\hat{\Omega}} \phi v \, d\vec{x}$. Here ϕ is a member of the space of test functions $H^1(\hat{\Omega})$. We approximate u with u_N by

$$
u_N(t, \vec{x}) = \sum_{i=1}^{N} T_i(t) \phi_i(\vec{x}).
$$

Substituting this expression into the weak form with test functions ϕ_i, $i \in \{1, 2, \ldots N\}$ in the space of two dimensional affine functions (we refer the reader to [29] for more details on these basis elements and the time dependent coefficients $T_i(t)$), we have

$$\left\langle \frac{\partial}{\partial t} \left(\sum_{i=1}^{N} T_i(t)\phi_i \right), \phi_j \right\rangle + \alpha \left\langle \nabla\phi_j, A^0\nabla \left(\sum_{i=1}^{N} T_i(t)\phi_i \right) \right\rangle + \gamma \left\langle \left(\sum_{i=1}^{N} T_i(t)\phi_i \right), \phi_j \right\rangle$$

$$- \int_{\omega_4} \phi_j(x,0)S_f\mathcal{I}_{[t_0,t_s]}(t)dx + \lambda \int_{\partial\hat{\Omega}} \sum_{i=1}^{N} T_i(t)\phi_i\phi_j \, ds = 0.$$
$$(3.5)$$

We may factor the time dependent coefficients $T_i(t)$ of the basis elements $\phi_i(\vec{x})$ from the inner product to obtain

$$\sum_{i=1}^{N} \frac{d}{dt}T_i \langle \phi_i, \phi_j \rangle + \alpha \sum_{i=1}^{N} T_i \langle \nabla\phi_j, A^0\nabla\phi_i \rangle + \gamma \sum_{i=1}^{N} T_i \langle \phi_i, \phi_j \rangle$$
$$(3.6)$$
$$- S_f\mathcal{I}_{[t_0,t_s]}(t) \int_{\omega_4} \phi_j(x,0)dx + \lambda \sum_{i=1}^{N} T_i \int_{\partial\hat{\Omega}} \phi_i\phi_j \, ds = 0.$$

Equation (3.6) must be true for arbitrary $j \in \{1, 2, \ldots, N\}$ and the system may be written as

$$C\frac{d}{dt}\vec{T}(t) + (\alpha M + \gamma C + \lambda D)\vec{T}(t) = S_f\mathcal{I}_{[t_0,t_s]}(t)\vec{f}, \qquad (3.7)$$

where C is an $N \times N$ positive definite matrix with elements $c_{ij} = \langle \phi_i, \phi_j \rangle$, M is an $N \times N$ positive definite matrix with elements $m_{ij} = \langle \nabla\phi_i, A^0\nabla\phi_j \rangle$, D is an $N \times N$ matrix with components $d_{ij} = \int_{\partial\hat{\Omega}} \phi_i\phi_j \, ds$, $\vec{f}$ is an N-vector with components $f_i = \int_{\omega_4} \phi_i(x,0)dx$ and $\vec{T}$ is an N column vector. We informally verified our calculations of these arrays in the case where $A^0 = I_2$ by comparing them to the corresponding values used to calculate the finite element method solution in MATLAB's PDE toolbox [25].

3.3　Homogenization

Now that we have considered a model of the flash-heat experiment on a homogeneous domain, we will model the flash heat experiment on the more complicated perforated domains developed in Chapter 2. Though these simulations were useful in detecting damage, they were too computationally intensive for the more sophisticated parameter estimation procedures needed to characterize damage. Here we will use (3.3) along with random geometries to model the flash heat experiment in a porous domain and compare this model to a limit partial differential equation which is derived from homogenization theory. In this formulation A^0 is no longer I_2 and the random complicated geometry is replaced with a less complicated domain with anisotropic flow. We will focus on values obtained on the source boundary ω_4 when we compare the subsequent models.

We will consider the random geometry Ω (depicted in Figure 2.1 in Chapter 2), which is composed of $\hat{\Omega} \setminus \cup_{i=1}^{n_r} \Omega_i$, where Ω_i are randomly placed pores, $\partial \Omega_i$ is the boundary of the ith pore and ω_i are the same as defined in Section 3.1 and in Chapter 2. We must now pose our problem on Ω. We will call the dependent variable of this system u^{rand}, where 'rand' refers to the random domain. Here it is worthwhile to note that we have performed the transformations detailed in the beginning of Section 3.1 to all of the partial differential equations in all subsequent chapters and sections.

The system corresponding to (3.3) on the random domain Ω is given by

$$
\begin{cases}
u_t^{\text{rand}} - \alpha \Delta u^{\text{rand}} + \gamma u^{\text{rand}} = 0 & \text{on } \Omega \times (0, T) \\[2mm]
\alpha \dfrac{\partial}{\partial \eta} u^{\text{rand}} = 0 & \text{on } \cup_{i=1}^{n_r} \partial \Omega_i \times (0, T) \\[2mm]
\alpha \dfrac{\partial}{\partial \eta} u^{\text{rand}} = -\lambda u^{\text{rand}} & \text{on } \cup_{i=1}^{3} \omega_i \times (0, T) \\[2mm]
\alpha \dfrac{\partial}{\partial \eta} u^{\text{rand}} = S_f \mathcal{I}_{[0, t_s]}(t) - \lambda u^{\text{rand}} & \text{on } \omega_4 \times (0, T) \\[2mm]
u^{\text{rand}}(\vec{x}, 0) = 0.
\end{cases}
\tag{3.8}
$$

We will use (3.8) to simulate data that one might expect from the flash-heat experiment performed on porous specimens. We generate these geometries and solve the partial differential equations using the methods developed in Chapter 2.

In order to apply homogenization theory to (3.8), we will use geometries with enough pores to suppose that Ω has a periodic structure (though it may be that the physical specimens are better modeled with periodic pores as the pores in composite materials are often the result of sinusoidal manufacturing processes). In other words, we suppose that the pores (or holes) are periodically distributed with a period ε, where ε is a small parameter that we let go to zero in the limit. This is the framework of the periodic homogenization theory which is explained in more detail in [19]. To do so, we introduce a reference cell (or domain) Y. For our purpose, let us take as Y the original (homogeneous) rectangle $\hat{\Omega}$. Let $B = \cup_{i=1}^{N} B_i$ be a set of N open subsets strictly included in Y such that $B_i \cap B_j = \emptyset$ for $i \neq j$.

Denote by $\tau(\varepsilon \overline{B})$ the set of all translated images of $\varepsilon \overline{B}$ of the form $\varepsilon(\kappa \ell + B)$, $\kappa \in \mathbb{Z}^2$, $\kappa \ell = (\kappa_1 \ell_1, \kappa_2 \ell_2)$, so the set $\tau(\varepsilon \overline{B})$ represents the periodic pores in $\mathbb{R}^2$. Let B^ε be the set of the holes contained in $\hat{\Omega}$. With the above choice of Y, and taking for instance

$$\varepsilon = \frac{1}{\left\lceil \sqrt{\frac{n_\varepsilon}{N}} \right\rceil}$$ with $n_\varepsilon \to +\infty$, no hole from B^ε will intersect the boundary $\partial\hat{\Omega}$. Here $\lceil \cdot \rceil$ is the nearest integer function. We will set

$$\Omega_\varepsilon = \hat{\Omega} \setminus \overline{B}^\varepsilon.$$

By this construction, the physical domain Ω_ε is periodically perforated with holes of size of the same order as the period. We are essentially approximating the random geometry Ω with the periodic geometry Ω_ε.

We will use the following notation:

· $Y^* = Y \setminus B$,

· $X^\dagger$, the topological dual space of X

· $p_V = \dfrac{|Y^*|}{|Y|}$, the proportion of the material in the cell Y,

· $|\omega| =$ the Lebesgue measure of any open set ω,

· $\mathcal{M}_\omega(\varphi) = \dfrac{1}{|\omega|} \displaystyle\int_\omega \varphi(x) \, dx$, the mean value of φ on the set ω.

Observe that by construction, p_V is also the proportion of the material in Ω_ε for any $\varepsilon > 0$ and the percent porosity $= (1 - p_V) \times 100\%$. We are now prepared to consider our

system on Ω_ε. Using Ω_ε to approximate Ω in (3.8), we have

$$
\begin{cases}
u_t^\varepsilon - \alpha \Delta u^\varepsilon + \gamma u^\varepsilon = 0 & \text{in } \Omega_\varepsilon \times (0, T) \\[2mm]
\alpha \dfrac{\partial}{\partial \eta} u^\varepsilon = 0 & \text{on } \partial B^\varepsilon \times (0, T) \\[2mm]
\alpha \dfrac{\partial}{\partial \eta} u^\varepsilon = -\lambda u^\varepsilon & \text{on } \cup_{i=1}^{3} \omega_i \times (0, T) \\[2mm]
\alpha \dfrac{\partial}{\partial \eta} u^\varepsilon = S_f \mathcal{I}_{[0, t_s]}(t) - \lambda u^\varepsilon & \text{on } \omega_4 \times (0, T) \\[2mm]
u^\varepsilon(\vec{x}, 0) = 0.
\end{cases}
\tag{3.9}
$$

The system (3.9) possesses a unique solution in the Banach space $\mathcal{W}_\varepsilon = \{v | v \in L^2(0, T; H^1(\Omega_\varepsilon)), \dfrac{\partial v}{\partial t} \in L^2(0, T; (H^1(\Omega_\varepsilon))^\dagger)\}$. One is then allowed to pass to the limit in (3.9) to obtain a limit homogenized system (for details, we refer the reader to [18, 19, 23]). In particular, these references contain proofs that

$$
\widetilde{u}^\varepsilon \rightharpoonup p_V U \quad \text{weakly in } L^2(0, T; H^1(\hat{\Omega})),
\tag{3.10}
$$

where U is characterized by the unique solution of the homogenized problem and $\widetilde{u}^\varepsilon$ is the zero extension of u^ε from Ω_ε to the whole domain $\hat{\Omega}$.

The limit system corresponding to (3.9) is given by

$$
\begin{cases}
p_V U_t - \alpha \nabla \cdot \left(A^0 U \right) + \gamma p_V U = 0 & \text{in } \hat{\Omega} \times (0, T) \\[2mm]
\alpha \dfrac{\partial U}{\partial \eta_{A^0}} = -\lambda U & \text{on } \cup_{i=1}^{3} \omega_i \times (0, T) \\[2mm]
\alpha \dfrac{\partial U}{\partial \eta_{A^0}} = S_f \mathcal{I}_{[0, t_s]}(t) - \lambda U & \text{on } \omega_4 \times (0, T) \\[2mm]
U(\vec{x}, 0) = 0.
\end{cases}
\tag{3.11}
$$

28

The homogenized operator A^0 has constant coefficients and is expressed in terms of the following cell problems defining the "corrector" functions χ_1 and χ_2:

$$
\begin{cases}
-\Delta \chi_j = 0 \quad \text{for } j = 1, 2 \quad \text{in } Y^* \\[2mm]
\chi_j \quad \text{is } Y \text{ periodic} \\[2mm]
\dfrac{\partial}{\partial \eta} (\chi_j - y_j) = 0 \quad \text{on } \partial \Omega_i \\[2mm]
\mathcal{M}_Y^*(\chi) = 0.
\end{cases}
\tag{3.12}
$$

Then the homogenized matrix $A^0 = (a_{ij}^0)$ is defined by

$$
a_{11}^0 = p_V - \frac{1}{|Y|} \int_{Y^*} \frac{\partial \chi_1}{\partial y_1} dy, \quad a_{12}^0 = -\frac{1}{|Y|} \int_{Y^*} \frac{\partial \chi_2}{\partial y_1} dy,
$$

$$
\tag{3.13}
$$

$$
a_{21}^0 = -\frac{1}{|Y|} \int_{Y^*} \frac{\partial \chi_1}{\partial y_2} dy, \qquad a_{22}^0 = p_V - \frac{1}{|Y|} \int_{Y^*} \frac{\partial \chi_2}{\partial y_2} dy.
$$

It is important to note that $\partial \Omega_i$ in (3.12) refers to the boundaries of the pores of the *reference cells*, depicted in Figure 3.2.

It can be shown that the error estimate (distance between $\widetilde{u}^\varepsilon$ and $p_V U$ in the $L^2(0, T; H^1(\hat{\Omega}))$-norm) is of order of $\sqrt{\varepsilon}$, which justifies the homogenization procedure if ε is sufficiently small, or equivalently if the number n_ε of holes is sufficiently large since $n_\varepsilon \sim \frac{1}{\varepsilon^2}$. Using the linear trace operator, $\gamma : H^1(\hat{\Omega}) \to L^2(\omega_4)$ and arguments similar to those in [16], we get the result that $\gamma(\widetilde{u}^\varepsilon)$ converges weakly in $L^2(\omega_4)$ to $\gamma(U)$.

Recalling the convergence of $\widetilde{u}^\varepsilon$ to U, we created numerical simulations to compare U to u^ε and u^{rand} on ω_4. We used methods developed in [4] and [30] to generate the random geometries Ω and Y^*. We used MATLAB's PDE toolbox to then solve these partial differential equations on these domains. One can not directly solve (3.12) with
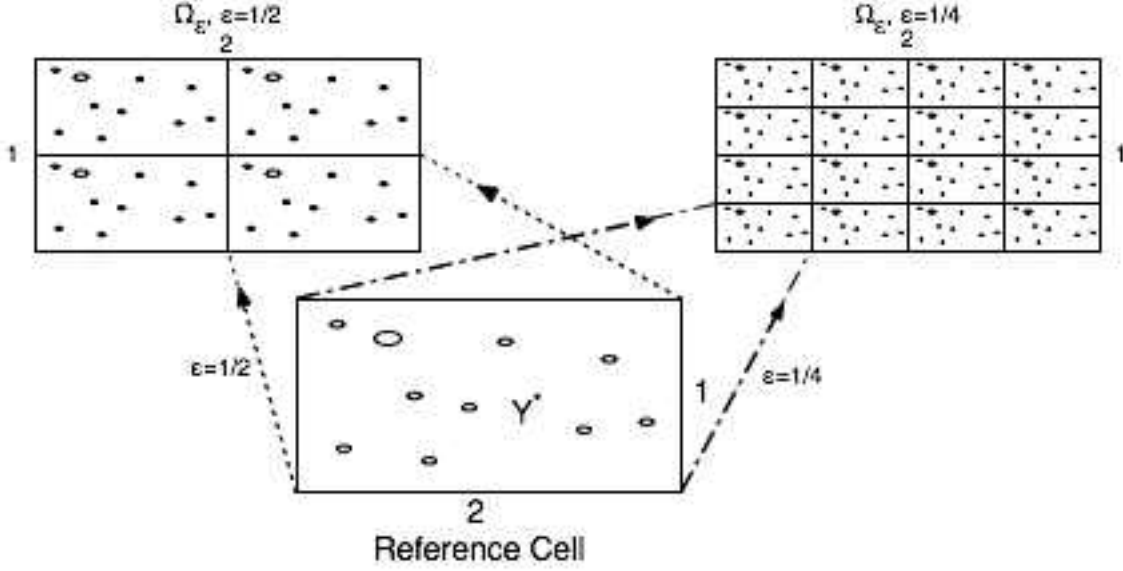
Figure 3.2: The reference domain and the limit domain with $\varepsilon = \dfrac{1}{2}$ and $\varepsilon = \dfrac{1}{4}$.

MATLAB's PDE Toolbox, we use the method described on pages 45–46 in [13] to solve this elliptic system of partial differential equations. To calculate U, we used the finite element schemes detailed in Section 3.2.

For each simulation, letting N be the number of pores in the reference cell, and n_r the number of pores in the random geometry, we might suppose that the ε corresponding to the Ω_ε which approximates Ω is given by

$$\varepsilon = \frac{1}{\left\lceil \sqrt{\frac{n_r}{N}} \right\rceil}, \tag{3.14}$$

with $\lceil \cdot \rceil$ representing the nearest integer function. As we see in (3.14), ε decreases as N decreases. This leads to a subtlety in choosing N. We would like Y^* to capture the random nature of Ω while still containing a sufficiently small number of pores N to ensure ε is small. In the simulations presented here, we take $N = 2$ and use (3.14) above to

calculate u^ε.

3.4 Approximation Results

In the previous section we developed (3.8) (with solution u^{rand}) to model the flash heat equation in porous material and (3.9) (with solution u^ε) to approximate (3.8). Finally, we introduced homogenization theory to approximate (3.9) with (3.11) (with solution U). In this section we will present graphical results corresponding to the three systems and summarize the results of 200 simulations of the three systems. Here, we will use the parameter values listed in Table 3.1. In each figure u^{rand} is the solution of (3.8), u^ε is the solution of (3.9) and U is the solution of (3.11). We will consider three different porosity levels, 10% (or $p_V = 0.9$, depicted in Figure 3.3), 5% (or $p_V = 0.95$, depicted in Figure 3.4), and 2% (or $p_V = 0.98$, depicted in Figure 3.5). The results presented here are for $(\gamma, \lambda) = (0, 10^{-5})$ though we carried out calculations for $(\gamma, \lambda) = (0, 0)$ (the perfectly insulated model), $(\gamma, \lambda) = (0, 6 \times 10^{-3})$, and $(\gamma, \lambda) = (10^{-5}, 0)$, each yielded similar results (see [6] for details). The random geometries used for the examples are featured in Figures 3.3–3.5(a), which corresponds to Ω used in (3.8). The approximations of Ω, Ω_ε, are presented for each level of porosity in Figures 3.3–3.5(b). Figures 3.3–3.5(c) give the solutions u^{rand}, u^ε and U at $y = 0$, $t = 0.1$ over all values of x on ω_4 or the source boundary. In this case, we see that U seems to capture the 'average' behavior of u^{rand} and that of u^ε. We observe that U overestimates when there are large pores near ω_4 and underestimates when there are not large pores near ω_4. In Figures 3.3 with $p_V = 0.9$ we see that the cluster of pores near ω_4 in Figure 3.3(a) corresponds to U underestimating u^{rand} for x greater than 1.25 in Figure 3.3(c). There are pores near ω_4 in Figure 3.3(b) which corresponds to periodic peaks of u^ε above U in Figure 3.3(c). There are pores near

31

ω_4 in Ω_ε in Figure 3.4(b) but they are very small and U overestimates u^ε in Figure 3.4(c). As should be expected for these systems, the difference between the three solutions seems to decrease with porosity. In Figure 3.5(c) it appears that U is a better estimate for u^{rand} and u^ε at $p_V = 0.98$ than it was for $p_V = 0.95$ depicted in Figure 3.4(c) and $p_V = 0.9$ depicted in Figure 3.3, so we see that U is a better approximation at lower levels of porosity or higher values of p_V.
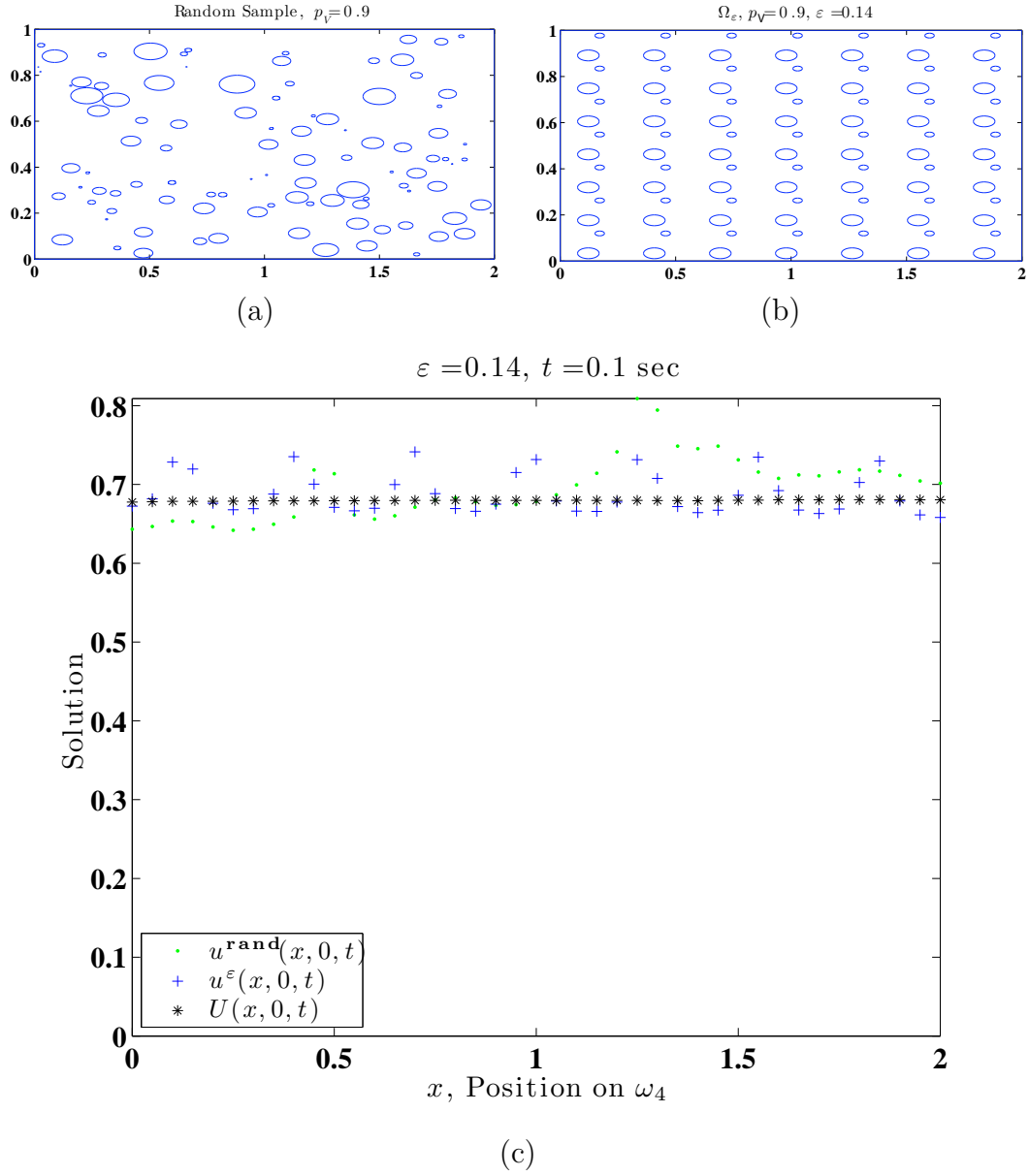
Figure 3.3: An example simulation at $p_V = 0.9$, or equivalently 10% porosity (a) The random geometry Ω; (b) The geometric approximation of Ω assumed in homogenization theory, Ω_ε where $\varepsilon = 0.14$; (c) $u^{\text{rand}}(x, 0, t)$, $u^\varepsilon(x, 0, t)$, and $U(x, 0, t)$ for $t = 0.1$ sec on ω_4. For a better representation of the behavior of the three systems over time on the source boundary (ω_4), see the corresponding movie at http://www4.ncsu.edu/~akcriner/movies/wholerobin9front.zip.
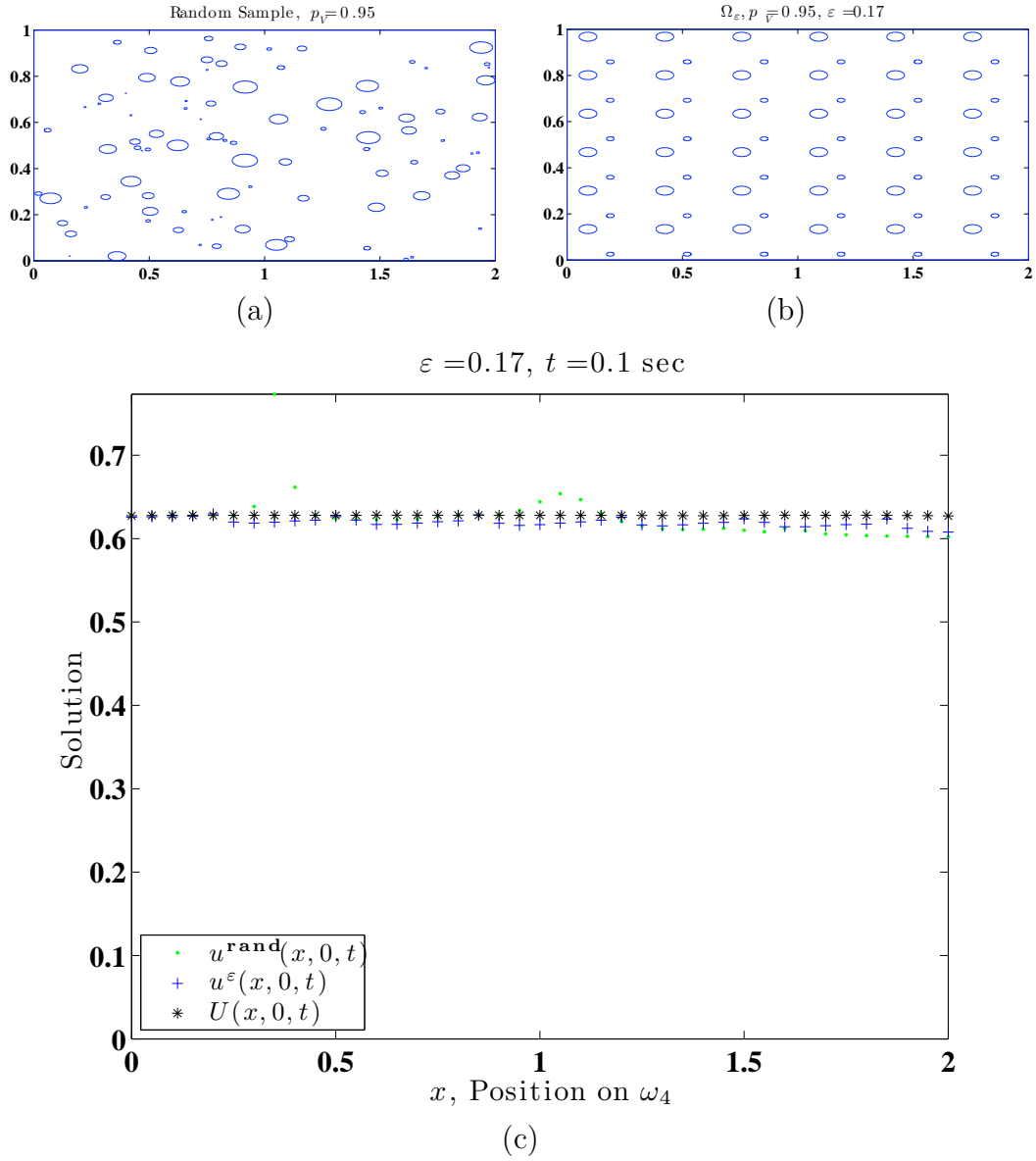
Figure 3.4: An example simulation at $p_V = 0.95$, or equivalently 5% porosity (a) The random geometry Ω; (b) The geometric approximation of Ω assumed in homogenization theory, Ω_ε where $\varepsilon = 0.17$; (c) $u^{\text{rand}}(x,0,t)$, $u^\varepsilon(x,0,t)$, and $U(x,0,t)$ for $t = 0.1$ sec on ω_4. For a better representation of the behavior of the three systems over time on the source boundary (ω_4), see the corresponding movie at http://www4.ncsu.edu/~akcriner/movies/wholerobin95front.zip.
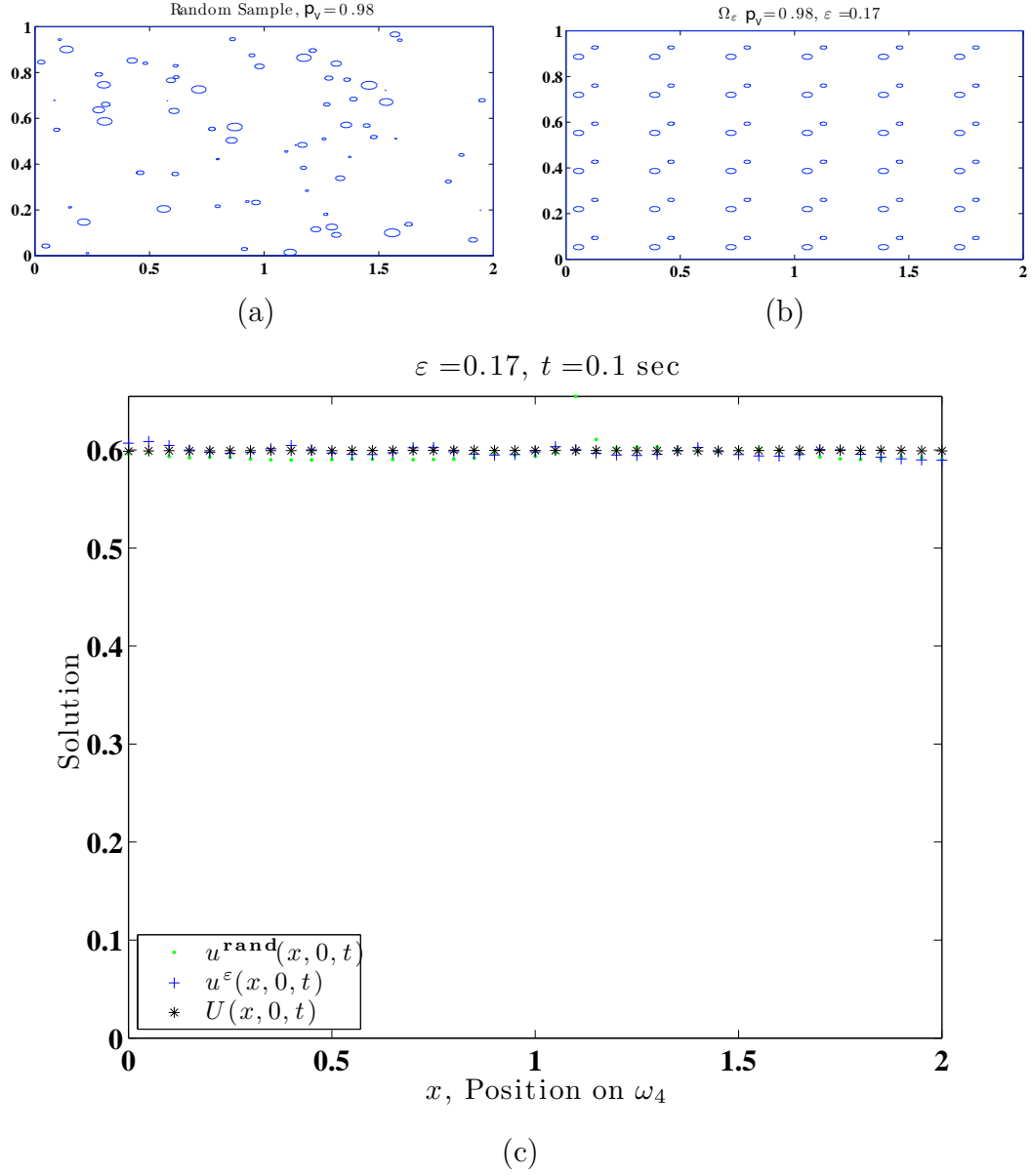
Figure 3.5: An example simulation at $p_V = 0.98$, or equivalently 2% porosity (a) The random geometry Ω; (b) The geometric approximation of Ω assumed in homogenization theory, Ω_ε where $\varepsilon = 0.17$; (c) $u^{\mathrm{rand}}(x,0,t)$, $u^\varepsilon(x,0,t)$, and $U(x,0,t)$ for $t = 0.1$ sec on ω_4. For a better representation of the behavior of the three systems over time on the source boundary (ω_4), see the corresponding movie at http://www4.ncsu.edu/~akcriner/movies/wholerobin98front.zip.

Table 3.2: In the first three rows, the last three columns contain the average time to calculate the respective solution for the 200 simulations. The last three rows contain the average mesh size over 200 simulations.

	Model	$p_V = 0.9$	$p_V = 0.95$	$p_V = 0.98$
Mean time	u^{rand}	45 sec	53 sec	62 sec
	u^ε	22 sec	28 sec	37 sec
	U	3.9 sec	4.0 sec	3.7 sec
Mean mesh size	u^{rand}	7851	8551	9965
	u^ε	5016	5744	7317
	U	355	355	355

We carried out 200 simulations at each porosity level ($p_V = 0.9, 0.95$ and 0.98) like those used to generate Figures 3.3–3.5. For each simulation, we randomly generated the domain Ω on which we solved (3.8) for u^{rand}. We also created a random Ω_ε, to solve (3.9) for u^ε. We used the reference cell used to generate Ω_ε to solve (3.11) for U. In Table 3.2 we report the average time to solve each of the systems and the average mesh size used to discretize the respective domain. It is clear that of the three systems (3.8) is the most computationally intensive. The limit system (3.11) is the least computationally intensive; its mesh is an order of magnitude smaller than the meshes for the other two systems. Also the computing time required to solve for U is five to ten times less than the time to solve for u^ε and ten to fifteen times less time to solve for u^{rand}. This supports the use of the limit system (3.11) as a more computationally suitable model than (3.8) and (3.9).

The limit system (3.11) seems to be a good approximation of (3.8) and (3.9). We consider the Frobenius norm of the difference between the limit systems on the source boundary ω_4. We will take values at time points $t_j = \dfrac{j-1}{20}$ for $j \in \{1, 2, \ldots 101\}$ and nodes $x_i = \dfrac{i-1}{20}$ for $i \in \{1, 2, \ldots 41\}$. For each simulation, we calculated the Frobenius

Table 3.3: The first and third row contain the mean Frobenius norm of the difference of the solutions for the 200 simiulations. The second and fourth row contain the standard deviation of the Frobenius norm of the difference of the solutions for the 200 simulations.

	$p_V = 0.9$	$p_V = 0.95$	$p_V = 0.98$
Mean $\|u^{\text{rand}} - U\|_F$	1.21	0.631	0.267
St. Dev. $\|u^{\text{rand}} - U\|_F$	0.245	0.109	0.042
Mean $\|u^\varepsilon - U\|_F$	1.322	0.656	0.267
St. Dev. $\|u^\varepsilon - U\|_F$	0.258	0.109	0.042

norm of $\|U - u^{\text{rand}}\|_F$

$$\|U - u^{\text{rand}}\|_F = \sqrt{\sum_{i=1}^{41}\sum_{j=1}^{101} \left(U(x_i, 0, t_j) - u^{\text{rand}}(x_i, 0, t_j)\right)^2}, \tag{3.15}$$

and $\|U - u^\varepsilon\|_F$. We report the average and standard deviation of these quantities for each porosity level in Table 3.3. As p_V increases, U better approximates both u^{rand} and u^ε. However, it is not clear that U better approximates either u^ε or u^{rand} which is interesting to note but would need a more analytical treatment to investigate.

We have selected and analyzed (3.3) which mathematically models the flash-heat experiment with uniformly imperfect insulation leading to small loss on all of the boundary of the rectangular cross section. The results of homogenization theory are encouraging. It is also clear that the choice of reference domain, specifically the location of pores in Ω_ε in relation to the source boundary ω_4 determines the efficacy of U to approximate u^ε. Similarly, the location of the pores in Ω in the random domain determine the behavior of u^{rand} in relation to the approximation U. We also observed that U approximates u^{rand} best at the lowest level of porosity, 98% or $p_V = 0.98$.

Based on these encouraging results, we will now use limit system (3.11) developed in

this chapter as a model to carry out parameter estimation of the parameter set $(\gamma, \alpha, \lambda)$. We will use data simulated with (3.8) with added noise (which often occurs in collected data) to evaluate the use of solutions of (3.11) as a model to describe data in inverse problems.

Chapter 4

Parameter estimation for the heat equation

4.1 Mathematical Models

Before considering the inverse problem, we will recall the models discussed in Chapters 2–3 for the forward problem. We again use the randomly perforated domain Ω depicted in Figure 2.1, and the homogeneous, non perforated domain $\hat{\Omega}$ which is an $L_1 \times L_2$ rectangle (again we will use $L_1 = 2$ and $L_2 = 1$) shown in Figure 3.1. The n_r randomly placed pores, which are generated using methods described in Chapters 2 and 3 and [30], are given by Ω_i with boundaries $\partial\Omega_i$ for $i = 1, 2 \ldots n_r$. We again assume that these pores do not intersect with each other nor the boundaries of $\hat{\Omega}$. The four boundaries of $\hat{\Omega}$ which are also the four exterior boundaries of Ω are denoted ω_i for $i = 1, 2, 3, 4$ (depicted in Figure 2.1). We continue to refer to ω_4 as the source boundary. The perforated domain Ω is given by $\hat{\Omega} \setminus (\cup_{i=1}^{n_r} \Omega_i)$. Recall the partial differential equation model of the flash heat

experiment on Ω

$$
\begin{cases}
u_t^{\text{rand}} - \alpha\nabla \cdot \left(\nabla u^{\text{rand}}\right) + \gamma u^{\text{rand}} = 0 & \text{in } \Omega \times (0,T) \\[2mm]
\alpha\dfrac{\partial u^{\text{rand}}}{\partial \eta} = 0 & \text{on } \cup_{i=1}^{n_r} \partial\Omega_i \times (0,T) \\[2mm]
\alpha\dfrac{\partial u^{\text{rand}}}{\partial \eta} = -\lambda u^{\text{rand}} & \text{on } \cup_{i=1}^{3} \omega_i \times (0,T) \\[2mm]
\alpha\dfrac{\partial u^{\text{rand}}}{\partial \eta} = S_f \mathcal{I}_{[0,t_s]}(t) - \lambda u^{\text{rand}} & \text{on } \omega_4 \times (0,T) \\[2mm]
u^{\text{rand}}(0,\vec{x}) = 0,
\end{cases}
\tag{4.1}
$$

where α is the thermal diffusivity of the material Ω, γ corresponds to loss in the direction orthogonal to the domain Ω (the z direction) and λ corresponds to loss on the boundary of the the rectangle $\hat{\Omega}$. The flash heat input is modeled by the term $S_f \mathcal{I}_{[0,t_s]}(t)$ where

$$
\mathcal{I}_{[0,t_s]}(t) = \begin{cases} 1, & \text{for } t \leq t_s \\[2mm] 0 & \text{for } t > t_s. \end{cases}
$$

There are many problems associated with using (4.1) as a model when performing the inverse problem. The computational time associated with solving the forward problem (4.1) is about two minutes. This is prohibitively long to perform the inverse problem. Also, for many applications of the forward model, two minutes is far too long a computational time as well. Beyond the computational intensity associated with solving (4.1), the random geometry of a porous sample (which we model as Ω) is not known for the applications that we are concerned with so we can not assume that we know Ω a priori.

In Chapter 3, using the results of homogenization theory (see [5],[15], [19], [17], [20]

and [18] and the references therein for details), we derived the limit system

$$
\begin{cases}
p_V U_t - \alpha \nabla \cdot \left(A^0 \nabla U \right) + \gamma p_V U = 0 & \text{in } \widehat{\Omega} \times (0, T) \\[2mm]
\alpha \dfrac{\partial U}{\partial \eta_{A^0}} = -\lambda U & \text{on } \cup_{i=1}^{3} \omega_i \times (0, T) \\[2mm]
\alpha \dfrac{\partial U}{\partial \eta_{A^0}} = S_f \mathcal{I}_{[0, t_s]}(t) - \lambda U & \text{on } \omega_4 \times (0, T) \\[2mm]
U(0, \vec{x}) = 0,
\end{cases}
\tag{4.2}
$$

where p_V is the proportion of $\widehat{\Omega}$ occupied by Ω ($p_V = \dfrac{\text{area of } \Omega}{\text{area of } \widehat{\Omega}}$) and A^0 is the 2×2 homogenized matrix which we calculate using methods described in Chapter 3 and [13]. We denote $\dfrac{\partial U}{\partial \eta_{A^0}} = \vec{n} \cdot A^0 \nabla U$ where $\vec{n}$ is the exterior unit normal vector. The action of A^0 is to approximate the isotropic flow through the random domain Ω around the perforations Ω_i with anisotropic flow through the homogeneous rectangle $\widehat{\Omega}$. We recall from Chapter 3 that as $n_r \to \infty$, $\nu(\widetilde{u}^{\text{rand}}) \to \nu(U)$ weakly in $L^2(0, T; L^2(\omega_4))$ where $\widetilde{\cdot}$ denotes the zero extension of Ω to all of $\widehat{\Omega}$ and ν is the linear trace operator $\nu :$ $L^2(0, T; H^1(\widehat{\Omega})) \to L^2(0, T; L^2(\omega_4))$. Based on this convergence, we will consider using U, the solution of (4.2), as a model solution in the ordinary least squares estimation procedure for simulated data of U with added absolute random error and for simulated data of u^{rand} (the solution of (4.1)) with added absolute random error in Section 4.2. In Section 4.3, we will consider using U as a model solution in the generalized least squares estimation procedure for simulated data of U with added relative random error and for simulated data of u^{rand} with added relative random error which is dependent on the value of u^{rand}.

4.2 Ordinary Least Squares

We will consider a statistical model, which describes data with random error that has zero mean, is independent and has constant variance. We will then discuss the OLS parameter estimation procedure in general and finally go on to present results of preforming the OLS parameter estimation procedure on two different kinds of simulated data in Section 4.2.1.

We will consider the full parameter set $\theta = (\gamma, \alpha, \lambda)$, and subsets $\theta^\lambda = (\gamma_\lambda, \alpha_\lambda)$ (corresponding to the assumption that the boundary loss parameter λ is known) and $\theta^\gamma = (\alpha_\gamma, \lambda_\gamma)$ (corresponding to the assumption that the parameter that models loss in the orthogonal direction γ is known). Now, that we have introduced the three parameter sets, we will use the notation $\theta^\#$ to mean any of the three parameter sets θ, θ^λ and θ^γ without loss of generality.

Full state observation is rare especially when the set of states is continuous (for our problem $\vec{x} \in \hat{\Omega}$). Often, when one performs thermal nondestructive evaluation, data is given by the output of an IR camera. To model the resulting pixels, we will consider

$$\mathcal{C}_i(\phi) = \frac{1}{\ell} \int_{x_i}^{x_i + \ell} \phi(s, 0) \, ds.$$

So $\mathcal{C}_i$ gives the average value of functions along intervals of length ℓ starting at $x = x_i$ on ω_4 (the source boundary). We will suppose the "perfectly resolved" data is given by

$$U_{ij}(\theta_0^\#) = \frac{1}{\ell} \int_{x_i}^{x_i + \ell} U(t_j, s, 0; \theta_0^\#) \, ds \tag{4.3}$$

or $U_{ij}(\theta_0^\#) = \mathcal{C}_i U(t_j, \vec{x}; \theta_0^\#)$ where $\theta_0^\#$ is the "true" parameter value. We will denote m spatial nodes $x_i = x_1, x_2, \ldots, x_m$ and n temporal nodes $t_j = t_1, t_2, \ldots, t_n$. The statistical assumptions that underlie the OLS parameter estimation procedure corresponding to this

observation process is then that data are given by realizations of the random process $\boldsymbol{y}_{ij}$ which is defined as

$$\boldsymbol{y}_{ij} = U_{ij}(\theta_0^\#) + \boldsymbol{\epsilon}_{ij}, \tag{4.4}$$

where $\boldsymbol{\epsilon}_{ij}$ is a random variable that satisfies (4.5) below. The random variable (random error) $\boldsymbol{\epsilon}_{ij}$ is further assumed to have zero mean, be independent and have constant variance. More precisely, we assume

$$
\begin{aligned}
E(\boldsymbol{\epsilon}_{ij}) &= 0 \\
Var(\boldsymbol{\epsilon}_{ij}) &= \sigma_0^2 \\
Cov(\boldsymbol{\epsilon}_{ij}, \boldsymbol{\epsilon}_{kh}) &= 0 \text{ for } (i, j) \neq (k, h).
\end{aligned}
\tag{4.5}
$$

It is important to emphasize that $\boldsymbol{y}_{ij}$ is a random variable with realizations y_{ij}. The realization y_{ij} would correspond to observed data.

In order to obtain the parameter estimate $\hat{\theta}^\#$, we must minimize the OLS cost functional

$$J(\theta^\#) = \sum_{i=1}^{m} \sum_{j=1}^{n} (U_{ij}(\theta^\#) - y_{ij})^2. \tag{4.6}$$

For each data set y_{ij}, the parameter estimate is given by

$$\hat{\theta}^\# = \arg \min_{\theta^\# \in \Theta^\#} J(\theta^\#) \tag{4.7}$$

where $\Theta^\#$ is an admissible parameter set. The error estimate is then given by

$$\hat{\sigma}_\#^2 = \frac{J(\hat{\theta}^\#)}{nm - p} \tag{4.8}$$

where p is the number of parameters so $p = 2$ for $\hat{\theta}^\# = \hat{\theta}^\gamma$ and $\hat{\theta}^\# = \hat{\theta}^\lambda$ while $p = 3$ for

$\hat{\theta}^{\#} = \hat{\theta}$.

Data collection nodes can be selected in many sophisticated ways such as by using SE-optimal design, E-optimal design, D-optimal and c-optimal design methods (see [12] and references therein). This is not the focus of our current efforts so we will examine the sensitivity functions to select data collections nodes. For each parameter $\theta_k^{\#}$ in the parameter set $\theta^{\#}$, the associated sensitivity function (the sensitivity of the model solution with respect to $\theta_k^{\#}$) $V^{\theta_k^{\#}} = \dfrac{\partial U}{\partial \theta_k^{\#}}$ corresponds to the sensitivity of the solution with respect to the kth parameter. In places where the sensitivity $V^{\theta_k^{\#}}$ is zero, one cannot obtain any information about the kth parameter. However, one should not exclusively choose nodes in the regions of the highest sensitivity [8].

We examined the sensitivity functions

$$
\begin{aligned}
V^{\gamma}(t, x_i) &= \frac{\partial}{\partial \gamma} \left(\frac{1}{\ell} \int_{x_i}^{x_i + \ell} U(t, s, 0; (10^{-3}, 2.9167, 0.01)) \, ds \right) \\
V^{\alpha}(t, x_i) &= \frac{\partial}{\partial \alpha} \left(\frac{1}{\ell} \int_{x_i}^{x_i + \ell} U(t, s, 0; (10^{-3}, 2.9167, 0.01)) \, ds \right) \\
V^{\lambda}(t, x_i) &= \frac{\partial}{\partial \lambda} \left(\frac{1}{\ell} \int_{x_i}^{x_i + \ell} U(t, s, 0; (10^{-3}, 2.9167, 0.01)) \, ds \right)
\end{aligned}
\tag{4.9}
$$

for $\ell = 0.57$ and $x_i = 0, 0.57, 1.14, 1.71$ using calculations detailed in Appendix A.1. We chose the values of x_i and ℓ based on an example pixel width. We chose $\gamma = 10^{-3}$, $\alpha = 2.9167$ and $\lambda = 0.01$ based on physically reasonable values. These are also values that we will use when we simulate data in Sections 4.2.1 and 4.3.1.

After inspecting V^{γ}, V^{α} and V^{λ} for different values of x_i, we noticed little difference so we arbitrarily chose two sets of spatial nodes $x_i \in \{0, 0.57\}$ and $x_i \in \{0, 0.57, 1.14\}$ to consider the effect of sparsity of spatial nodes on the inverse problem. The values of $V^{\gamma}(t, x_i)$, $V^{\alpha}(t, x_i)$ and $V^{\lambda}(t, x_i)$ vary over time as depicted in Figures 4.1(a) and (b). The sensitivity with respect to α, $V^{\alpha}(t, x_i)$ goes toward zero quickly after the
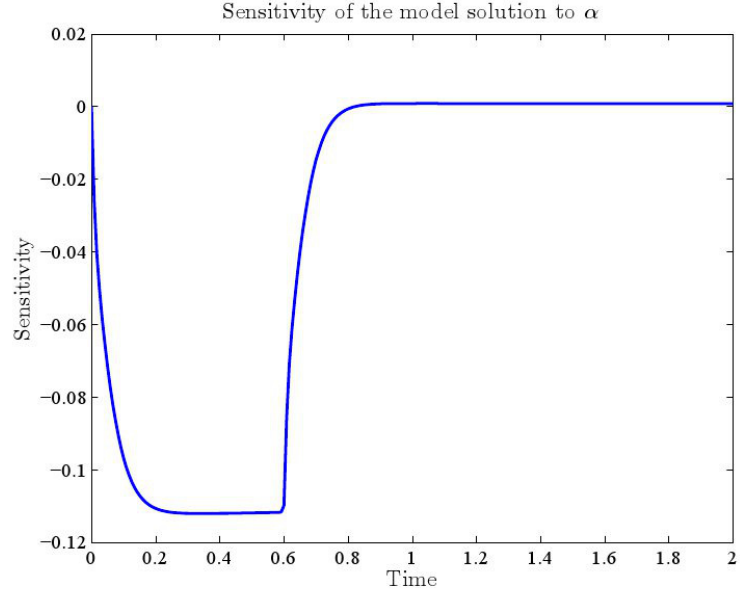
(a)
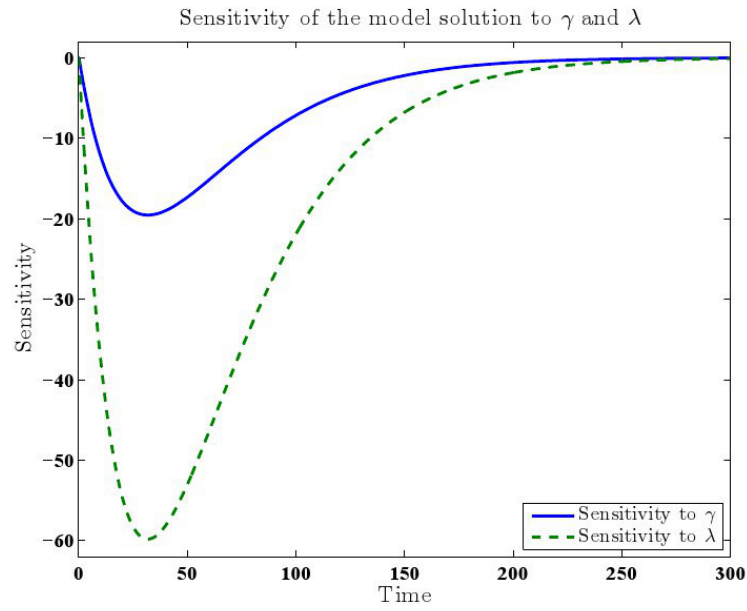
(b)

Figure 4.1: The sensitivity functions of $\dfrac{1}{0.57}\displaystyle\int_0^{0.57} U(t,s,0)\,ds$ where U is the solution of (4.2) with $\gamma = 10^{-3}$, $\alpha = 2.9167$ and $\lambda = 0.01$. (a) The sensitivity with respect to α for time $t \in [0,2]$. (b) The sensitivity with respect to λ and γ for time $t \in [0,300]$.

end of flash-heating at $t_s = 0.6$ s in Figure 4.1(a). There is often more measurement error during flash-heating so we take many times just after the end of flash heating $\{0.6 + \frac{1}{120}, 0.6 + \frac{2}{120}, \ldots 0.6 + \frac{7}{120}\}$ to gain information about the parameter α. The sensitivities to γ and λ are depicted in Figure 4.1(b) and go to zero much more slowly than V^α. We take times $\{20, 40, \ldots, 140\}$ to gain information about the parameters γ and λ. We note that in Figure 4.1(b) the sensitivity with respect to γ is less than the sensitivity with respect to λ. This suggests that there could be problems estimating γ; we will further discuss the well-posedness of estimating γ in Section 4.2.1.

Using the sensitivity matrix with entries

$$\chi_{i+m(j-1),k}(\theta) = \left. \frac{\partial}{\partial \theta_k} U_{ij}(\zeta) \right|_{\zeta=\theta} \tag{4.10}$$

we may calculate the estimated covariance matrix

$$\Sigma(\hat{\theta}^\#) = \hat{\sigma}^2 \left(\chi^T(\hat{\theta}^\#) \chi(\hat{\theta}^\#) \right) \tag{4.11}$$

and the estimated standard error of the kth parameter

$$\mathrm{SE}(\hat{\theta}_k^\#) = \sqrt{\Sigma_{kk}(\hat{\theta}^\#)}. \tag{4.12}$$

4.2.1 Simulated Ordinary Least Squares Data

We would like to consider data motivated by (4.1) because we suspect that this model will resemble experimental data. We can not, however, use (4.1) as a model solution in the OLS cost functional (4.6) because the random geometry Ω in (4.1) is not a priori knowledge in most thermal nondestructive evaluation applications. Thus we are con-

cerned with the behavior of $U_{ij}(\theta)$ as a model solution in the inverse problem with data motivated by u^{rand}. It is not simple to ensure that the OLS assumptions are satisfied even in the most straight forward cases because relations between parameters can cause violations in the OLS assumptions. For instance, the estimation of γ is ill-posed. In the partial differential equation (4.2), if we make the transformation $U = e^{-\gamma t}Z$ in (4.2) the partial differential equation becomes

$$
\begin{cases}
p_V Z_t - \alpha \nabla \cdot \left(A^0 \nabla Z \right) = 0 & \text{on } \hat{\Omega} \times (0, T) \\
\alpha \dfrac{\partial Z}{\partial \eta_{A^0}} = -\lambda Z & \text{on } \cup_{i=1}^3 \omega_i \times (0, T) \\
\alpha \dfrac{\partial Z}{\partial \eta_{A^0}} = S_f \mathcal{I}_{[0,t_s]}(t) - \lambda Z & \text{on } \omega_4 \times (0, T)
\end{cases}
\tag{4.13}
$$

This means that if we rewrite the cost functional in (4.6) as

$$
J(U(t_j, \vec{x}_i; \theta), \mathrm{D}_{ij}) = \sum_{i=1}^m \sum_{j=1}^n \left(U(t_j, \vec{x}_i; \theta) - \mathrm{D}_{ij} \right)^2
\tag{4.14}
$$

we can see that the cost functional $J(U(t_i j, \vec{x}_i; \theta), \mathrm{D}_{ij})$ in (4.14) where $U(t_j, \vec{x}_i; \theta)$ is the solution of (4.2) can equivalently be written as

$$
J(U(t_j, \vec{x}_i; \theta, \mathrm{D}_{ij}) = J(Z(t_j, \vec{x}_i; \theta), e^{\gamma t_j} \mathrm{D}_{ij})
\tag{4.15}
$$

where $Z(t_j, \vec{x}_i; \theta)$ is the solution of (4.13). This implies that by including γ any noise in the data will be amplified. This will also cause model dependence in the error in D_{ij} which violates the error assumptions (4.5).

Because of the subtlety in verifying the OLS error assumptions (4.5) directly, we will compare data simulated using the solution of (4.2) with data simulated using the solution

47

of (4.1). We simulate data motivated by OLS assumptions and the solution of (4.2) with the random process

$$\mathbf{D}_{ij}(\sigma) = U_{ij}(10^{-3}, 2.9167, 0.01) + \sigma\boldsymbol{\beta}_{ij} \tag{4.16}$$

where $\boldsymbol{\beta}_{ij}$ is a random variable which follows a standard normal distribution or $\boldsymbol{\beta}_{ij} \sim \mathcal{N}(0, 1^2)$. We consider two sets of spatial nodes $x_i = 0, 0.57$ and $x_i = 0, 0.57, 1.14$.

We simulate data motivated by the OLS error assumptions (4.5) and the solution of (4.1) with the random process

$$\mathbf{D}_{ij}^{\mathrm{rand}}(\sigma) = u_{ij}^{\mathrm{rand}} + \sigma\boldsymbol{\beta}_{ij} \tag{4.17}$$

where u_{ij}^{rand} is given by

$$u_{ij}^{\mathrm{rand}} = \frac{1}{\ell} \int_{x_i}^{x_i+\ell} u^{\mathrm{rand}}(t_j, s, 0; (10^{-3}, 2.9167, 0.01)) \, ds, \tag{4.18}$$

with $u^{\mathrm{rand}}(t_j, s, 0; (10^{-3}, 2.9167, 0.01))$ the solution of (4.1) with $(\gamma, \alpha, \lambda) = (10^{-3}, 2.9167, 0.01)$ on a randomly perforated geometry Ω.

For realizations of $\mathbf{D}_{ij}(\sigma)$ and $\mathbf{D}_{ij}^{\mathrm{rand}}(\sigma)$ each data set is analyzed using the results of OLS asymptotic theory for the parameter sets $\theta = (\gamma, \alpha, \lambda)$, $\theta^\gamma = (\alpha, \lambda)$ and $\theta^\lambda = (\gamma, \lambda)$. So for each data set we perform three inverse problems calculating three parameter estimates $\hat{\theta}^\gamma$, $\hat{\theta}^\lambda$ and $\hat{\theta}$ using (4.7), three error estimates $\hat{\sigma}_\gamma^2$, $\hat{\sigma}_\lambda^2$ and $\hat{\sigma}^2$ using (4.8), three covariance matrix estimates $\Sigma(\hat{\theta}^\gamma)$, $\Sigma(\hat{\theta}^\lambda)$, and $\Sigma(\hat{\theta})$ using (4.11), and the standard error for each parameter in the sets $\hat{\theta}$, $\hat{\theta}^\lambda$, and $\hat{\theta}^\gamma$ denoted $\mathrm{SE}(\hat{\gamma})$, $\mathrm{SE}(\hat{\alpha})$, $\mathrm{SE}(\hat{\lambda})$, $\mathrm{SE}(\hat{\gamma}_\lambda)$, $\mathrm{SE}(\hat{\alpha}_\lambda)$, $\mathrm{SE}(\hat{\alpha}_\gamma)$, and $\mathrm{SE}(\hat{\lambda}_\gamma)$ using (4.12).

There are many different ways to consider these parameter estimation and uncertainty estimation problems. We will consider the difference between the parameter estimate and

the "true" parameter values $\gamma_0 = 10^{-3}$, $\alpha_0 = 2.9167$, and $\lambda_0 = 0.01$ which will give us insight into the accuracy of the parameter estimate $\hat{\theta}_k^{\#}$. We will also consider the ratio of the estimated standard error to the parameter estimate or $\mathrm{SE}(\hat{\theta}_k^{\#})/\hat{\theta}_k^{\#}$. When this ratio is large, there is little confidence in the value of the parameter $\hat{\theta}_k^{\#}$. For instance, the 95% confidence interval for $m = 3$ for $\hat{\gamma}$ is given by

$$95\% \text{ confidence interval for } \hat{\gamma} = (\hat{\gamma} - 2.02 \times \mathrm{SE}(\hat{\gamma}), \hat{\gamma} + 2.02 \times \mathrm{SE}(\hat{\gamma})).$$

In this example when $\mathrm{SE}(\hat{\gamma})/\hat{\gamma}$ is greater than 0.5, we can not even be confident that the parameter γ is positive. So the ratio $\mathrm{SE}(\hat{\theta}_k^{\#})/\hat{\theta}_k^{\#}$ is related to the uncertainty associated with the parameter estimate $\hat{\theta}_k^{\#}$.

We will now compare the results of ordinary least squares parameter estimation procedure for realizations of $\mathbf{D}_{ij}(\sigma)$ with the results of ordinary least squares parameter estimation procedure for realizations of $\mathbf{D}_{ij}^{\mathrm{rand}}(\sigma)$. In Figures 4.2–4.7, the simulated data is taken at temporal collection nodes $t_j = 0.6 + \dfrac{1}{120}, 0.6 + \dfrac{2}{120}, \ldots, 0.6 + \dfrac{7}{120}, 20, 40, \ldots, 140$ and spatial nodes $x_i = 0, 0.57, 1.14$. Figure 4.2(a) depicts the difference $\hat{\alpha}_{\#} - \alpha_0$ for each of five realizations at each level of added noise $\sigma = 0.015, 0.030, \ldots, 0.090$ for $\mathbf{D}_{ij}(\sigma)$. The estimates for the three parameter subsets do not seem to vary much. That is, we see that for each realization the differences $\hat{\alpha} - \alpha_0$, $\hat{\alpha}_\gamma - \alpha_0$ and $\hat{\alpha}_\lambda - \alpha_0$ are relatively close. Figure 4.2(b) depicts the difference $\hat{\alpha}_{\#} - \alpha_0$ for each of five realizations of $\mathbf{D}_{ij}^{\mathrm{rand}}(\sigma)$ at each level of noise $\sigma = 0, 0.015, \ldots, 0.090$, we see that the differences $\hat{\alpha}_{\#} - \alpha_0$ do not seem to vary much for each realization either. Also, the results depicted in Figure 4.2(a) resemble the results depicted in Figure 4.2(b). This suggests that using realizations of $\mathbf{D}_{ij}(\sigma)$ versus $\mathbf{D}_{ij}^{\mathrm{rand}}(\sigma)$ does not affect the accuracy of the estimates $\hat{\alpha}_{\#}$. In Figures 4.3 (a) and (b), we examine the ratios $\mathrm{SE}(\hat{\alpha}_{\#})/\hat{\alpha}_{\#}$ for the five realizations of $\mathbf{D}_{ij}(\sigma)$ and

$\mathbf{D}_{ij}^{\mathrm{rand}}(\sigma)$, respectively. In Figure 4.3(a), we see that the uncertainty associated with the estimate $\hat{\alpha}$ is larger than the uncertainty associated with the estimates $\hat{\alpha}_\gamma$ and $\hat{\alpha}_\lambda$. It also appears that the ratio $\mathrm{SE}(\hat{\alpha}_\#)/\hat{\alpha}_\#$ varies linearly with σ. These observations are valid for the ratios depicted in Figure 4.3(b), as well. The similarities in Figure 4.3(a) and Figure 4.3(b) suggest that there is not a significant difference in using realizations $\mathbf{D}_{ij}(\sigma)$ and $\mathbf{D}_{ij}^{\mathrm{rand}}(\sigma)$ regarding the uncertainty associated the OLS parameter estimate $\hat{\alpha}_\#$.

We also considered the parameter λ. Figures 4.4(a) are the differences $\lambda_\# - \lambda_0$ ($\lambda_0 = 0.01$) for the realizations used in Figures 4.2(a) and 4.3(a). The difference $\hat{\lambda}_\# - \lambda_0$, unlike these differences for the parameter α, appears to depend on the parameter set. The magnitude of the difference $\hat{\lambda} - \lambda_0$ is much larger than the difference $\hat{\lambda}_\gamma - \lambda_0$ indicating that estimating γ adds inaccuracy to the estimate of λ. In Figure 4.4(b), we have plotted the difference $\hat{\lambda}_\# - \lambda_0$ for the realizations depicted in Figures 4.2(b) and 4.3(b). In Figure 4.4(b), we see that the differences $\hat{\lambda}_\gamma - \lambda_0$ and $\hat{\lambda} - \lambda_0$ for the realizations of $\mathbf{D}_{ij}^{\mathrm{rand}}(\sigma)$ resemble these differences for the realizations of $\mathbf{D}_{ij}(\sigma)$ in Figure 4.4(a) so we suspect that the error associated with the approximation of u^{rand} (the solution of (4.1)) with U (the solution of (4.2)) in the model solution does not affect the estimate of $\hat{\lambda}_\gamma$ nor $\hat{\lambda}$.

In Figure 4.5(a), we see that the ratio $\mathrm{SE}(\hat{\lambda}_\gamma)/\hat{\lambda}_\gamma$ appears to be linear in σ for the realizations of $\mathbf{D}_{ij}(\sigma)$. This linear pattern is similar to the linearity in Figure 4.5(c) which depicts the ratio $\mathrm{SE}(\hat{\lambda}_\gamma)/\hat{\lambda}_\gamma$ for the realizations of $\mathbf{D}_{ij}^{\mathrm{rand}}(\sigma)$. Also, the ratio $\mathrm{SE}(\hat{\lambda}_\gamma)/\hat{\lambda}_\gamma$ is on about the same scale in Figures 4.5(a) and (c). So for $\hat{\lambda}_\gamma$, there does not appear to be a difference in using data generated by (4.16) versus data generated by (4.17) in the accuracy of the parameter estimate $\hat{\lambda}_\gamma$ nor the uncertainty associated with the parameter estimate $\hat{\lambda}_\gamma$.
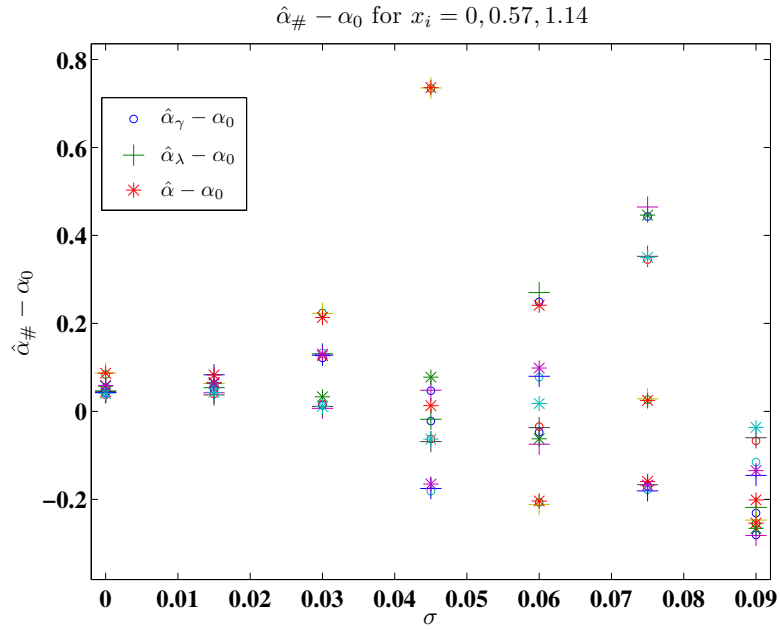
Figure 4.2: The points denoted with ^{o} are the difference $\hat{\alpha}_\gamma - \alpha_0$, the points denoted are the $\hat{\alpha}_\lambda - \alpha_0$, the points denoted * are the difference $\hat{\alpha} - \alpha_0$ (a) The result of five realizations of $\mathbf{D}_{ij}(\sigma)$ for values of $\sigma = 0.015, 0.030, \ldots, 0.090$ (b) The result of five realizations of $\mathbf{D}_{ij}^{\mathrm{rand}}(\sigma)$ for values of $\sigma = 0,0.015,\ldots,0.090$.

51

Figure 4.3: The points denoted with ^{o} are the ratio $\text{SE}(\hat{\alpha}_\gamma)/\hat{\alpha}_\gamma$, the points denoted are the $\text{SE}(\hat{\alpha}_\lambda)/\hat{\alpha}_\lambda$, the points denoted * are the difference $\text{SE}(\hat{\alpha})/\hat{\alpha}$ (a) The result of five realizations of $\mathbf{D}_{ij}(\sigma)$ for values of $\sigma = 0.015, 0.030, \ldots, 0.090$ (b) The result of five realizations of $\mathbf{D}_{ij}^{\text{rand}}(\sigma)$ for values of $\sigma = 0, 0.015, \ldots, 0.090$.

In order to consider the ratio $\mathrm{SE}(\hat{\lambda})/\hat{\lambda}$, we plotted the logarithm of this quantity in Figures 4.17(b) (for realizations of $\mathbf{D}_{ij}(\sigma)$ and (d) (for $\mathbf{D}_{ij}^{\mathrm{rand}}(\sigma)$ because in both examples these quantities vary greatly. The ratio $\mathrm{SE}(\hat{\lambda})/\hat{\lambda}$ in both Figure 4.17(b) and Figure 4.17(d) appears to grow exponentially with added error σ which is not surprising based on our observation in (4.15) that γ in the parameter estimation increases the error in the data.

The estimation of γ is ill-posed for the parameter values, spatial nodes and temporal nodes in this problem. In Figures 4.6(a) and (b), we see that the difference $\hat{\gamma} - \gamma_0$ ($\gamma_0 = 10^{-3}$) is very large compared to γ_0. This is true for both the realizations of $\mathbf{D}_{ij}(\sigma)$ in Figure 4.6(a) and the realizations of $\mathbf{D}_{ij}^{\mathrm{rand}}(\sigma)$ in Figure 4.6(b). Though the differences $\hat{\gamma}_\lambda - \gamma_0$ are smaller than $\hat{\gamma} - \gamma_0$ in Figures 4.6(a) and (b), in Figures 4.7(a) and (c) we see that the uncertainty associated with the estimate $\hat{\gamma}_\lambda$ is very large. In Figure 4.7(a), we see that, for the realizations of $\mathbf{D}_{ij}(\sigma)$, the ratios $\mathrm{SE}(\hat{\gamma}_\lambda)/\hat{\gamma}_\lambda$ do not appear to grow exponentially with σ but the values of $\mathrm{SE}(\hat{\gamma}_\lambda)/\hat{\gamma}_\lambda$ are so large that the 95% confidence interval contains negative values $\hat{\gamma}_\lambda$. Thus one cannot conclude with 95% confidence that γ_λ is positive. The use of $\mathbf{D}_{ij}^{\mathrm{rand}}(\sigma)$ in the OLS parameter estimation procedure does appear to affect the uncertainty associated with the parameter estimate $\hat{\gamma}_\lambda$ as we see in the exponential growth of $\mathrm{SE}(\hat{\gamma}_\lambda)/\hat{\gamma}_\lambda$ with σ for realizations of $\mathbf{D}_{ij}^{\mathrm{rand}}(\sigma)$ in Figure 4.7(c). The ratio $\mathrm{SE}(\hat{\gamma})/\hat{\gamma}$ varies on an exponential scale for both realizations of $\mathbf{D}_{ij}(\sigma)$ and $\mathbf{D}_{ij}^{\mathrm{rand}}(\sigma)$ in Figures 4.7(b) and (d), respectively.

We also considered data at temporal nodes $t_j = 0.6 + \dfrac{1}{120}, 0.6 + \dfrac{2}{120}, \ldots, 0.6 + \dfrac{7}{120}, 20, 40, \ldots, 140$ and spatial nodes $x_i = 0, 0.57$ to understand how sparsity of spatial data affects the inverse problem. For each level of added noise $\sigma = 0.015, 0.030, \ldots, 0.090$, we simulated five realizations of $\mathbf{D}_{ij}(\sigma)$ using (4.16). We also simulated five realizations of $\mathrm{D}_{ij}^{\mathrm{rand}}(\sigma)$ using (4.17) for each level of added noise $\sigma = 0, 0.015, \ldots, 0.090$. For each

Figure 4.4: The points denoted with ^{o} are the difference $\hat{\lambda}_\gamma - \lambda_0$, and the points denoted * are the difference $\hat{\lambda} - \lambda_0$ (a) The result of five realizations of $\mathbf{D}_{ij}(\sigma)$ for values of $\sigma = 0.015, 0.030, \ldots, 0.090$ (b) The result of five realizations of $\mathbf{D}_{ij}^{\mathrm{rand}}(\sigma)$ for values of $\sigma = 0, 0.015, \ldots, 0.090$.
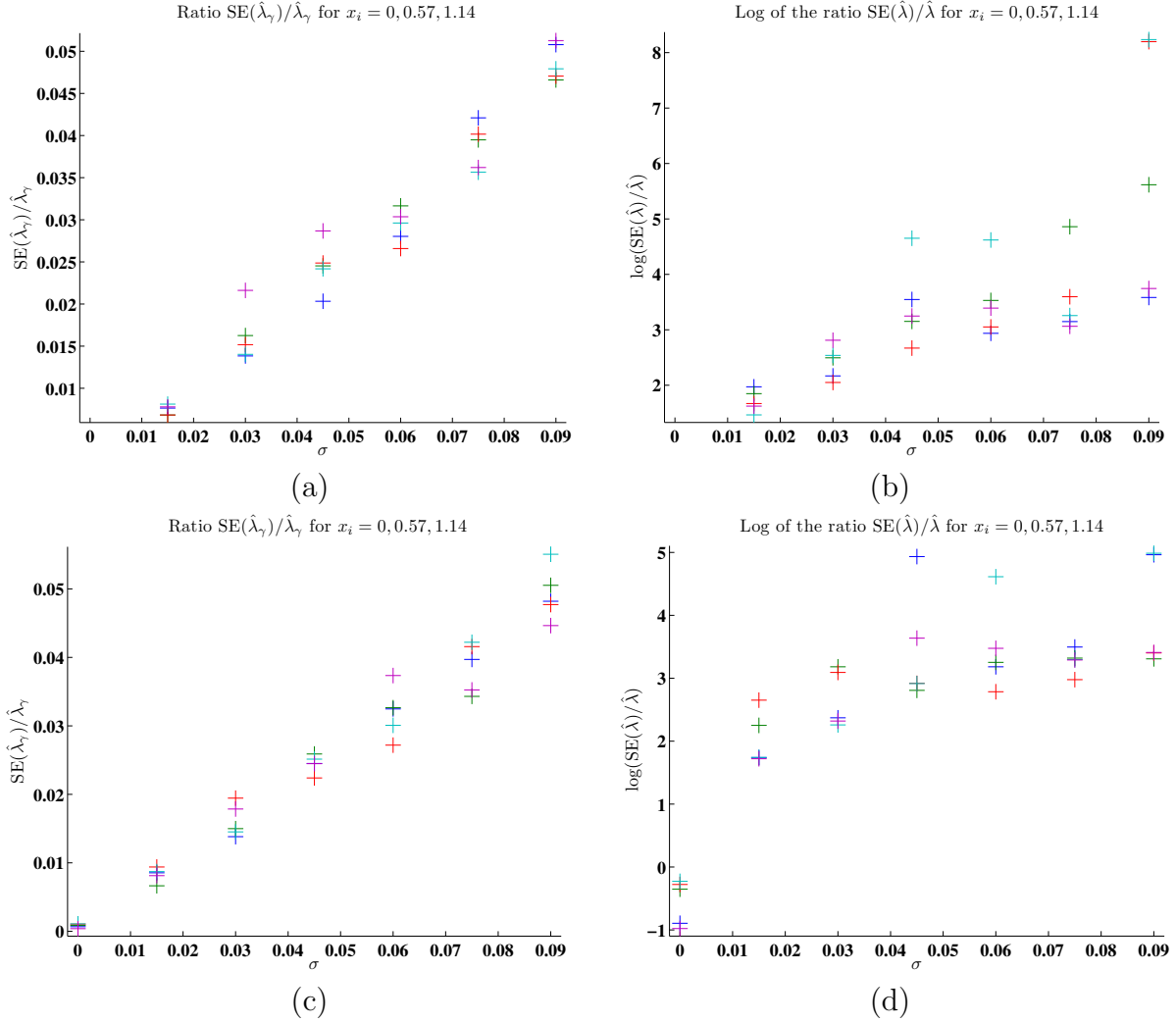
Figure 4.5: (a) The ratio $\mathrm{SE}(\hat{\lambda}_\gamma)/\hat{\lambda}_\gamma$ for five realizations of $\mathbf{D}_{ij}(\sigma)$ for values of $\sigma = 0.015, 0.030, \ldots, 0.090$ (b) The log of the ratio $\log \mathrm{SE}(\hat{\lambda})/\hat{\lambda}$ for five realizations of $\mathbf{D}_{ij}(\sigma)$ for values of $\sigma = 0.015, 0.030, \ldots, 0.090$. (c) The ratio $\mathrm{SE}(\hat{\lambda}_\gamma)/\hat{\lambda}_\gamma$ for five realizations of $\mathbf{D}_{ij}^{\mathrm{rand}}(\sigma)$ for values of $\sigma = 0, 0.015, \ldots, 0.090$. (d) The log of the ratio $\log \mathrm{SE}(\hat{\lambda})/\hat{\lambda}$ for five realizations of $\mathbf{D}_{ij}^{\mathrm{rand}}(\sigma)$ for values of $\sigma = 0, 0.015, 0.030, \ldots, 0.090$.

Figure 4.6: The points denoted with ^{o} are the difference $\hat{\gamma}_\lambda - \gamma_0$, and the points denoted * are the difference $\hat{\gamma} - \gamma_0$ (a) The result of five realizations of $\mathbf{D}_{ij}(\sigma)$ for values of $\sigma = 0.015, 0.030, \ldots, 0.090$ (b) The result of five realizations of $\mathbf{D}_{ij}^{\mathrm{rand}}(\sigma)$ for values of $\sigma = 0, 0.015, \ldots, 0.090$.
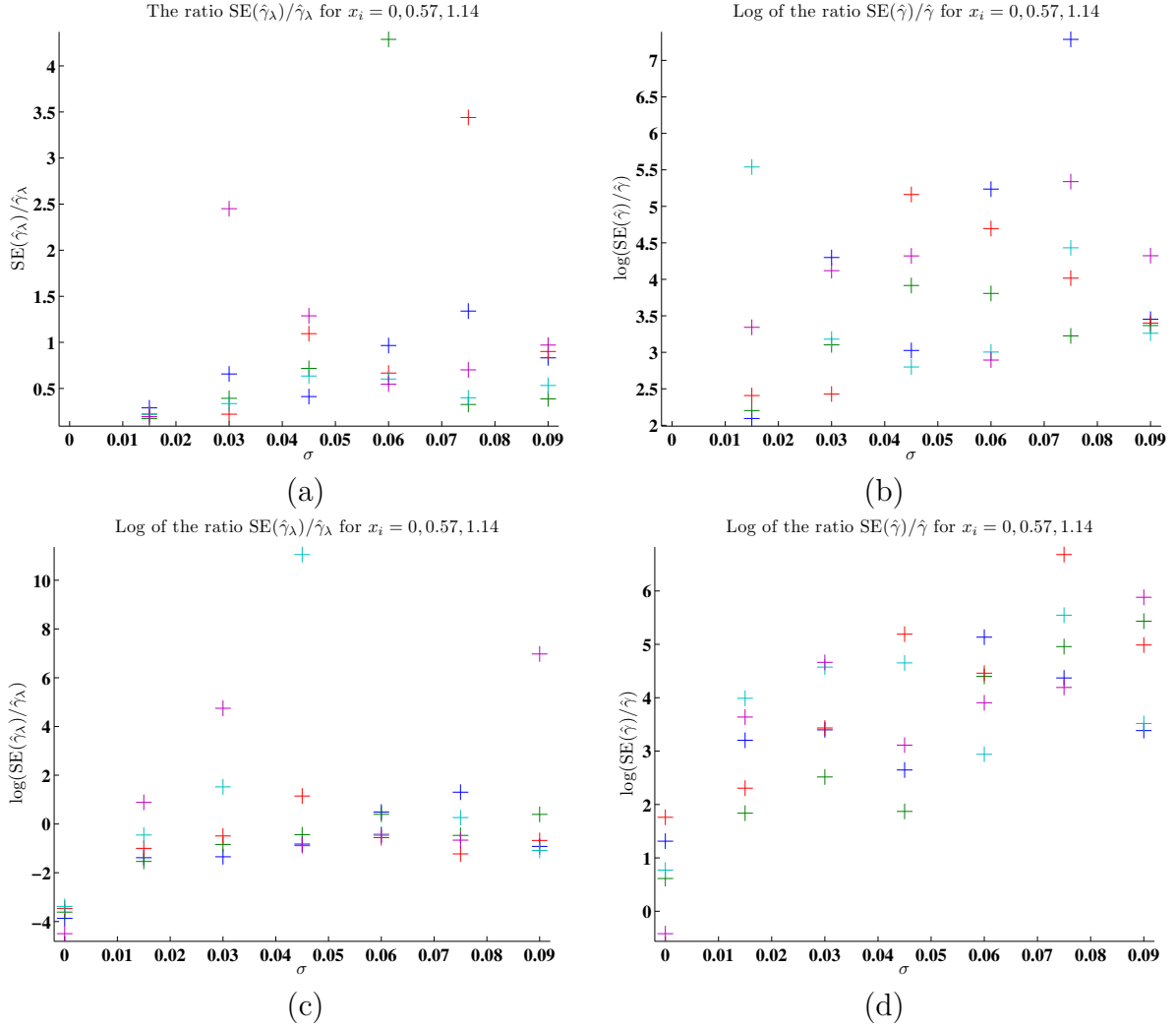
Figure 4.7: (a) The ratio $SE(\hat{\gamma}_\lambda)/\hat{\gamma}_\lambda$ for five realizations of $\mathbf{D}_{ij}(\sigma)$ for values of $\sigma = 0.015, 0.030, \ldots, 0.090$ (b) The log of the ratio $\log SE(\hat{\gamma})/\hat{\gamma}$ for five realizations of $\mathbf{D}_{ij}(\sigma)$ for values of $\sigma = 0.015, 0.030, \ldots, 0.090$. (c) The log of the ratio $\log(SE(\hat{\gamma}_\lambda)/\hat{\gamma}_\lambda)$ for five realizations of $\mathbf{D}_{ij}^{\mathrm{rand}}(\sigma)$ for values of $\sigma = 0, 0.015, \ldots, 0.090$. (d) The log of the ratio $\log SE(\hat{\gamma})/\hat{\gamma}$ for five realizations of $\mathbf{D}_{ij}^{\mathrm{rand}}(\sigma)$ for values of $\sigma = 0, 0.015, 0.030, \ldots, 0.090$.

realization of $\mathbf{D}_{ij}^{\mathrm{rand}}(\sigma)$ a different random geometry Ω is used to solve (4.1) for u_{ij}^{rand} in (4.18). Results from these simulations are given in Figures 4.8–4.13.

For the realizations of $\mathbf{D}_{ij}(\sigma)$, the differences $\hat{\alpha}_\# - \alpha_0$ are plotted in Figure 4.8(a) while these differences for the realizations of $\mathbf{D}_{ij}^{\mathrm{rand}}(\sigma)$ are plotted in Figure 4.8(b). Much like these quantities in Figures 4.2(a) and (b), for each realization the differences $\hat{\alpha}_\lambda - \alpha_0$, $\hat{\alpha}_\gamma - \alpha_0$ and $\hat{\alpha} - \alpha_0$ remain relatively close and are on about the same scale as in Figures 4.2(a) and (b). The ratios $\mathrm{SE}(\hat{\alpha}_\#)/\hat{\alpha}_\#$ for the realizations of $\mathbf{D}_{ij}(\sigma)$ and $\mathbf{D}_{ij}^{\mathrm{rand}}(\sigma)$ are plotted in Figures 4.9(a) and (b), respectively. In both figures, it appears that the ratio $\mathrm{SE}(\hat{\alpha})/\hat{\alpha}$ is larger than the ratios $\mathrm{SE}(\hat{\alpha}_\lambda)/\hat{\alpha}_\lambda$ and $\mathrm{SE}(\hat{\alpha}_\gamma)/\hat{\alpha}_\gamma$. It also appears that the relationship between the ratios $\mathrm{SE}(\hat{\alpha}_\#)/\hat{\alpha}_\#$ and σ is linear as we observed in Figures 4.3(a) and (b) as well. This suggests that for the temporal and spatial nodes that we are considering estimating α is well-posed and there is little difference between using realizations of $\mathbf{D}_{ij}^{\mathrm{rand}}(\sigma)$ and $\mathbf{D}_{ij}(\sigma)$ in the estimation of the parameter α and the estimation of the uncertainty associated with α.

In Figures 4.10(a) and (b), we see that the difference $\hat{\lambda} - \lambda_0$ is larger than $\hat{\lambda}_\gamma - \lambda_0$ for the realizations of $\mathbf{D}_{ij}(\sigma)$ and $\mathbf{D}_{ij}^{\mathrm{rand}}(\sigma)$, respectively. Figure 4.10(b) resembles Figure 4.10(a) which suggests that using realizations of $\mathbf{D}_{ij}^{\mathrm{rand}}(\sigma)$ rather than realizations of $\mathbf{D}_{ij}(\sigma)$ does not have a large effect on the accuracy of the parameter estimates $\hat{\lambda}_\#$. The ratios $\mathrm{SE}(\hat{\lambda}_\gamma)/\hat{\lambda}_\gamma$ appear to be similar for realizations of $\mathbf{D}_{ij}(\sigma)$ (in Figure 4.11(a)) and realizations of $\mathbf{D}_{ij}^{\mathrm{rand}}(\sigma)$ (in Figure 4.11(c)) and seem to vary linearly with σ. The ratios $\mathrm{SE}(\hat{\lambda})/\hat{\lambda}$ are much larger than the ratios $\mathrm{SE}(\hat{\lambda}_\gamma)/\hat{\lambda}_\gamma$, so we plotted $\log(\mathrm{SE}(\hat{\lambda})/\hat{\lambda})$ for the realizations of $\mathbf{D}_{ij}(\sigma)$ in Figure 4.11(b) and for the realizations of $\mathbf{D}_{ij}^{\mathrm{rand}}(\sigma)$ in Figure 4.11(d). This implies that for realizations of $\mathbf{D}_{ij}(\sigma)$ and $\mathbf{D}_{ij}^{\mathrm{rand}}(\sigma)$ estimating γ causes a dramatic increase in the uncertainty associated with the parameter estimate $\hat{\lambda}$ for spatial nodes $x_i = 0, 0.57$. Note that this effect appears to be similar for realizations
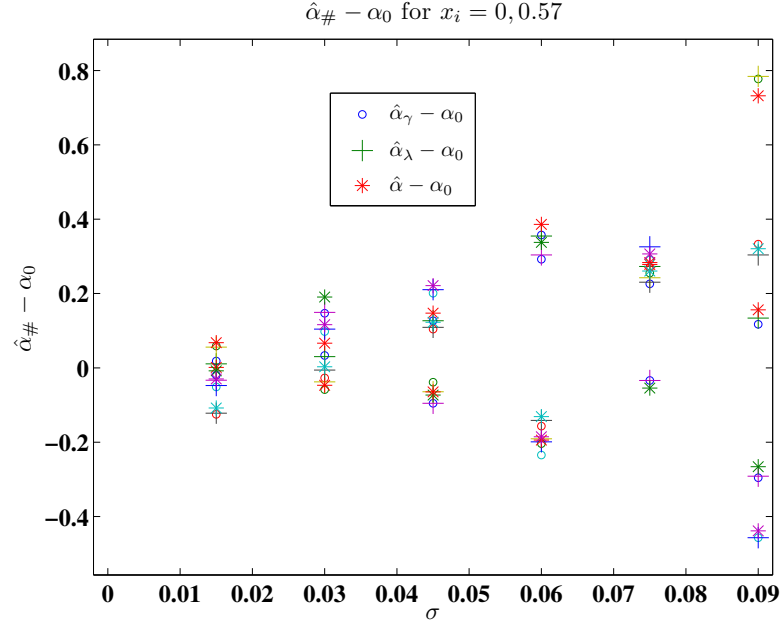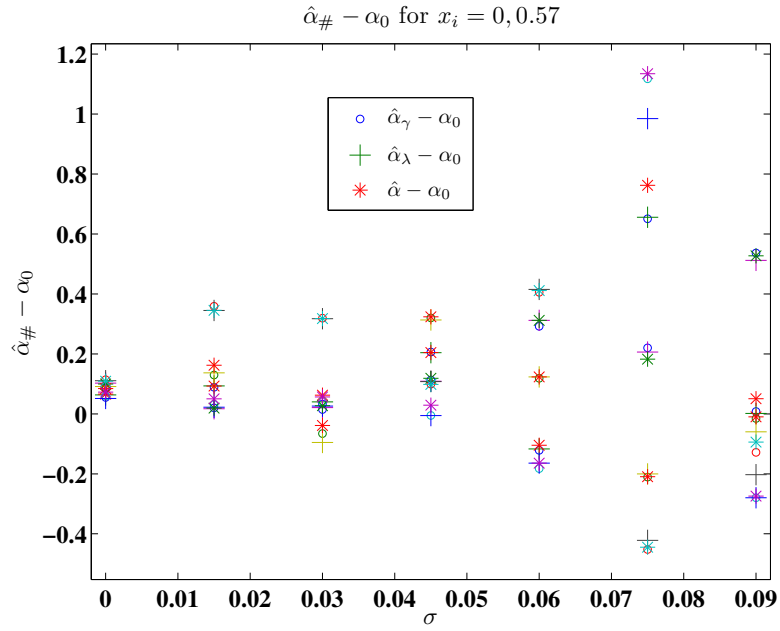
Figure 4.8: The points denoted with ^{o} are the difference $\hat{\alpha}_\gamma - \alpha_0$, the points denoted are the $\hat{\alpha}_\lambda - \alpha_0$, the points denoted * are the difference $\hat{\alpha} - \alpha_0$ (a) The result of five realizations of $\mathbf{D}_{ij}(\sigma)$ for values of $\sigma = 0.015, 0.030, \ldots, 0.090$ (b) The result of five realizations of $\mathbf{D}_{ij}^{\mathrm{rand}}(\sigma)$ for values of $\sigma = 0, 0.015, \ldots, 0.090$.
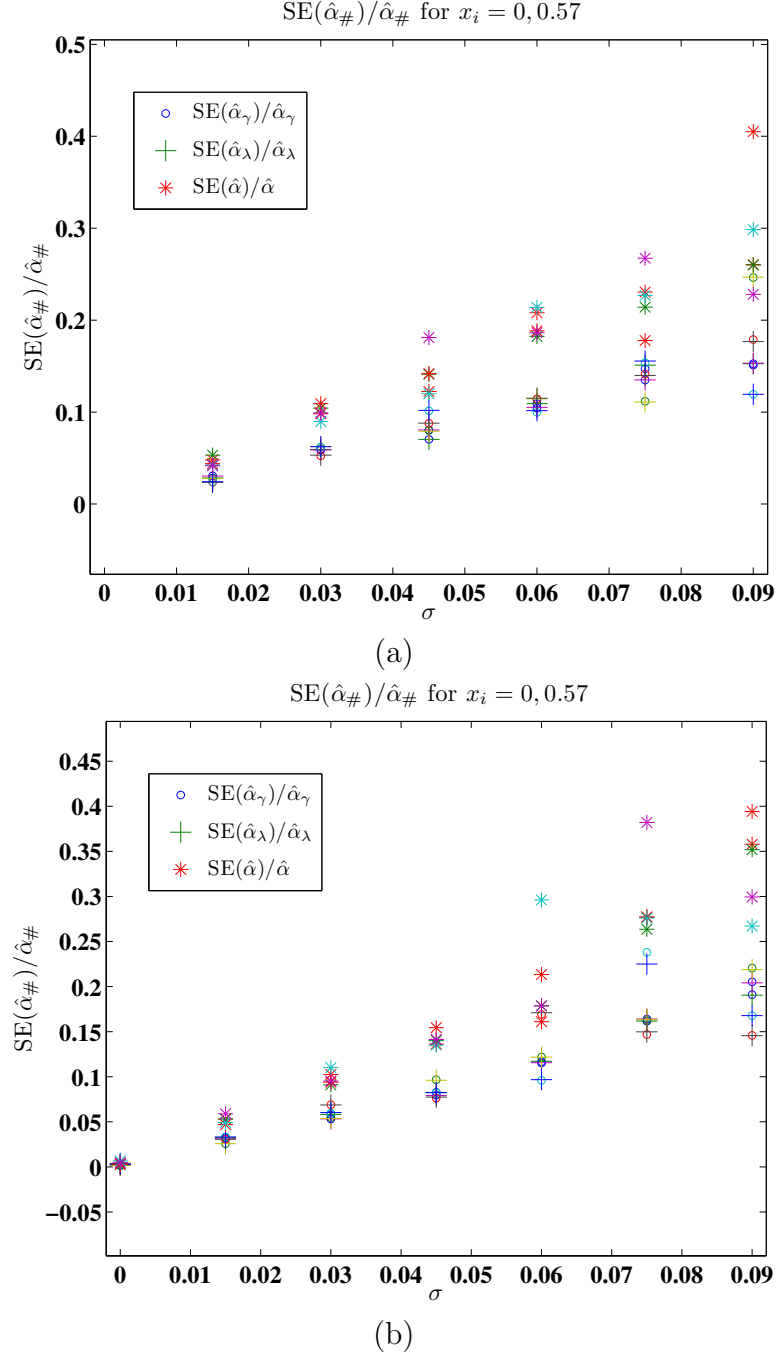
Figure 4.9: The points denoted with ^{o} are the ratio $\mathrm{SE}(\hat{\alpha}_\gamma)/\hat{\alpha}_\gamma$, the points denoted are the $\mathrm{SE}(\hat{\alpha}_\lambda)/\hat{\alpha}_\lambda$, the points denoted * are the difference $\mathrm{SE}(\hat{\alpha})/\hat{\alpha}$ (a) The result of five realizations of $\mathbf{D}_{ij}(\sigma)$ for values of $\sigma = 0.015, 0.030, \ldots, 0.090$ (b) The result of five realizations of $\mathbf{D}_{ij}^{\mathrm{rand}}(\sigma)$ for values of $\sigma = 0, 0.015, \ldots, 0.090$.

of $\mathbf{D}_{ij}(\sigma)$ in Figure 4.11(b) as for realizations of $\mathbf{D}_{ij}^{\mathrm{rand}}(\sigma)$ in Figure 4.11(d).

The estimation of the parameter γ appears to be ill-posed for the spatial nodes $x_i = 0, 0.57$, especially when estimating the parameter set $(\gamma, \alpha, \lambda)$. The differences $\hat{\gamma} - \gamma_0$ are several orders of magnitude larger than the "true" parameter $\gamma_0 = 10^{-3}$ in Figure 4.12(a) (for realizations of $\mathbf{D}_{ij}(\sigma)$) and in Figure 4.6(b) (for realizations of $\mathbf{D}_{ij}^{\mathrm{rand}}(\sigma)$).

For the spatial nodes $x_i = 0, 0.57$, the uncertainty associated with the parameter estimate $\hat{\gamma}_{\#}$ is very large. For all of the examples of $\mathrm{SE}(\hat{\gamma}_{\#})/\hat{\gamma}_{\#}$ in Figures 4.13(a)–(d) we plotted $\log(\mathrm{SE}(\hat{\gamma}_{\#})/\hat{\gamma}_{\#})$ because the variation of $\mathrm{SE}(\hat{\gamma}_{\#})/\hat{\gamma}_{\#}$ was so large for every example. Figures 4.13(a) and (c) depict $\mathrm{SE}(\hat{\gamma}_{\lambda})/\hat{\gamma}_{\lambda}$ for the realizations of $\mathbf{D}_{ij}(\sigma)$ and $\mathbf{D}_{ij}^{\mathrm{rand}}(\sigma)$, respectively. The ratios $\mathrm{SE}(\hat{\gamma}_{\lambda})/\hat{\gamma}_{\lambda}$ are on an exponential scale for realizations of $\mathbf{D}_{ij}(\sigma)$ in Figure 4.13(a) with spatial nodes $x_i = 0, 0.57$ while the ratios $\mathrm{SE}(\hat{\gamma}_{\lambda})/\hat{\gamma}_{\lambda}$ are on a linear scale for realizations of $\mathbf{D}_{ij}(\sigma)$ in Figure 4.7(a) which indicates that sparsity of spatial collection nodes affects the uncertainty associated with the parameter estimates $\hat{\gamma}_{\#}$.
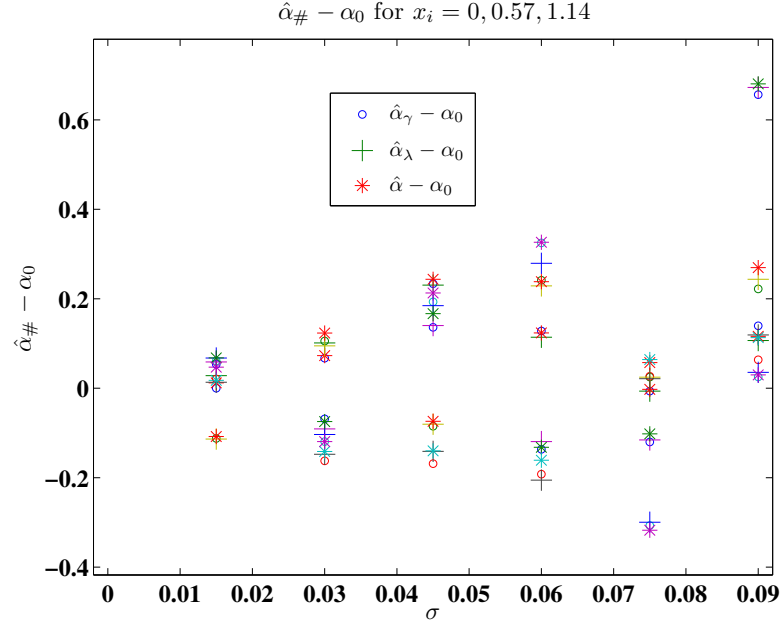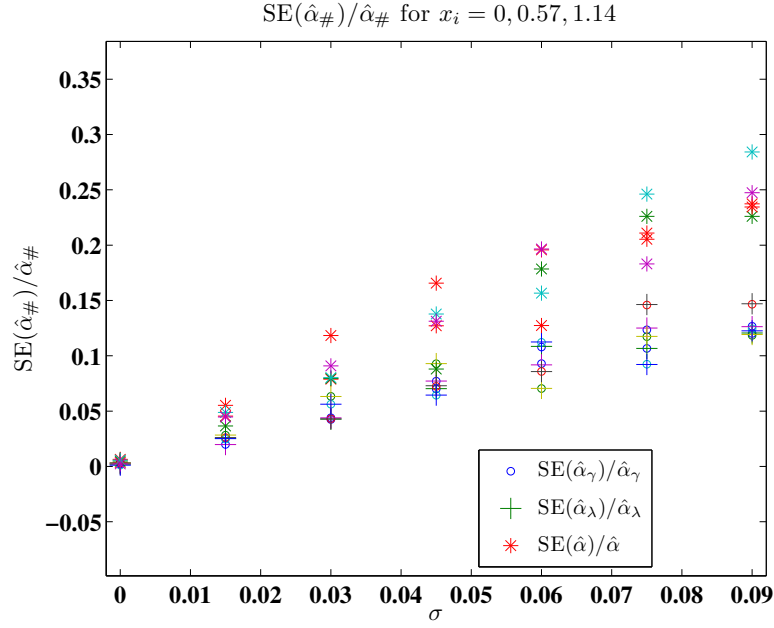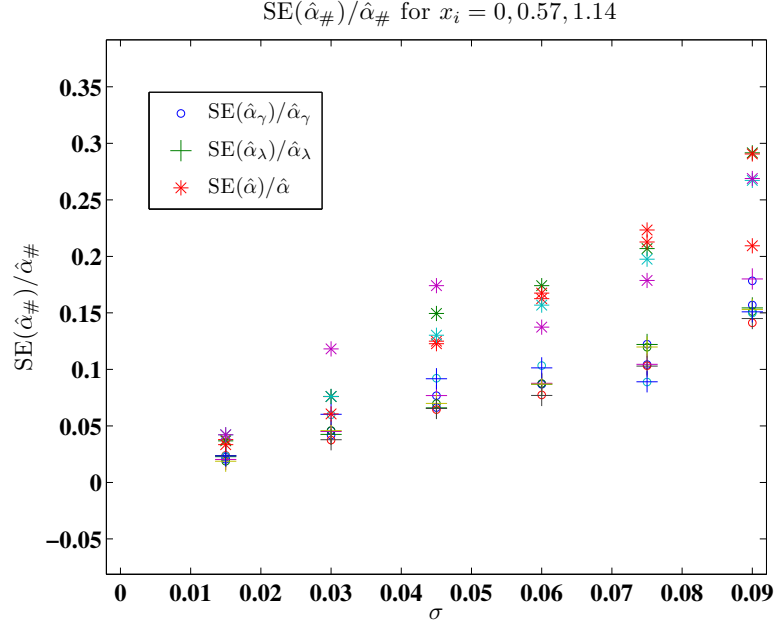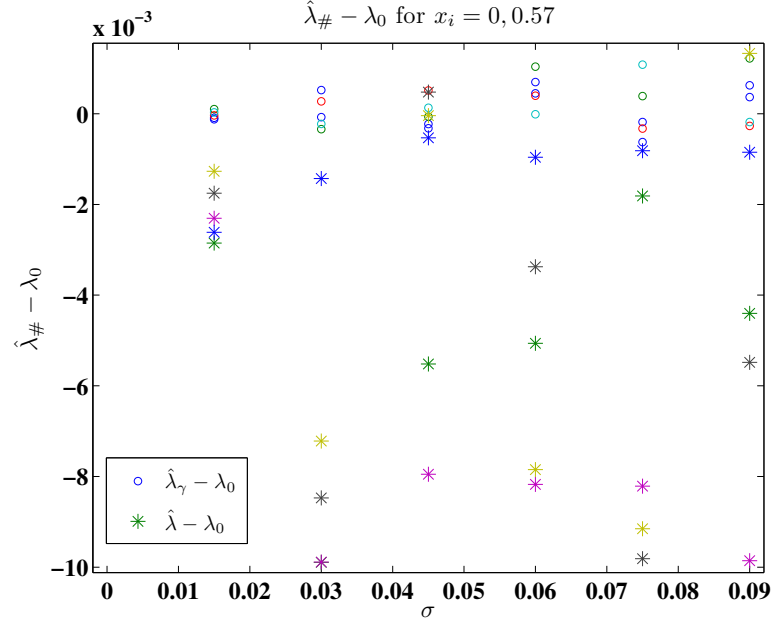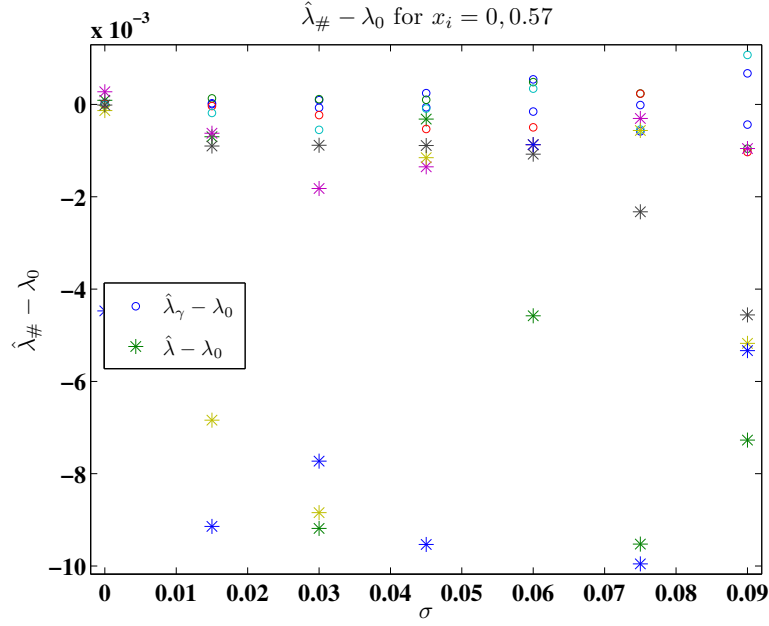
Figure 4.10: The points denoted with ^{o} are the difference $\hat{\lambda}_\gamma - \lambda_0$, and the points denoted * are the difference $\hat{\lambda} - \lambda_0$ (a) The result of five realizations of $\mathbf{D}_{ij}(\sigma)$ for values of $\sigma = 0.015, 0.030, \ldots, 0.090$ (b) The result of five realizations of $\mathbf{D}_{ij}^{\text{rand}}(\sigma)$ for values of $\sigma = 0, 0.015, \ldots, 0.090$.
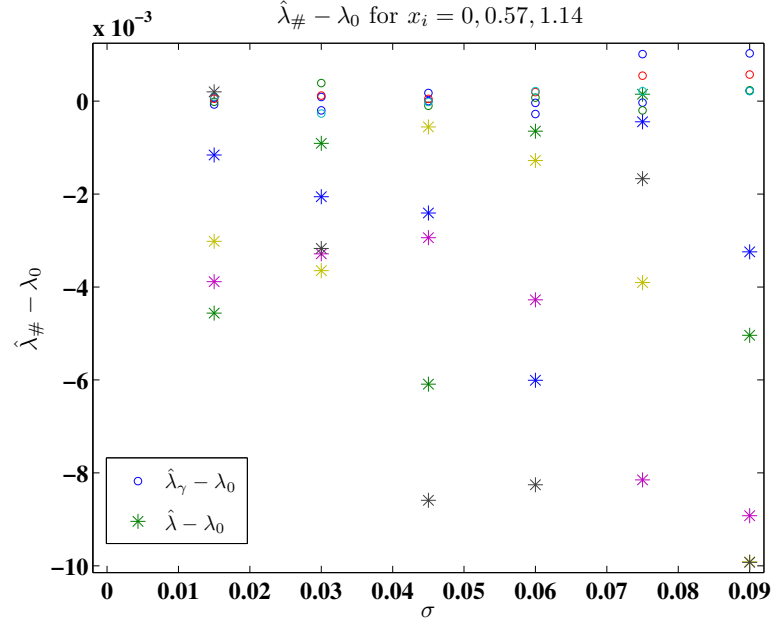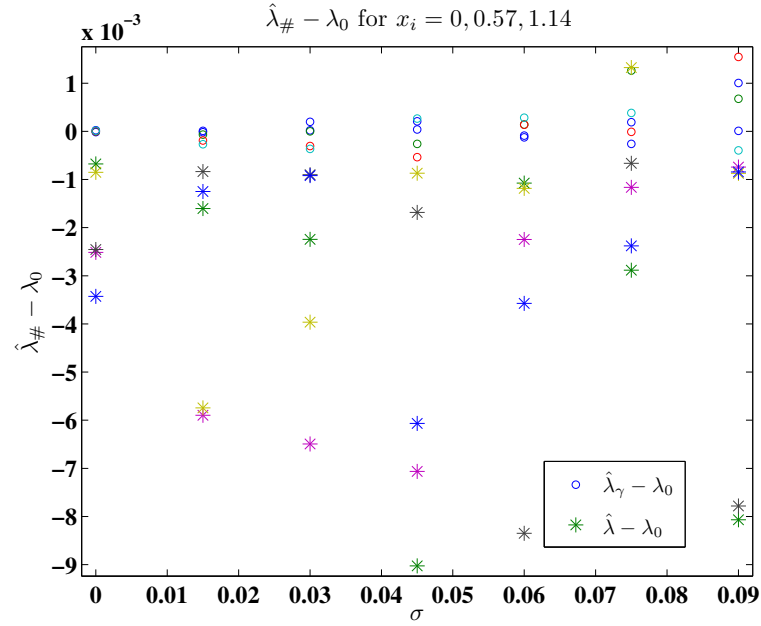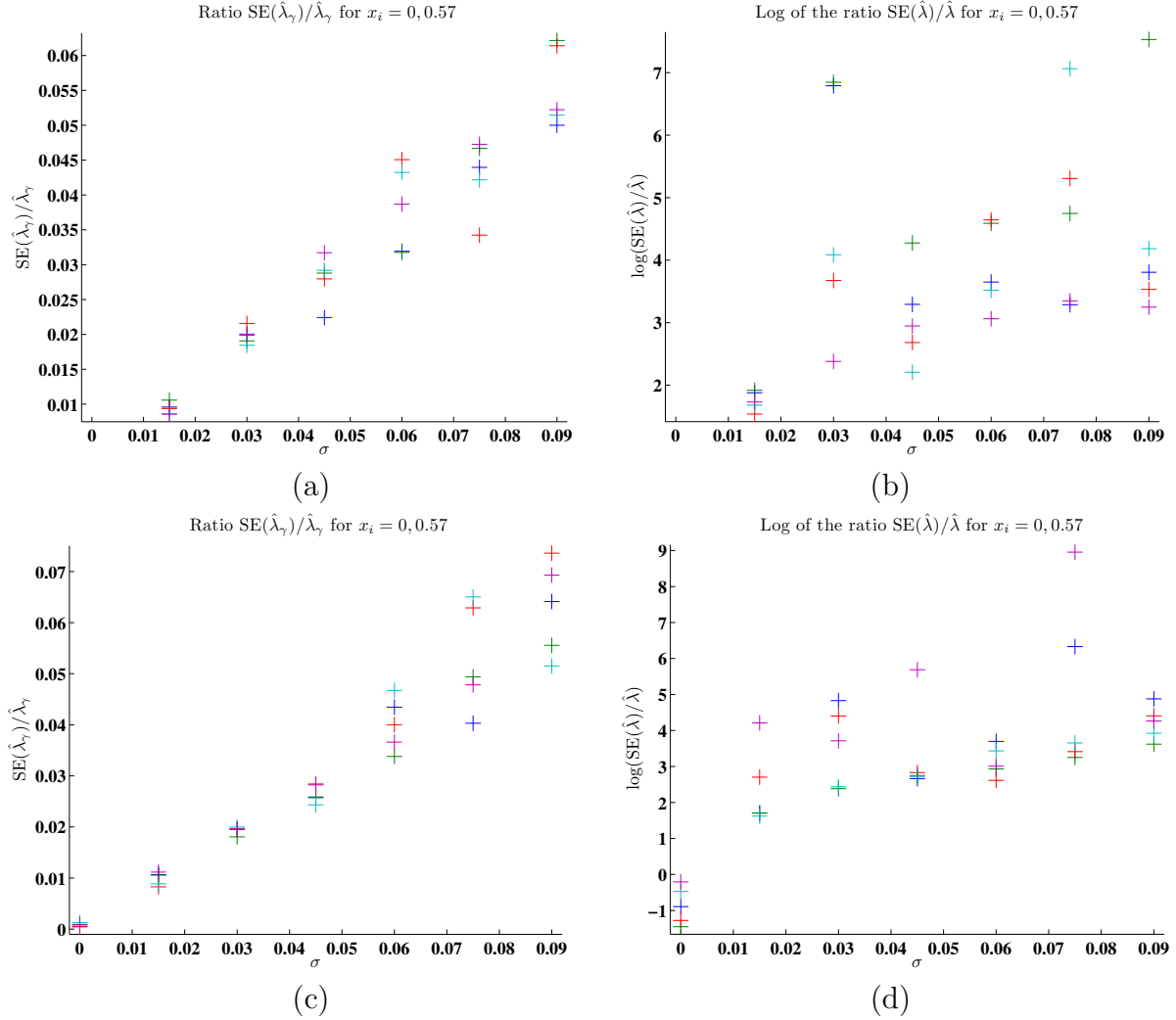
Figure 4.11: (a) The ratio $\text{SE}(\hat{\lambda}_\gamma)/\hat{\lambda}_\gamma$ for five realizations of $\mathbf{D}_{ij}(\sigma)$ for values of $\sigma = 0.015, 0.030, \ldots, 0.090$ (b) The log of the ratio $\log \text{SE}(\hat{\lambda})/\hat{\lambda}$ for five realizations of $\mathbf{D}_{ij}(\sigma)$ for values of $\sigma = 0.015, 0.030, \ldots, 0.090$. (c) The ratio $\text{SE}(\hat{\lambda}_\gamma)/\hat{\lambda}_\gamma$ for five realizations of $\mathbf{D}_{ij}^{\text{rand}}(\sigma)$ for values of $\sigma = 0, 0.015, \ldots, 0.090$. (d) The log of the ratio $\log \text{SE}(\hat{\lambda})/\hat{\lambda}$ for five realizations of $\mathbf{D}_{ij}^{\text{rand}}(\sigma)$ for values of $\sigma = 0, 0.015, 0.030, \ldots, 0.090$.

63

Figure 4.12: The points denoted with $^{\circ}$ are the difference $\hat{\gamma}_\lambda - \gamma_0$, and the points denoted * are the difference $\hat{\gamma} - \gamma_0$ (a) The result of five realizations of $\mathbf{D}_{ij}(\sigma)$ for values of $\sigma = 0.015, 0.030, \ldots, 0.090$ (b) The result of five realizations of $\mathbf{D}_{ij}^{\mathrm{rand}}(\sigma)$ for values of $\sigma = 0, 0.015, \ldots, 0.090$.
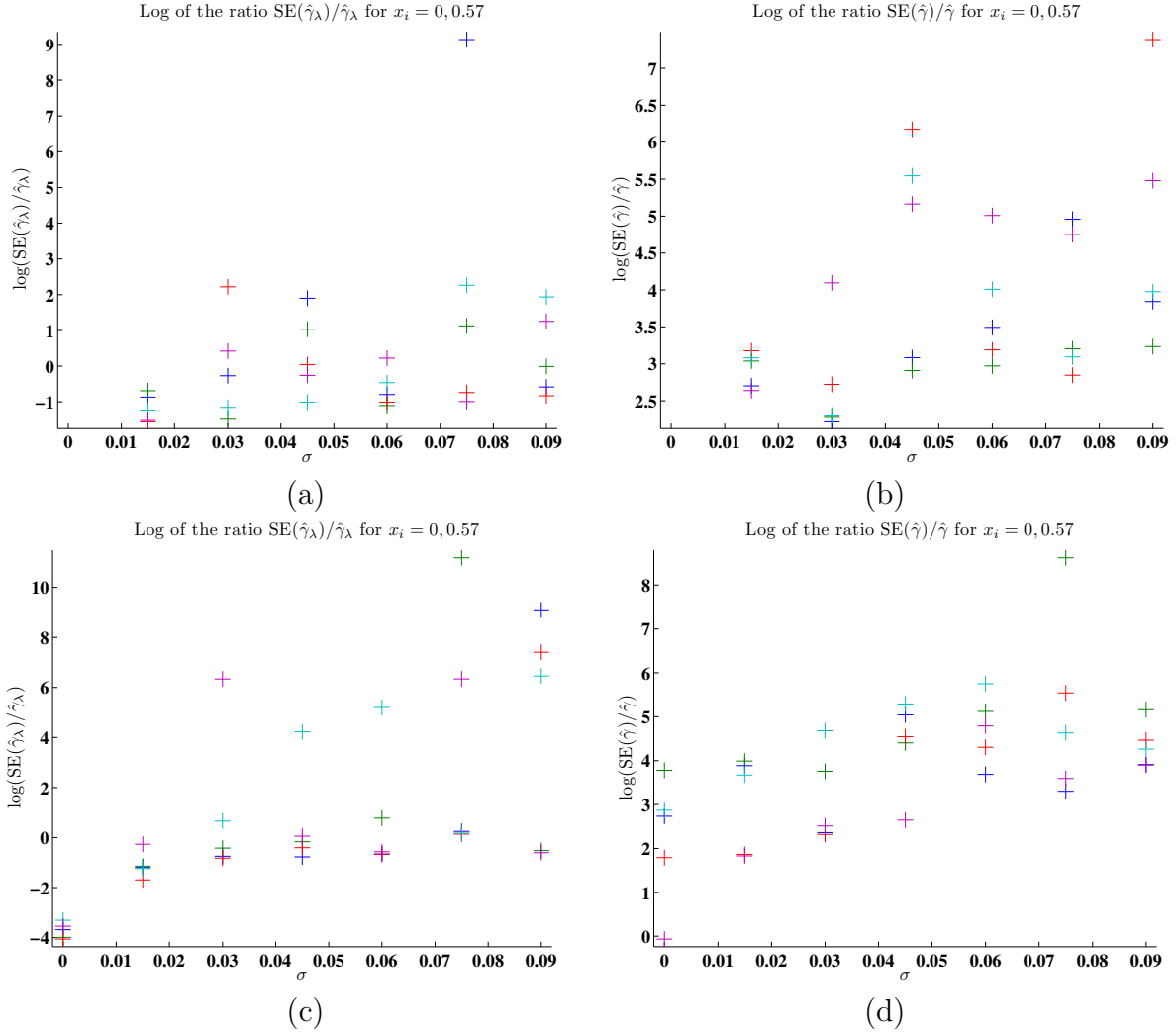
Figure 4.13: (a) The ratio $SE(\hat{\gamma}_\lambda)/\hat{\gamma}_\lambda$ for five realizations of $\mathbf{D}_{ij}(\sigma)$ for values of $\sigma = 0.015, 0.030, \ldots, 0.090$ (b) The log of the ratio $\log SE(\hat{\gamma})/\hat{\gamma}$ for five realizations of $\mathbf{D}_{ij}(\sigma)$ for values of $\sigma = 0.015, 0.030, \ldots, 0.090$. (c) The log of the ratio $\log(SE(\hat{\gamma}_\lambda)/\hat{\gamma}_\lambda)$ for five realizations of $\mathbf{D}_{ij}^{\text{rand}}(\sigma)$ for values of $\sigma = 0, 0.015, \ldots, 0.090$. (d) The log of the ratio $\log SE(\hat{\gamma})/\hat{\gamma}$ for five realizations of $\mathbf{D}_{ij}^{\text{rand}}(\sigma)$ for values of $\sigma = 0, 0.015, 0.03, \ldots, 0.09$.

65

4.3 Generalized Least Squares
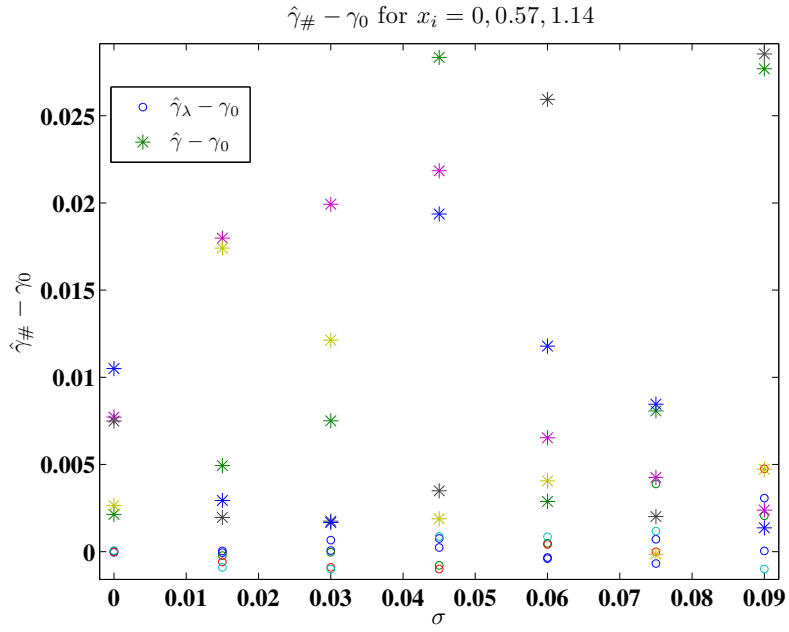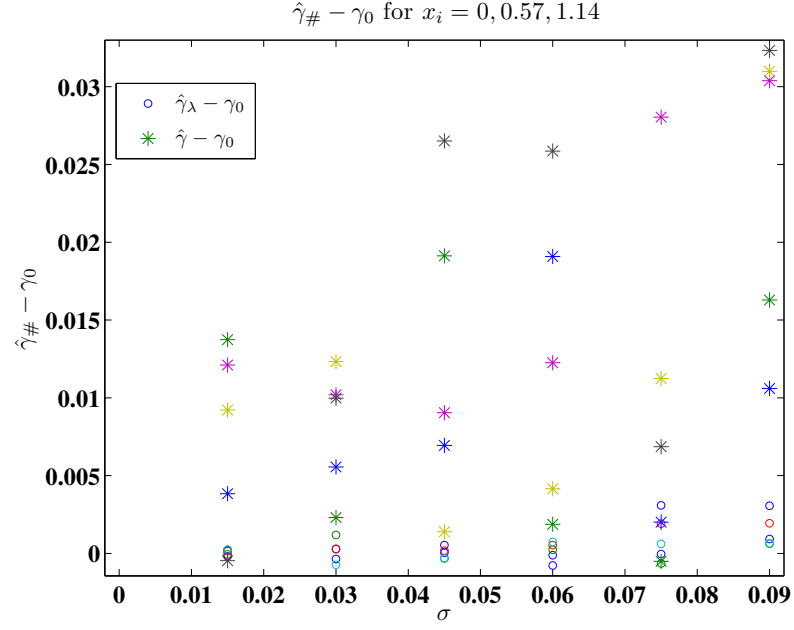
The generalized least squares (GLS) parameter estimation procedure (like the OLS parameter estimation procedure) is based on an underlying statistical model. The error for GLS is assumed to be relative or proportional to the model value. Observations are assumed to be realizations of the random process $\boldsymbol{y}_{ij}$ given by

$$\boldsymbol{y}_{ij} = U_{ij}(\theta_0^{\#})\left(1 + \boldsymbol{\epsilon}_{ij}\right), \tag{4.19}$$

where $\boldsymbol{\epsilon}_{ij}$ is assumed to have constant variance, zero mean, and mutually independent or

$$
\begin{aligned}
E(\boldsymbol{\epsilon}_{ij}) &= 0 \\
Var(\boldsymbol{\epsilon}_{ij}) &= \sigma_0^2 \\
Cov(\boldsymbol{\epsilon}_{ij}, \boldsymbol{\epsilon}_{kh}) &= 0 \text{ for } (i,j) \neq (k,h).
\end{aligned}
\tag{4.20}
$$

Note that in (4.19), the error is given by $U_{ij}(\theta_0^{\#})\boldsymbol{\epsilon}_{ij}$ so it is proportional to the model and the variance is proportional to $U_{ij}^2(\theta_0^{\#})$. Assuming the statistical model given by (4.19), the GLS parameter estimation procedure involves the minimization of the cost functional below

$$J(\theta^{\#}) = \sum_{i=1}^{m} \sum_{j=1}^{n} \left(\frac{U_{ij}(\theta^{\#}) - y_{ij}}{U_{ij}(\theta^{\#})}\right)^2. \tag{4.21}$$

The GLS parameter estimate is given by

$$\hat{\theta}^{\#} = \arg\min_{\theta^{\#} \in \Theta^{\#}} J(\theta^{\#}), \tag{4.22}$$

where $J(\theta^{\#})$ is defined in (4.21). We used the iteratively reweighted least squares method

as described in [7] and [22] to minimize (4.21). The GLS error estimate $\hat{\sigma}_\#^2$ is given by

$$\hat{\sigma}_\#^2 = \frac{J(\hat{\theta}^\#)}{nm - p},\tag{4.23}$$

where again $J(\hat{\theta}^\#)$ is defined in (4.21). The $nm \times nm$ matrix of weights $W(\theta^\#)$ has entries

$$w_{i+m(j-1),i+m(j-1)}(\theta^\#) = \frac{1}{U_{ij}^2(\theta^\#)}\tag{4.24}$$

for $i = 1, 2, \ldots, m$ and $j = 1, 2, \ldots, n$. The GLS covariance matrix estimate $\Sigma(\hat{\theta}^\#)$ is given below

$$\Sigma(\hat{\theta}^\#) = \hat{\sigma}^2 \left(\chi^T(\hat{\theta}^\#) W(\hat{\theta}^\#) \chi(\hat{\theta}^\#) \right)\tag{4.25}$$

where $\chi(\hat{\theta}^\#)$ is the matrix of sensitivities with entries given in (5.29). The standard error estimates are again given by the square roots of the diagonal entries of the covariance matrix

$$\text{SE}(\hat{\theta}_k^\#) = \sqrt{\Sigma_{kk}(\hat{\theta}^\#)}.\tag{4.26}$$

4.3.1 Simulated Generalized Least Squares Data

As in the previous section, we will consider the well-posedness of the GLS parameter estimation procedure by considering the resulting parameter estimates and uncertainty estimates for simulated data. We simulate data motivated the GLS error assumptions in (4.19) and (4.20) using both the solutions of (4.1) u^{rand} and solutions of (4.2) U. In order to consider U the solution of (4.2) as a model solution in the inverse problem, we will simulate data which is given by realizations of $\mathbf{D}_{ij}$ where $\mathbf{D}_{ij}$ is given by

$$\mathbf{D}_{ij}(\sigma) = U_{ij}(10^{-3}, 2.9167, 0.01)\left(1 + \sigma\boldsymbol{\beta}_{ij}\right)\tag{4.27}$$

where $U_{ij}(10^{-3}, 2.9167, 0.01)$ is given by (4.3), and $\boldsymbol{\beta}_{ij}$ follows a standard normal distribution or $\boldsymbol{\beta}_{ij} \sim \mathcal{N}(0, 1^2)$. Again, as in Section 4.2.1, we consider spatial nodes $x_i = 0, 0.57, 1.14$ and $x_i = 0, 0.57$ and temporal nodes $t_j = 0.6 + \dfrac{1}{120}, 0.6 + \dfrac{2}{120}, \ldots, 0.6 + \dfrac{7}{120}, 20, 40, \ldots, 140$. We analyzed five realizations of $\mathbf{D}_{ij}(\sigma)$ for each value of $\sigma = 0.02, 0.05, 0.10$.

We also consider data which is generated using solutions of (4.1) and motivated by the GLS assumptions with realizations of the random process

$$\mathbf{D}_{ij}^{\mathrm{rand}}(\sigma) = u_{ij}^{\mathrm{rand}}(1 + \sigma\boldsymbol{\beta}_{ij}), \tag{4.28}$$

where u_{ij}^{rand} is defined in (4.18), and $\boldsymbol{\beta}_{ij}$ is a random variable sampled from a standard normal distribution or $\boldsymbol{\beta}_{ij} \sim \mathcal{N}(0, 1^2)$. We calculated five realizations of $\mathbf{D}_{ij}^{\mathrm{rand}}(\sigma)$ for each value of $\sigma = 0, 0.02, 0.05, 0.10$.

For both sets of simulations, we calculate the parameter estimates $\hat{\theta}^{\#}$, or $\hat{\theta}^{\lambda} = (\hat{\gamma}_{\lambda}, \hat{\alpha}^{\lambda})$, $\hat{\theta}^{\gamma} = (\hat{\alpha}_{\gamma}, \hat{\lambda}^{\gamma})$ and $\hat{\theta} = (\hat{\gamma}, \hat{\alpha}, \hat{\lambda})$ as defined in (4.22) by minimizing (4.21). We also calculate $\mathrm{SE}(\hat{\theta}^{\#})$ using (4.26).

As in Section 4.3.1, we consider the accuracy of the inverse problem by investigating $\hat{\theta}^{\#} - \theta_0^{\#}$ and the uncertainty associated with the inverse problem by investigating the ratios $\mathrm{SE}(\hat{\theta}^{\#})/\hat{\theta}^{\#}$. In Figures 4.14–4.19, we consider these simulations with spatial nodes $x_i = 0, 0.57, 1.14$. Figure 4.14(a) depicts $\hat{\alpha}_{\#} - \alpha_0$ for five realizations of $\mathbf{D}_{ij}(\sigma)$ for each value of $\sigma = 0.02, 0.05, 0.10$. The values of $\alpha_{\#} - \alpha_0$ in Figure 4.14(b) for five realizations of $\mathbf{D}_{ij}^{\mathrm{rand}}(\sigma)$ for each value of $\sigma = 0, 0.02, 0.05, 0.10$ appear to be smaller than those in Figure 4.14(a). This suggests that the GLS parameter estimation procedure predicts $\hat{\alpha}_{\#}$ more accurately for data generated by realizations $\mathbf{D}_{ij}(\sigma)$ than for data generated by realizations of $\mathbf{D}_{ij}^{\mathrm{rand}}(\sigma)$.

To consider the uncertainty associated with the parameter estimates $\hat{\alpha}_\# - \alpha_0$, we plotted the ratio $\text{SE}(\hat{\alpha}_\#)/\hat{\alpha}_\#$ in Figure 4.15(a) for realizations of $\mathbf{D}_{ij}(\sigma)$ and in Figure 4.15(b) for realizations of $\mathbf{D}_{ij}^{\text{rand}}(\sigma)$. The ratios $\text{SE}(\hat{\alpha}_\#)/\hat{\alpha}_\#$ appear to be linear in σ for realizations of $\mathbf{D}_{ij}(\sigma)$ and $\mathbf{D}_{ij}^{\text{rand}}(\sigma)$ with similar slopes. It appears that there is little difference between using realizations of $\mathbf{D}_{ij}(\sigma)$ and realizations of $\mathbf{D}_{ij}^{\text{rand}}(\sigma)$ in the GLS estimate of the uncertainty associated with the parameter estimate $\hat{\alpha}_\#$.

We plotted the differences $\hat{\lambda}_\# - \lambda_0$ for the realizations of $\mathbf{D}_{ij}(\sigma)$ in Figure 4.16(a) and the realizations of $\mathbf{D}_{ij}^{\text{rand}}(\sigma)$ in Figure 4.16(b). The differences between $\hat{\lambda}_\gamma$ and λ_0 are very small for both realizations of $\mathbf{D}_{ij}(\sigma)$ in Figure 4.16(a) and realizations of $\mathbf{D}_{ij}^{\text{rand}}(\sigma)$ in Figure 4.16(b). The difference $\hat{\lambda} - \lambda_0$ (depicted in Figure 4.16(a) for realizations of $\mathbf{D}_{ij}(\sigma)$ and Figure 4.16(b) for realizations of $\mathbf{D}_{ij}^{\text{rand}}(\sigma)$) has a much larger magnitude than the magnitude of the difference $\hat{\lambda}_\gamma - \lambda_0$. This suggests as in Section 4.2.1 estimating γ detracts from the accuracy GLS estimate of the parameter λ. This is because, as we observed in Section 4.2.1, if we make the transformation $U = e^{-\gamma t} Z$ in the partial differential equation (4.2), we get the same partial differential equation but without the zero order term $p_V \gamma U$ (4.13). Thus, if we write the GLS cost functional as

$$J(U(t_j, \vec{x}_i; \theta), \mathrm{D}_{ij}) = \sum_{i=1}^{m} \sum_{j=1}^{n} \left(\frac{U(t_j, \vec{x}_i; \theta) - \mathrm{D}_{ij}}{U(t_j, \vec{x}_i; \theta)} \right)^2 \tag{4.29}$$

then the cost functional can be written as $J(Z(t_j, \vec{x}_i; \theta), e^{\gamma t_j} \mathrm{D}_{ij})$. Estimating γ adds an extra level of time dependence to the error which would violate the error assumptions in (4.20). We further see the effect of estimating γ on the uncertainty associated with the parameter estimate $\hat{\lambda}$. In Figure 4.17(a) we plotted the ratio $\text{SE}(\hat{\lambda}_\gamma)/\hat{\lambda}_\gamma$ versus σ for realizations of $\mathbf{D}_{ij}(\sigma)$ and the ratio $\text{SE}(\hat{\lambda}_\gamma)/\hat{\lambda}_\gamma$ versus σ in Figure 4.17(c). The ratios $\text{SE}(\hat{\lambda}_\gamma)/\hat{\lambda}_\gamma$ in both of these examples appear to be linearly dependent on σ. When the

Figure 4.14: The results of realizations of simulated data with temporal nodes $t_j = 0.6 + \dfrac{1}{120}, 0.6 + \dfrac{2}{120}, \ldots, \dfrac{7}{120}, 20, 40, \ldots, 140$ and spatial nodes $x_i = 0, 0.57, 1.14$. The points denoted with ^{o} are the difference $\hat{\alpha}_\gamma - \alpha_0$, the points denoted are the $\hat{\alpha}_\lambda - \alpha_0$, the points denoted * are the difference $\hat{\alpha} - \alpha_0$ (a) The result of five realizations of $\mathbf{D}_{ij}(\sigma)$ for values of $\sigma = 0.02, 0.05, 0.10$ (b) The result of five realizations of $\mathbf{D}_{ij}^{\mathrm{rand}}(\sigma)$ for values of $\sigma = 0, 0.02, 0.05, 0.10$.

70

Figure 4.15: The results of realizations of simulated data with temporal nodes $t_j = 0.6 + \dfrac{1}{120}, 0.6 + \dfrac{2}{120}, \ldots, \dfrac{7}{120}, 20, 40, \ldots, 140$ and spatial nodes $x_i = 0, 0.57, 1.14$. The points denoted with ^{o} are the ratio $\mathrm{SE}(\hat{\alpha}_\gamma)/\hat{\alpha}_\gamma$, the points denoted are the $\mathrm{SE}(\hat{\alpha}_\lambda)/\hat{\alpha}_\lambda$, the points denoted * are the difference $\mathrm{SE}(\hat{\alpha})/\hat{\alpha}$ (a) The result of five realizations of $\mathbf{D}_{ij}(\sigma)$ for values of $\sigma = 0.02, 0.05, 0.10$ (b) The result of five realizations of $\mathbf{D}_{ij}^{\mathrm{rand}}(\sigma)$ for values of $\sigma = 0, 0.02, 0.05, 0.10$.

71

full parameter set $\hat{\theta}$ is estimated, we see that the ratio $\mathrm{SE}(\hat{\lambda}_\gamma)/\hat{\lambda}_\gamma$ varies exponentially with σ in Figures (b) and (d) in which we plotted $\log(\mathrm{SE}(\hat{\alpha})/\hat{\alpha})$ versus σ for realizations of $\mathbf{D}_{ij}(\sigma)$ and $\mathbf{D}_{ij}^{\mathrm{rand}}(\sigma)$, respectively.

Figure 4.16: The results of realizations of simulated data with temporal nodes $t_j = 0.6 + \dfrac{1}{120}, 0.6 + \dfrac{2}{120}, \ldots, \dfrac{7}{120}, 20, 40, \ldots, 140$ and spatial nodes $x_i = 0, 0.57, 1.1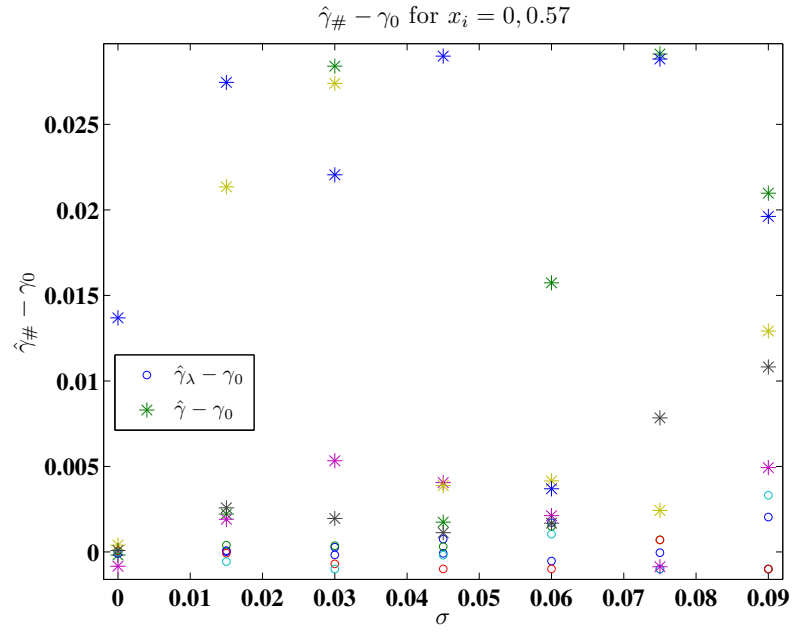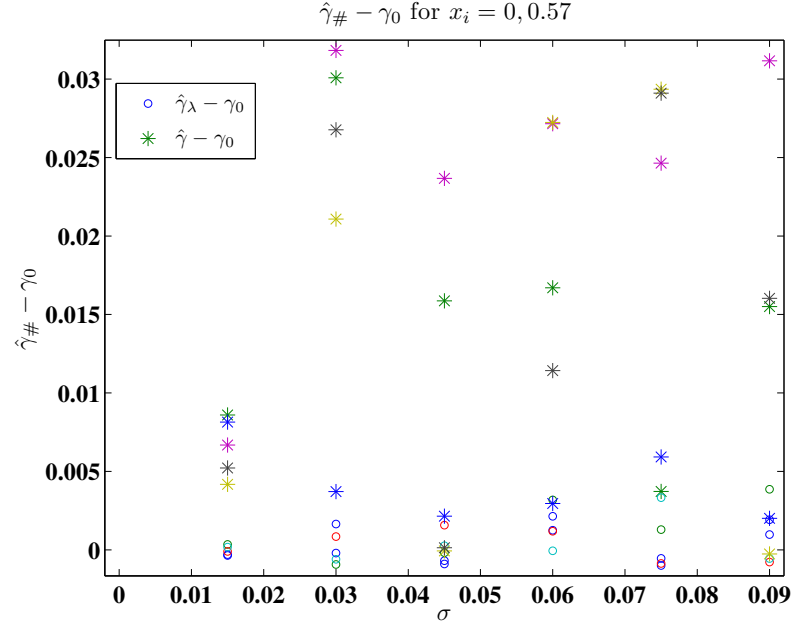4$. The points denoted with ^{o} are the difference $\hat{\lambda}_\gamma - \lambda_0$, and the points denoted * are the difference $\hat{\lambda} - \lambda_0$ (a) The result of five realizations of $\mathbf{D}_{ij}(\sigma)$ for values of $\sigma = 0.02, 0.05, 0.10$ (b) The result of five realizations of $\mathbf{D}_{ij}^{\mathrm{rand}}(\sigma)$ for values of $\sigma = 0, 0.02, 0.05, 0.10$.

73

Figure 4.17: The results of realizations of simulated data with temporal nodes $t_j = 0.6 + \dfrac{1}{120}, 0.6 + \dfrac{2}{120}, \dots, \dfrac{7}{120}, 20, 40, \dots, 140$ and spatial nodes $x_i = 0, 0.57, 1.14$. (a) The ratio $\mathrm{SE}(\hat{\lambda}_\gamma)/\hat{\lambda}_\gamma$ for five realizations of $\mathbf{D}_{ij}(\sigma)$ for values of $\sigma = 0.02, 0.05, 0.10$ (b) The log of the ratio $\log \mathrm{SE}(\hat{\lambda})/\hat{\lambda}$ for five realizations of $\mathbf{D}_{ij}(\sigma)$ for values of $\sigma = 0.02, 0.05, 0.10$. (c) The ratio $\mathrm{SE}(\hat{\lambda}_\gamma)/\hat{\lambda}_\gamma$ for five realizations of $\mathbf{D}_{ij}^{\mathrm{rand}}(\sigma)$ for values of $\sigma = 0, 0.02, 0.05, 0.10$. (d) The log of the ratio $\log \mathrm{SE}(\hat{\lambda})/\hat{\lambda}$ for five realizations of $\mathbf{D}_{ij}^{\mathrm{rand}}(\sigma)$ for values of $\sigma = 0, 0.02, 0.05, 0.10$.

74

We also examined the difference between $\hat{\gamma}_\# - \gamma_0$ in Figures 4.18(a) and (b). In Figure 4.18(a), we plotted $\hat{\gamma}_\# - \gamma_0$ for realizations of $\mathbf{D}_{ij}(\sigma)$. In Figure 4.18(b), we plotted $\gamma_\# - \gamma_0$. In both Figure 4.18(a) and (b), $|\hat{\gamma}_\lambda - \gamma_0|$ is several orders of magnitude less than $|\hat{\gamma} - \gamma_0|$. Thus by estimating the entire parameter set $\hat{\theta}$, we gain inaccuracy of our estimate of $\hat{\gamma}$. Also, the differences $|\hat{\gamma} - \gamma_0|$ are an order of magnitude greater than the parameter itself $\gamma_0 = 10^{-3}$. In Figures 4.19(a)–(b), we see that the uncertainty associated with the parameter estimate $\hat{\gamma}_\#$ varies exponentially with σ. Figure 4.19(a) and (c), we plotted $\log(\mathrm{SE}(\hat{\gamma}_\lambda)/\hat{\gamma}_\lambda)$ for realizations of $\mathbf{D}_{ij}(\sigma)$ and $\mathbf{D}_{ij}^{\mathrm{rand}}(\sigma)$, respectively. In Figures 4.19(b) and (d), we see that $\log(\mathrm{SE}(\hat{\gamma})/\hat{\gamma})$ is larger for realizations of $\mathbf{D}_{ij}(\sigma)$ (in (b)) than for realizations of $\mathbf{D}_{ij}^{\mathrm{rand}}(\sigma)$ (in (d)) though $\log(\mathrm{SE}(\hat{\gamma})/\hat{\gamma})$ (in Figures 4.19(b) and (d)) appears to be larger than $\log(\mathrm{SE}(\hat{\gamma}_\lambda)/\hat{\gamma}_\lambda)$ (in Figure 4.19(a) and (c)).

$\hat{\gamma}_{\#} - \gamma_0$ for $x_i = 0, 0.57, 1.14$

(a)

$\hat{\gamma}_{\#} - \gamma_0$ for $x_i = 0, 0.57, 1.14$

(b)
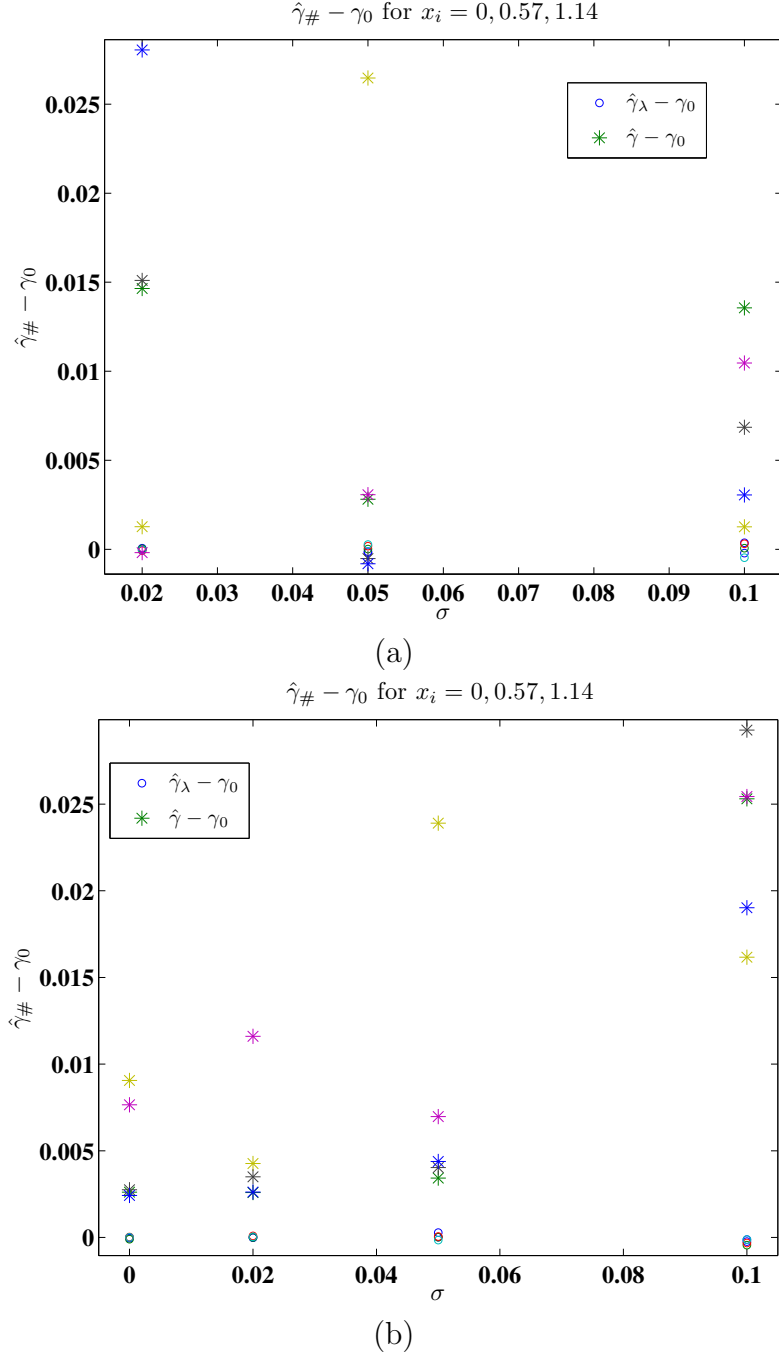
Figure 4.18: The results of realizations of simulated data with temporal nodes $t_j = 0.6 + \dfrac{1}{120}, 0.6 + \dfrac{2}{120}, \ldots, \dfrac{7}{120}, 20, 40, \ldots, 140$ and spatial nodes $x_i = 0, 0.57, 1.14$. The points denoted with ^{o} are the difference $\hat{\gamma}_{\lambda} - \gamma_0$, and the points denoted * are the difference $\hat{\gamma} - \gamma_0$ (a) The result of five realizations of $\mathbf{D}_{ij}(\sigma)$ for values of $\sigma = 0.02, 0.05, 0.10$ (b) The result of five realizations of $\mathbf{D}_{ij}^{\mathrm{rand}}(\sigma)$ for values of $\sigma = 0, 0.02, 0.05, 0.10$.

76
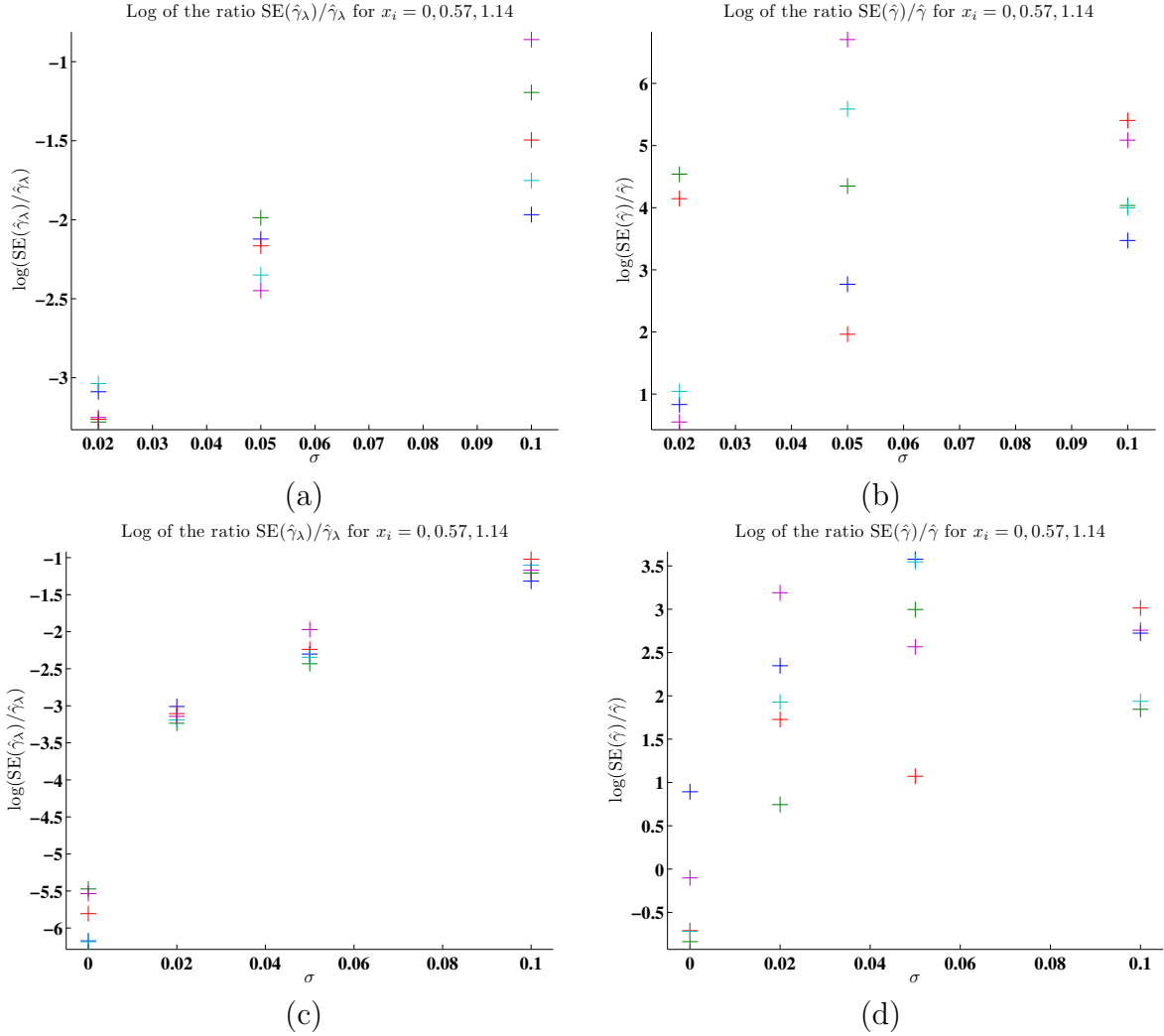
Figure 4.19: The results of realizations of simulated data with temporal nodes $t_j = 0.6 + \dfrac{1}{120}, 0.6 + \dfrac{2}{120}, \ldots, \dfrac{7}{120}, 20, 40, \ldots, 140$ and spatial nodes $x_i = 0, 0.57, 1.14$. (a) The log of the ratio $\log(\mathrm{SE}(\hat{\gamma}_\lambda)/\hat{\gamma}_\lambda)$ for five realizations of $\mathbf{D}_{ij}(\sigma)$ for values of $\sigma = 0.02, 0.05, 0.10$ (b) The log of the ratio $\log(\mathrm{SE}(\hat{\gamma})/\hat{\gamma})$ for five realizations of $\mathbf{D}_{ij}(\sigma)$ for values of $\sigma = 0.02, 0.05, 0.10$. (c) The log of the ratio $\log(\mathrm{SE}(\hat{\gamma}_\lambda)/\hat{\gamma}_\lambda)$ for five realizations of $\mathbf{D}_{ij}^{\mathrm{rand}}(\sigma)$ for values of $\sigma = 0, 0.02, 0.05, 0.10$. (d) The log of the ratio $\log \mathrm{SE}(\hat{\gamma})/\hat{\gamma}$ for five realizations of $\mathbf{D}_{ij}^{\mathrm{rand}}(\sigma)$ for values of $\sigma = 0, 0.02, 0.05, 0.10$.

77

We also considered realizations of $\mathbf{D}_{ij}(\sigma)$ (given by (4.27)) and $\mathbf{D}_{ij}^{\text{rand}}(\sigma)$ (given by (4.28)) for spatial nodes $x_i = 0, 0.57$ and the same temporal nodes $t_j = 0.6 + \frac{1}{120}, 0.6 + \frac{2}{120}, \ldots, \frac{7}{120}, 20, 40, \ldots, 140$. The results of these realizations are depicted in Figures 4.20–4.25.

We see that for realizations of $\mathbf{D}_{ij}(\sigma)$ and $\mathbf{D}_{ij}^{\text{rand}}(\sigma)$ the accuracy of the GLS parameter estimation procedure for the parameter α is similar for the two random processes. We see this in Figures 4.20(a) and (b) though it does appear that one realization of $\mathbf{D}_{ij}^{\text{rand}}(0.10)$ produced large values of $\hat{\alpha}_\lambda$, $\hat{\alpha}_\gamma$, and $\hat{\alpha}$ in Figure 4.20(b). In Figures 4.21(b), we see this extreme realization of $\mathbf{D}_{ij}^{\text{rand}}(0.10)$ also produced large ratios $\text{SE}(\hat{\alpha}_\#)/\hat{\alpha}_\#$. Other than this extreme realization, the ratios $\text{SE}(\hat{\alpha}_\#)/\hat{\alpha}_\#$ for realizations of $\mathbf{D}_{ij}(\sigma)$ (in Figure 4.21(a)) and $\mathbf{D}_{ij}^{\text{rand}}(\sigma)$ (in Figure 4.21(b)) appear to have similar linear dependence on σ.

The differences $\hat{\lambda}_\# - \lambda_0$ are depicted in Figures 4.22(a) and (b) for realizations of $\mathbf{D}_{ij}(\sigma)$ and $\mathbf{D}_{ij}^{\text{rand}}(\sigma)$, respectively. Again, we see similar results for realizations of $\mathbf{D}_{ij}(\sigma)$ and realizations of $\mathbf{D}_{ij}^{\text{rand}}(\sigma)$. We also note, that as was the case for spatial nodes $x_i = 0, 0.57, 1.14$ in Figure 4.16(a) and (b), $|\hat{\lambda} - \lambda_0|$ is much larger than $|\hat{\lambda}_\gamma - \lambda_0|$ for both realizations of $\mathbf{D}_{ij}(\sigma)$ and realizations of $\mathbf{D}_{ij}^{\text{rand}}(\sigma)$. The ratio $\text{SE}(\hat{\lambda}_\gamma)/\hat{\lambda}_\gamma$ appears to vary linearly with σ for both realizations of $\mathbf{D}_{ij}(\sigma)$ (in Figure 4.23(a)) and realizations of $\mathbf{D}_{ij}^{\text{rand}}(\sigma)$ (in Figure 4.23(c)), while the dependence of $\text{SE}(\hat{\lambda})/\hat{\lambda}$ is less clear though it does vary greatly with σ for both realizations $\mathbf{D}_{ij}(\sigma)$ ($\log(\text{SE}(\hat{\lambda})/\hat{\lambda})$ is plotted in Figure 4.23(b)) and realizations of $\mathbf{D}_{ij}^{\text{rand}}(\sigma)$ ($\log(\text{SE}(\hat{\lambda})/\hat{\lambda})$ is plotted in Figure 4.23(d)).
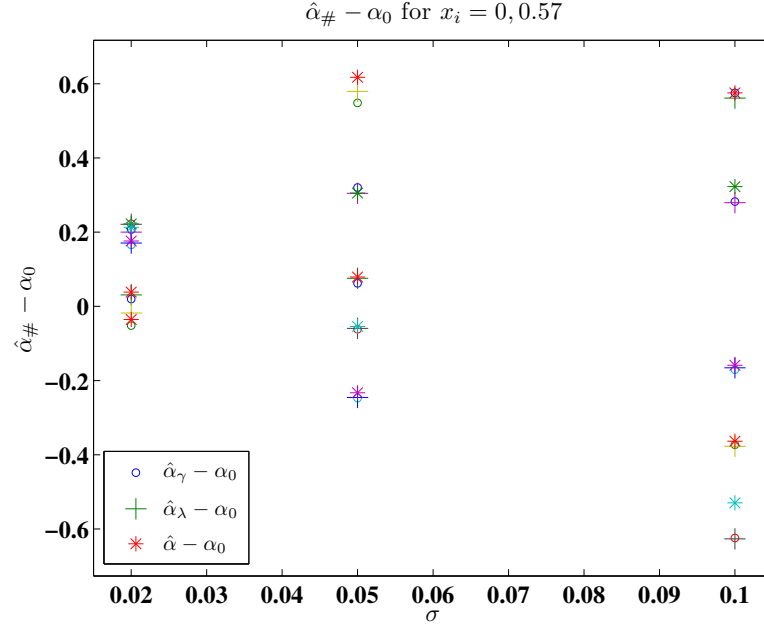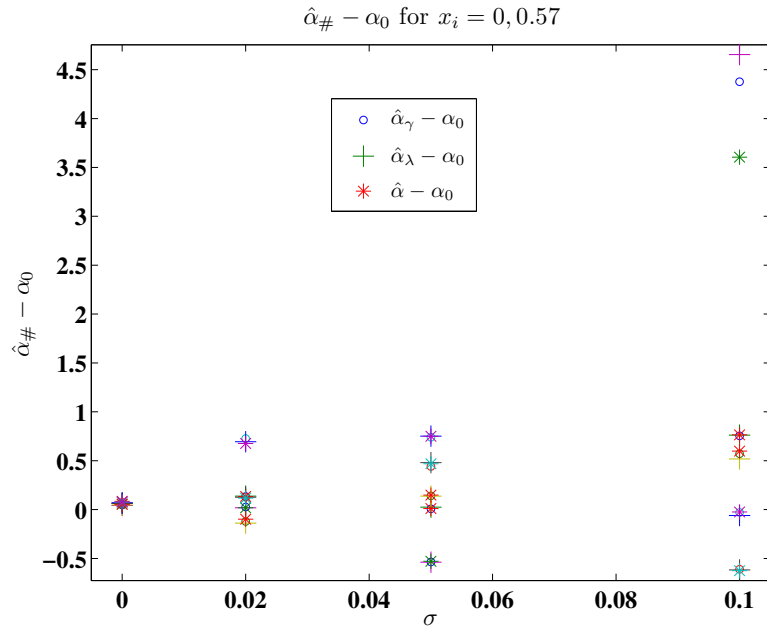
Figure 4.20: The results of realizations of simulated data with temporal nodes $t_j = 0.6 + \dfrac{1}{120}, 0.6 + \dfrac{2}{120}, \ldots, \dfrac{7}{120}, 20, 40, \ldots, 140$ and spatial nodes $x_i = 0, 0.57$. The points denoted with ^{o} are the difference $\hat{\alpha}_\gamma - \alpha_0$, the points denoted are the $\hat{\alpha}_\lambda - \alpha_0$, the points denoted * are the difference $\hat{\alpha} - \alpha_0$ (a) The result of five realizations of $\mathbf{D}_{ij}(\sigma)$ for values of $\sigma = 0.02, 0.05, 0.10$ (b) The result of five realizations of $\mathbf{D}_{ij}^{\text{rand}}(\sigma)$ for values of $\sigma = 0, 0.02, 0.05, 0.10$.

79
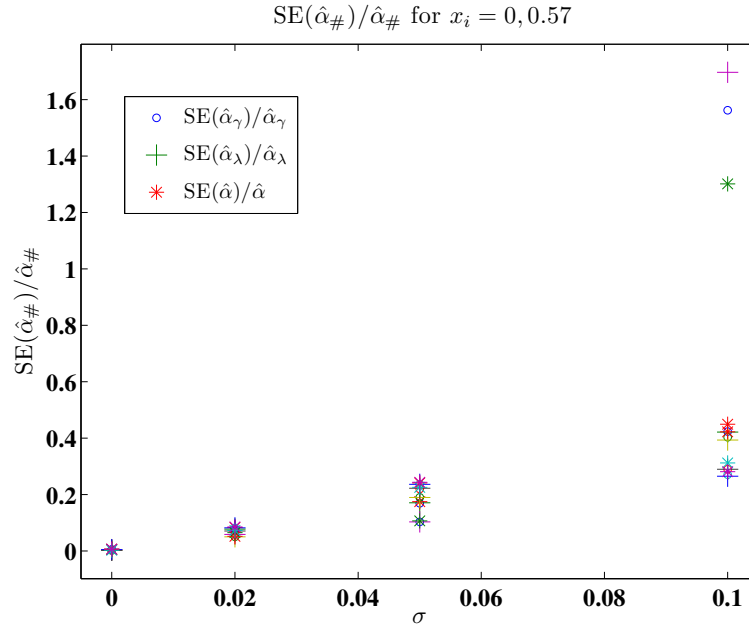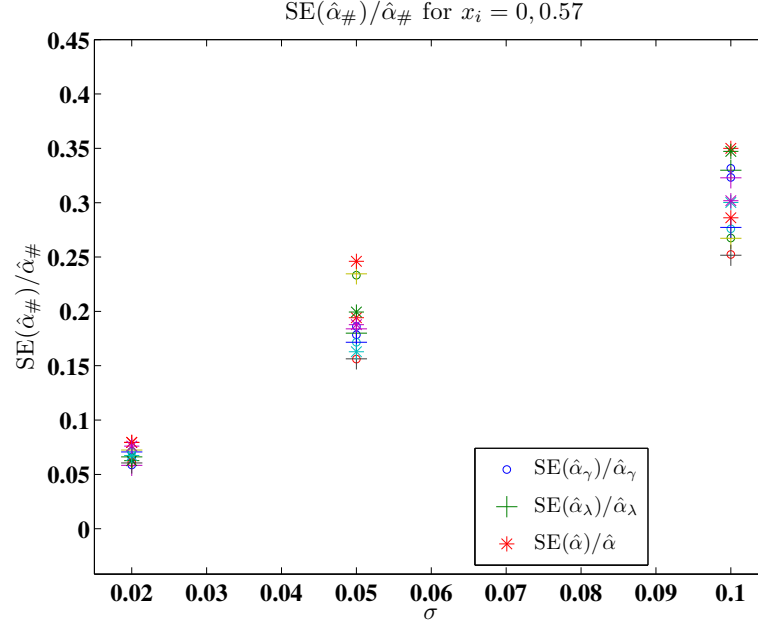
Figure 4.21: The results of realizations of simulated data with temporal nodes $t_j = 0.6 + \dfrac{1}{120}, 0.6 + \dfrac{2}{120}, \dots, \dfrac{7}{120}, 20, 40, \dots, 140$ and spatial nodes $x_i = 0, 0.57$. The points denoted with ^{o} are the ratio $\mathrm{SE}(\hat{\alpha}_\gamma)/\hat{\alpha}_\gamma$, the points denoted are the $\mathrm{SE}(\hat{\alpha}_\lambda)/\hat{\alpha}_\lambda$, the points denoted * are the difference $\mathrm{SE}(\hat{\alpha})/\hat{\alpha}$ (a) The result of five realizations of $\mathbf{D}_{ij}(\sigma)$ for values of $\sigma = 0.02, 0.05, 0.10$ (b) The result of five realizations of $\mathbf{D}_{ij}^{\mathrm{rand}}(\sigma)$ for values of $\sigma = 0, 0.02, 0.05, 0.10$.
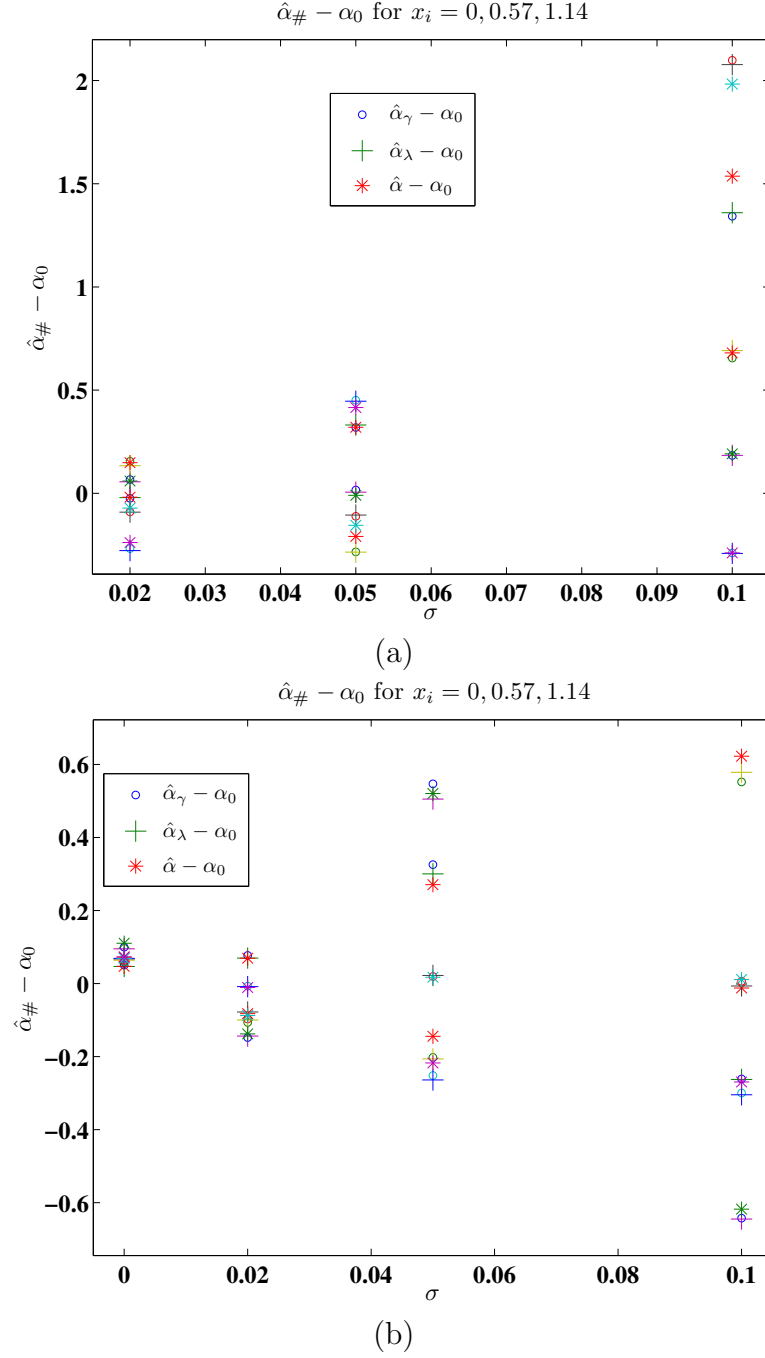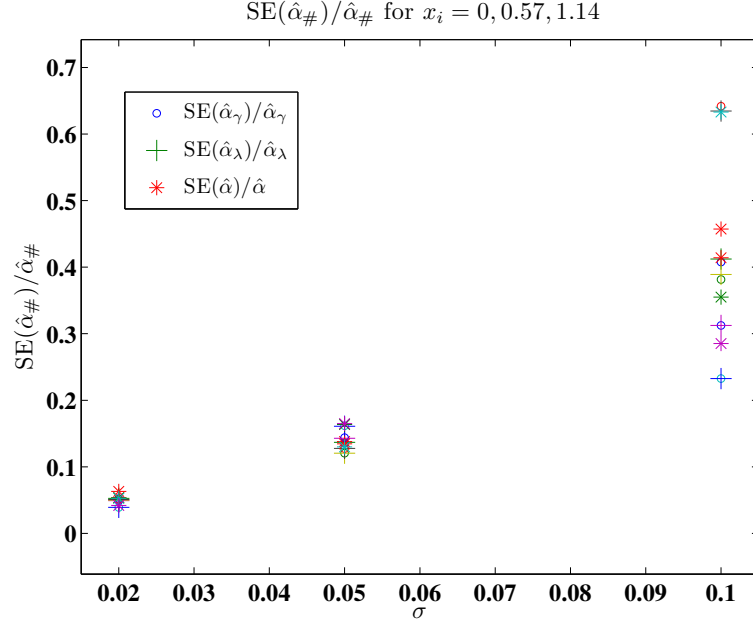
Figure 4.22: The results of realizations of simulated data with temporal nodes $t_j = 0.6 + \dfrac{1}{120}, 0.6 + \dfrac{2}{120}, \ldots, \dfrac{7}{120}, 20, 40, \ldots, 140$ and spatial nodes $x_i = 0, 0.57$. The points denoted with ^{o} are the difference $\hat{\lambda}_\gamma - \lambda_0$, and the points denoted * are the difference $\hat{\lambda} - \lambda_0$ (a) The result of five realizations of $\mathbf{D}_{ij}(\sigma)$ for values of $\sigma = 0.02, 0.05, 0.10$ (b) The result of five realizations of $\mathbf{D}_{ij}^{\text{rand}}(\sigma)$ for values of $\sigma = 0, 0.02, 0.05, 0.10$.
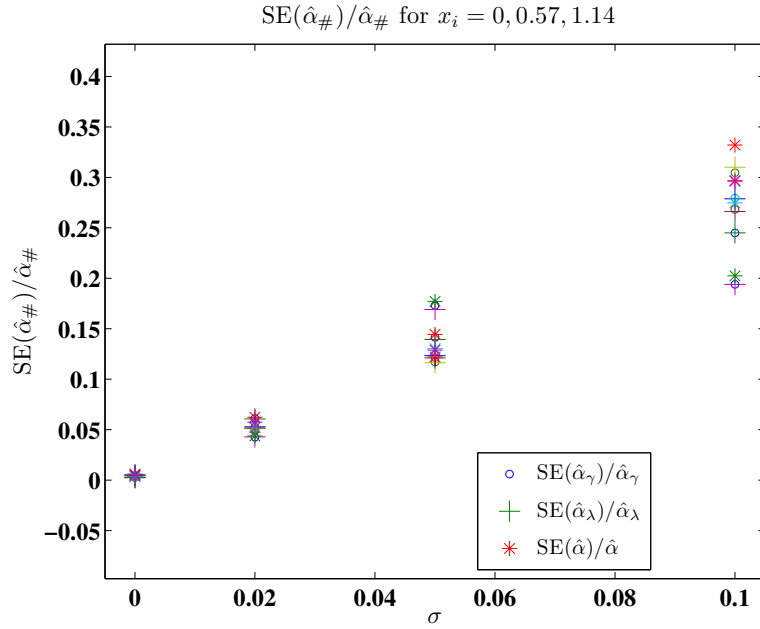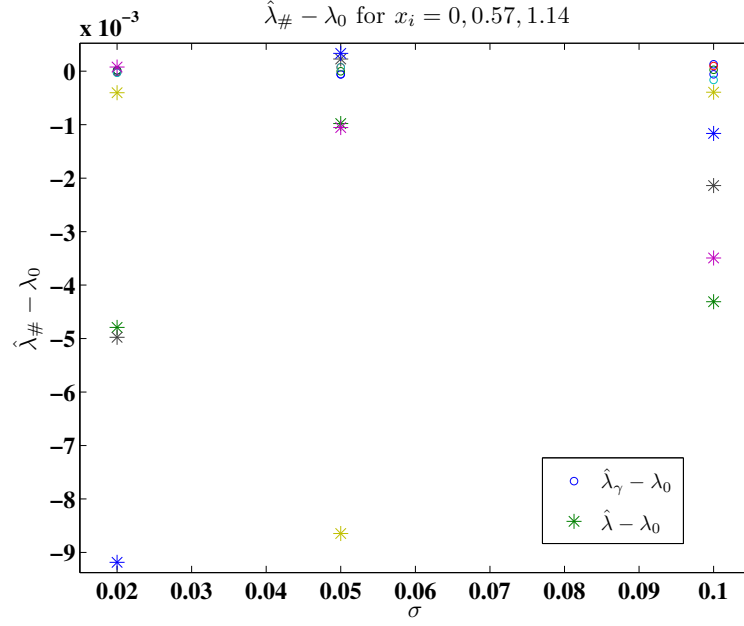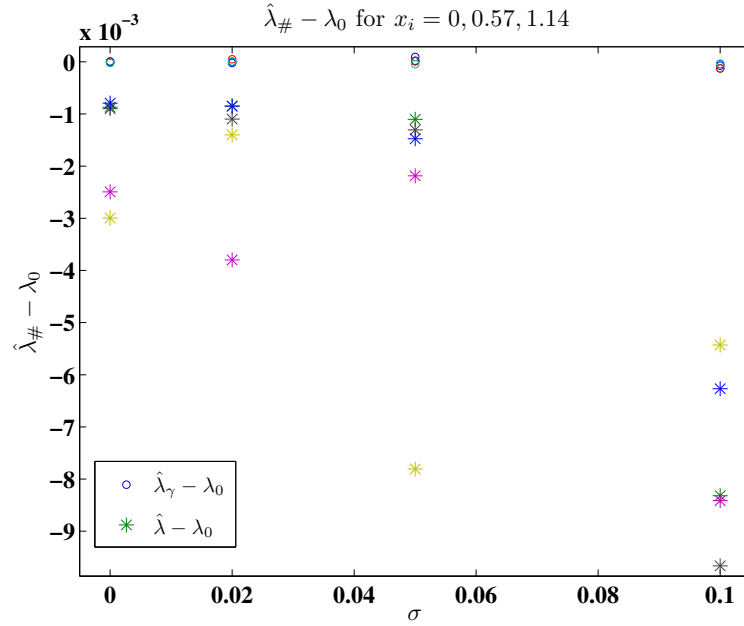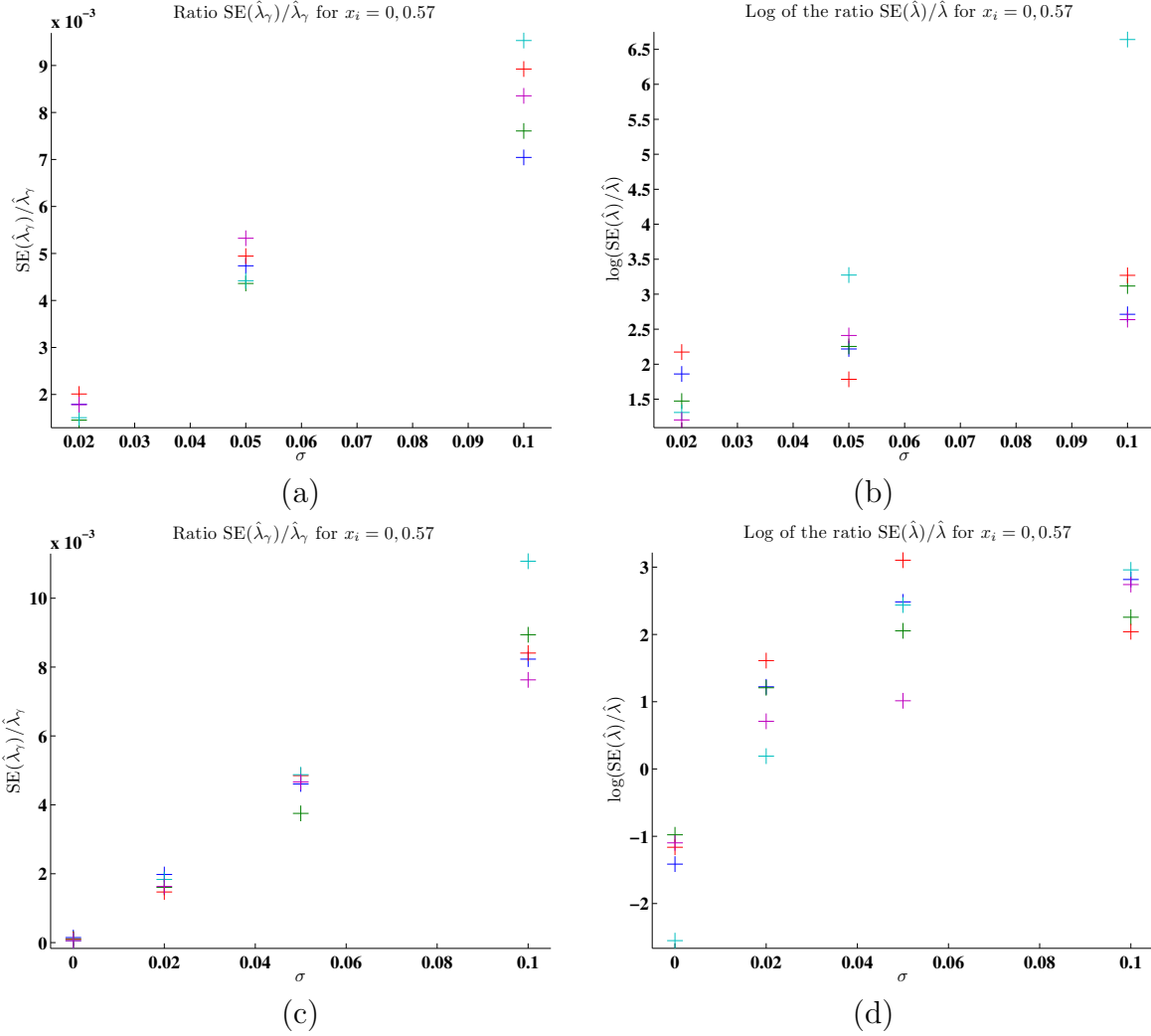
Figure 4.23: The results of realizations of simulated data with temporal nodes $t_j = 0.6 + \dfrac{1}{120}, 0.6 + \dfrac{2}{120}, \ldots, \dfrac{7}{120}, 20, 40, \ldots, 140$ and spatial nodes $x_i = 0, 0.57$. (a) The ratio $\mathrm{SE}(\hat{\lambda}_\gamma)/\hat{\lambda}_\gamma$ for five realizations of $\mathbf{D}_{ij}(\sigma)$ for values of $\sigma = 0.02, 0.05, 0.10$ (b) The log of the ratio $\log \mathrm{SE}(\hat{\lambda})/\hat{\lambda}$ for five realizations of $\mathbf{D}_{ij}(\sigma)$ for values of $\sigma = 0.02, 0.05, 0.10$. (c) The ratio $\mathrm{SE}(\hat{\lambda}_\gamma)/\hat{\lambda}_\gamma$ for five realizations of $\mathbf{D}_{ij}^{\mathrm{rand}}(\sigma)$ for values of $\sigma = 0, 0.02, 0.05, 0.10$. (d) The log of the ratio $\log \mathrm{SE}(\hat{\lambda})/\hat{\lambda}$ for five realizations of $\mathbf{D}_{ij}^{\mathrm{rand}}(\sigma)$ for values of $\sigma = 0, 0.02, 0.05, 0.10$.

The differences $\hat{\gamma}_\# - \gamma_0$ are plotted for realizations of $\mathbf{D}_{ij}(\sigma)$ and $\mathbf{D}_{ij}^{\text{rand}}(\sigma)$ in Figures 4.24(a) and (b), respectively. In both figures, the values $|\hat{\gamma} - \gamma_0|$ are much larger than the values $|\hat{\gamma}_\lambda - \gamma_0|$. This demonstrates that in these cases, estimating the full parameter set $\hat{\theta}$ contributes to inaccuracy of the paramter estimate of γ. Also, the differences $|\hat{\gamma} - \gamma_0|$ are several orders of magnitude larger than the "true" parameter value $\gamma_0 = 10^{-3}$. The values of the ratios $\text{SE}(\hat{\gamma}_\#)/\hat{\gamma}_\#$ vary a lot with σ in Figures 4.25(a)–(d). Figure 4.25(a) depicts $\log(\text{SE}(\hat{\gamma}_\lambda)/\hat{\gamma}_\lambda)$ for realizations of $\mathbf{D}_{ij}(\sigma)$ while $\mathbf{D}_{ij}^{\text{rand}}(\sigma)$ depicts $\log(\text{SE}(\hat{\gamma}_\lambda)/\hat{\gamma}_\lambda)$ for realizations of $\mathbf{D}_{ij}^{\text{rand}}(\sigma)$. In both Figure 4.25(a) and Figure 4.25(c), the ratio $\text{SE}(\hat{\gamma}_\lambda)/\hat{\gamma}_\lambda$ appears to depend exponentially on σ, though the value of $\text{SE}(\hat{\gamma}_\lambda)/\hat{\gamma}_\lambda$ remains below one for realizations that we considered. In Figures 4.25(b) and (d), we see that $\log(\text{SE}(\hat{\gamma})/\hat{\gamma})$ varies between 1–5 for realizations of $\mathbf{D}_{ij}(\sigma)$ (in (b)) and between -2–8 for realizations of $\mathbf{D}_{ij}^{\text{rand}}(\sigma)$ (in (d)).
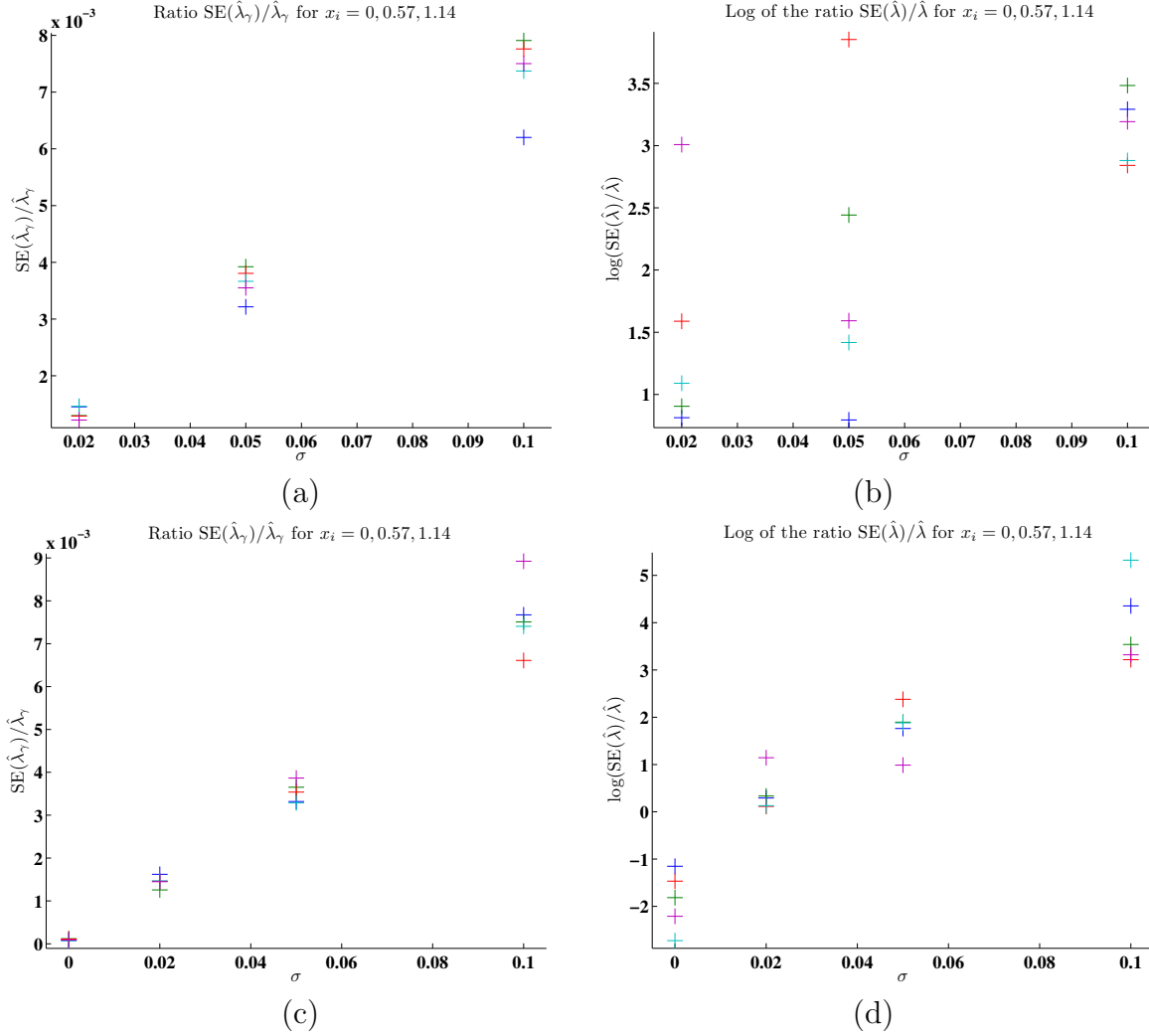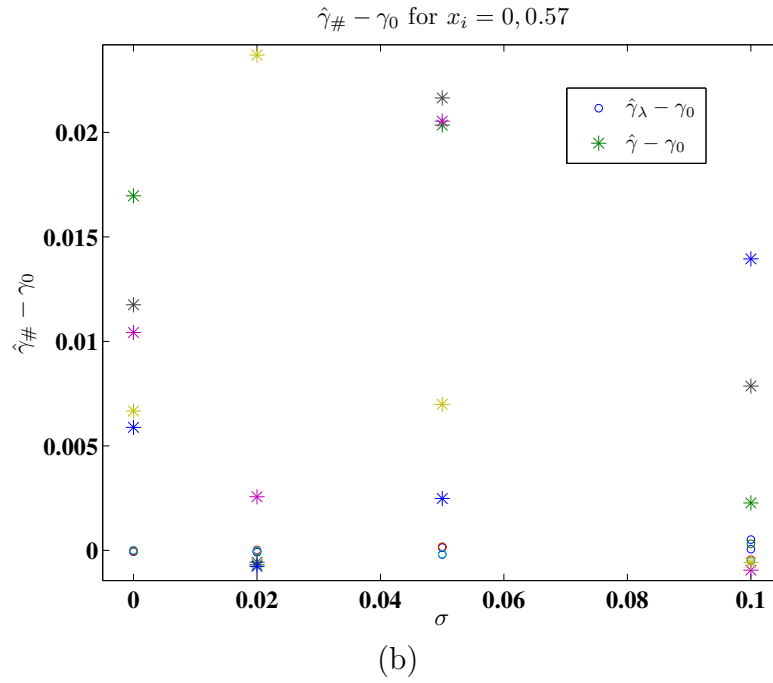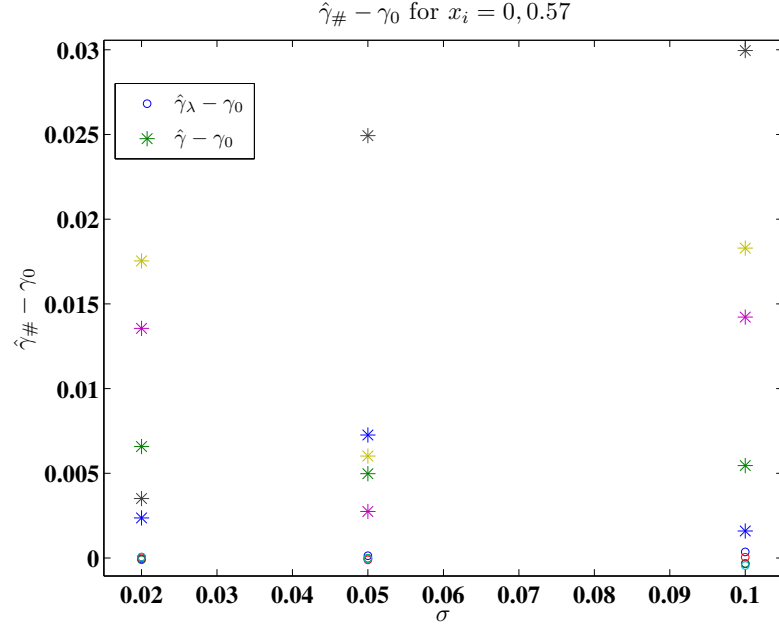
Figure 4.24: The results of realizations of simulated data with temporal nodes $t_j = 0.6 + \dfrac{1}{120}, 0.6 + \dfrac{2}{120}, \dots, \dfrac{7}{120}, 20, 40, \dots, 140$ and spatial nodes $x_i = 0, 0.57$. The points denoted with $^\circ$ are the difference $\hat{\gamma}_\lambda - \gamma_0$, and the points denoted * are the difference $\hat{\gamma} - \gamma_0$ (a) The result of five realizations of $\mathbf{D}_{ij}(\sigma)$ for values of $\sigma = 0.02, 0.05, 0.10$ (b) The result of five realizations of $\mathbf{D}_{ij}^{\mathrm{rand}}(\sigma)$ for values of $\sigma = 0, 0.02, 0.05, 0.10$.

84
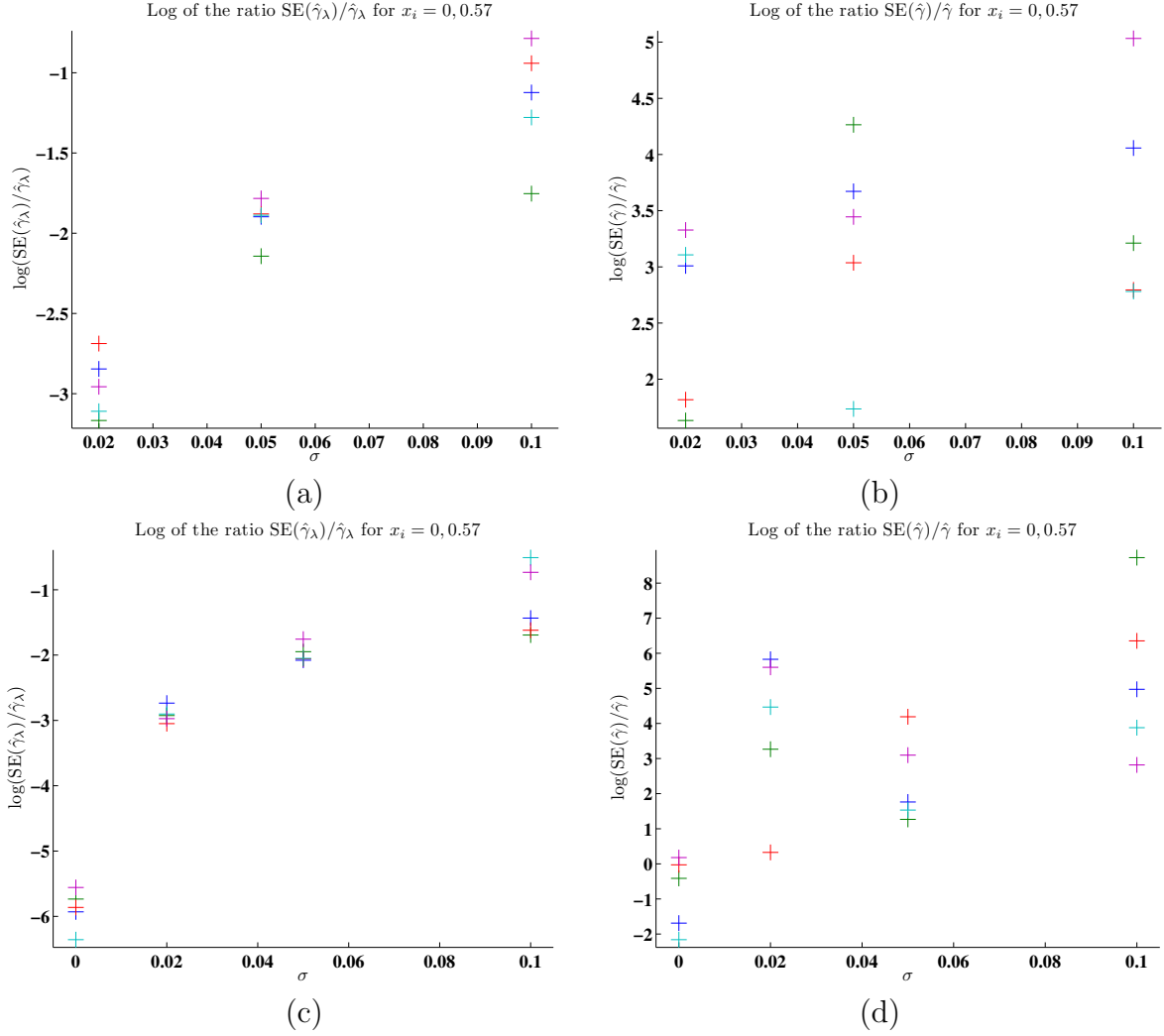
Figure 4.25: The results of realizations of simulated data with temporal nodes $t_j = 0.6 + \dfrac{1}{120}, 0.6 + \dfrac{2}{120}, \ldots, \dfrac{7}{120}, 20, 40, \ldots, 140$ and spatial nodes $x_i = 0, 0.57$. (a) The ratio $\mathrm{SE}(\hat{\gamma}_\lambda)/\hat{\gamma}_\lambda$ for five realizations of $\mathbf{D}_{ij}(\sigma)$ for values of $\sigma = 0.02, 0.05, 0.10$ (b) The log of the ratio $\log \mathrm{SE}(\hat{\gamma})/\hat{\gamma}$ for five realizations of $\mathbf{D}_{ij}(\sigma)$ for values of $\sigma = 0.02, 0.05, 0.10$. (c) The log of the ratio $\log(\mathrm{SE}(\hat{\gamma}_\lambda)/\hat{\gamma}_\lambda)$ for five realizations of $\mathbf{D}_{ij}^{\mathrm{rand}}(\sigma)$ for values of $\sigma = 0, 0.02, 0.05, 0.10$. (d) The log of the ratio $\log \mathrm{SE}(\hat{\gamma})/\hat{\gamma}$ for five realizations of $\mathbf{D}_{ij}^{\mathrm{rand}}(\sigma)$ for values of $\sigma = 0, 0.02, 0.05, 0.10$.

Chapter 5

Damage Detection and Characterization

5.1   Mathematical models

In order to discuss our method of detecting damage and results, we must discuss a few underlying models. First, we will discuss the models that we will use to simulate data. We developed a method for modeling the flash heat experiment on both damaged and undamaged porous domains in Chapter 2 which we use to simulate data in this chapter. We model the undamaged domain by the randomly perforated domain Ω. The homogeneous, non perforated domain is given by $\hat{\Omega}$ which is an $L_1 \times L_2$ rectangle (here we will use $L_1 = 10$ and $L_2 = 2$). The n_r randomly placed pores, which are generated using methods described in Chapter 2, are again denoted Ω_i with boundaries $\partial\Omega_i$ for $i = 1, 2 \ldots n_r$. The undamaged perforated domain Ω is given by $\hat{\Omega} \setminus (\cup_{i=1}^{n_r}\Omega_i)$. We will call the damaged porous domain $\Omega^D(q)$. The damage will be given by the ellipse $E^D(q) = \{(x,y) : \left(\frac{x - x_D}{h_D}\right)^2 + \left(\frac{y - y_D}{v_D}\right)^2 < 1\}$ with center (x_D, y_D), h_D is the horizontal semi-

axis and v_D is the vertical semi-axis. The ellipse and damaged domain are parameterized by q which specifies (x_D, y_D, h_D, v_D) though throughout this chapter we will consider y_D to be fixed. We restrict q so that the center of $E^D(q)$ is above the back boundary ω_2, and $E^D(q)$ intersects the boundary of $\hat{\Omega}$ at two points on ω_2. The damaged geometry is then given by $\Omega^D(q) = \Omega \setminus \left(E^D(q) \cup \mathcal{O}(q) \right)$ where $\mathcal{O}(q)$ is the set of ellipses in Ω that intersect $E^D(q)$. An example damaged domain is depicted in Figure 5.1. We model the heat equation on this domain with

$$
\begin{cases}
\dfrac{\partial}{\partial t} u_D^{\text{rand}} - \alpha \nabla \cdot \left(\nabla u_D^{\text{rand}} \right) = 0 & \text{in } \Omega^D \times (0, T) \\[2mm]
\alpha \dfrac{\partial}{\partial \eta} u_D^{\text{rand}} = 0 & \text{on } \left(\cup_{i=1}^{n_r^D} \partial \Omega_i \right) \times (0, T) \\[2mm]
\alpha \dfrac{\partial}{\partial \eta} u_D^{\text{rand}} = 0 & \text{on } \left(\omega_1 \cup \omega_2^D \cup \omega_3 \right) \times (0, T) \\[2mm]
\alpha \dfrac{\partial}{\partial \eta} u_D^{\text{rand}} = S_f \mathcal{I}_{[0, t_s]}(t) & \text{on } \omega_4 \times (0, T) \\[2mm]
u^{\text{rand}}(0, \vec{x}) = 0,
\end{cases}
\tag{5.1}
$$

where the $\partial \Omega_i$ for $i = 1, 2, \ldots n_r^D$ are the boundaries of the n_r^D pores remaining in $\Omega^D(q)$. The back boundary of $\Omega^D(q)$, $\omega_2^D(q)$ is parametrized by (x_D, y_D, h_D, v_D). In order to define $\omega_2^D(q)$ more precisely, we introduce the piecewise defined function

$$
r(x; q) =
\begin{cases}
L_2 & \text{for } 0 \leq x \leq x_L(q) \\[2mm]
y_D - v_D \sqrt{1 - \left(\dfrac{x - x_D}{h_D} \right)^2} & \text{for } x_L(q) < x < x_R(q) \\[2mm]
L_2 & \text{for } x_R(q) \leq x \leq L_1,
\end{cases}
\tag{5.2}
$$
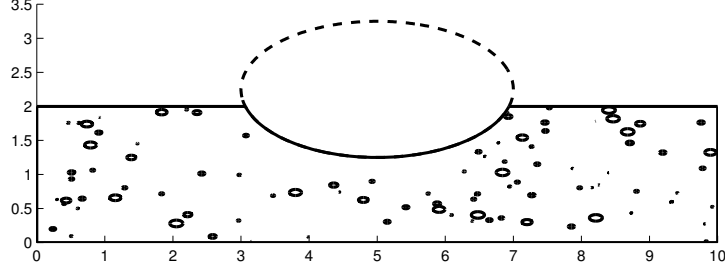
Figure 5.1: An example geometry $\Omega^D(q)$ for $(x_D, y_D, h_D, v_D) = (5, 2.25, 2, 1)$

where the left end point $x_L(q)$ is given by $x_L(q) = x_D - h_D\sqrt{1 - \left(\dfrac{y_D - L_2}{v_D}\right)^2}$ and the

right end point is given by $x_R(q) = x_D + h_D\sqrt{1 - \left(\dfrac{y_D - L_2}{v_D}\right)^2}$. The damaged back

boundary of $\Omega^D(q)$ is then given by $\omega_2^D(q) = \{(x, y) : 0 \le x \le L_1 \text{ and } y = r(x; q)\}$.

We simulate data using the same model of the output of an IR camera as in Sections 4.2.1 and 4.3.1. We again use pixel length $\ell = 0.57$ and take the simulated data on the source boundary ω_4. We denote

$$\left(u_D^{\text{rand}}(q)\right)_{ij} = \frac{1}{\ell} \int_{x_i}^{x_i+\ell} u_D^{\text{rand}}(t_j, s, 0; q)\, ds. \tag{5.3}$$

To include error associated with the measurement process, we will take data given by realizations of

$$\mathbf{D}_{ij}^{\text{rand}}(q) = \left(u_D^{\text{rand}}(q)\right)_{ij} + \sigma\boldsymbol{\beta}_{ij}, \tag{5.4}$$

where the $\boldsymbol{\beta}_{ij}$ are independently identically distributed standard normal random variables. That is $\boldsymbol{\beta}_{ij} \sim \mathcal{N}(0, 1^2)$. In this chapter, we focus on $\sigma = 0.015$. It is important to emphasize that $\mathbf{D}_{ij}^{\text{rand}}(q)$ is a random variable with realizations $\mathrm{D}_{ij}^{\text{rand}}(q)$. The realization $\mathrm{D}_{ij}^{\text{rand}}(q)$ would correspond to observed data. We again take m spatial nodes (which corre-

spond to pixels) which correspond to the $\{x_i\}$'s and n temporal nodes which correspond to the $\{t_j\}$'s in (5.4).

We will again use a model motivated by homogenization theory as the model solution in our inverse problems. We will also simulate data from this model as in Chapter 4 to understand the effect of the error associated with the approximation derived from homogenization theory affects the inverse problem. Methods used in Chapters 3 and 4 and [13, 17, 20, 16, 15, 23, 19, 2, 18] can be used to establish the convergence of $u_D^{\text{rand}}(t, \vec{x}; q)$ to $u^D(t, \vec{x}; q)$ where $u^D(t, \vec{x}; q)$ is given by

$$
\begin{cases}
p_V \dfrac{\partial}{\partial t} u^D - \alpha \nabla \cdot (A^0 \nabla u^D) = 0 & \text{in } \mathcal{T} \times \hat{\Omega}^D(q) \\[2mm]
\alpha \dfrac{\partial}{\partial \eta_{A^0}} u^D = 0 & \text{on } \mathcal{T} \times (\omega_1 \cup \omega_2(q) \cup \omega_3) \\[2mm]
\alpha \dfrac{\partial}{\partial \eta_{A^0}} u^D = S_f \mathcal{I}_{[0,t_s]}(t) & \text{on } \mathcal{T} \times \omega_4 \\[2mm]
u^D(0, \vec{x}) = 0 & \text{for } \vec{x} \in \hat{\Omega}^D,
\end{cases}
\tag{5.5}
$$

where again α is the thermal diffusivity, p_V is the proportion of the material in the porous domain (here, $p_V = 0.98$), A^0 is the anisotropy matrix associated with the results of homogenization theory from Chapter 3, S_f is the intensity of the heat lamp and $\mathcal{I}_{[0,t_s]}(t)$ is the heaviside function. The geometry on which the partial differential equation (5.5) is defined is given by $\hat{\Omega}^D(q) = \hat{\Omega} \setminus E^D(q)$.

The weak solution of (5.5) is given by

$$
p_V \int_{\hat{\Omega}^D(q)} \frac{\partial}{\partial t} u^D(t, \vec{x}; q) \phi(\vec{x}) \, d\vec{x} \;\; + \;\; \alpha \int_{\hat{\Omega}^D(q)} \nabla u^D(t, \vec{x}; q) \cdot A^0 \nabla \phi(\vec{x}) \, d\vec{x}
$$
$$
= \;\; S_f \mathcal{I}_{[0,t_s]}(t) \int_{\omega_4} \gamma_{\omega_4}(\phi(\vec{x})) \, d\xi_{\omega_4},
\tag{5.6}
$$

for all test functions $\phi \in H^1(\hat{\Omega}^D)$ where γ_{ω_4} is the trace on ω_4 and ξ_{ω_4} is a parametrization of ω_4. In order to compute a finite element solution of (5.6), for each iteration of q, a new mesh of $\hat{\Omega}^D(q)$ must be generated. In order to avoid this difficulty, we make the coordinate transformation $\vec{x} = T(q) \circ \vec{z}$ where $T(q)$ is the bijection that maps $\hat{\Omega}$ to $\hat{\Omega}^D(q)$ given by

$$\vec{z} = \begin{bmatrix} z_1 \\ z_2 \end{bmatrix} = T(q)(\vec{x}) = \begin{bmatrix} x \\ \dfrac{r(x;q)}{L_2}y \end{bmatrix}. \tag{5.7}$$

The weak formulation (5.6) can be written as

$$p_V \int_{\hat{\Omega}} \frac{\partial}{\partial t} u(t,\vec{x};q)\phi(\vec{x}) \det\left(\nabla T(\vec{x};q)\right) d\vec{x}$$

$$-\alpha \int_{\hat{\Omega}} \nabla u(t,\vec{x};q) \cdot \nabla T(\vec{x};q)^{-1} A^0 \left(\nabla T(\vec{x};q)^{\dagger}\right)^{-1} \nabla\phi(\vec{x}) \det(\nabla T(\vec{x};q)) d\vec{x} \tag{5.8}$$

$$= S_f \mathcal{I}_{[0,t_s]}(t) \int_{\hat{\omega}_4} \gamma_{\omega_4}(\phi) d\xi_{\omega_4}, \text{ for all } \phi(\vec{x}) \in H^1(\hat{\Omega}),$$

by making the coordinate transformation $\vec{z} = T(\vec{x};q)$ where † is the transpose. Noting that

$$\nabla T(\vec{x};q) = \begin{bmatrix} 1 & 0 \\ \dfrac{r'(x;q)}{L_2}y & \dfrac{r(x;q)}{L_2} \end{bmatrix}, \tag{5.9}$$

and $\det(\nabla T(\vec{x};q)) = \dfrac{r(x;q)}{L_2}$, we may rewrite (5.8) as

$$\frac{p_V}{L_2} \int_{\hat{\Omega}} \frac{\partial}{\partial t} u(t, \vec{x}; q) \phi(\vec{x}) r(x; q) \, d\vec{x} \quad - \quad \alpha \int_{\hat{\Omega}} \nabla u(t, \vec{x}; q) \cdot B(\vec{x}; q) \nabla \phi(\vec{x}) \, d\vec{x}$$

$$(5.10)$$

$$= \quad S_f \mathcal{I}_{[0,t_s]}(t) \int_{\omega_4} \gamma_{\omega_4}(\phi) \, d\xi_{\omega_4}.$$

In (5.10), above $B(\vec{x}; q)$ is a 2×2 matrix with entries

$$
\begin{aligned}
b_{11}(\vec{x}; q) &= a_{11}^0 \frac{r(x; q)}{L_2} \\
b_{12}(\vec{x}; q) &= -a_{11}^0 \, y \, \frac{r'(x; q)}{L_2} + a_{12}^0 \\
b_{21}(\vec{x}; q) &= -a_{11}^0 \, y \, \frac{r'(x; q)}{L_2} + a_{21}^0 \\
b_{22}(\vec{x}; q) &= a_{11}^0 \, y^2 \frac{(r'(x; q))^2}{r(x; q) L_2} - \frac{r'(x; q)}{r(x; q)} y(a_{12}^0 + a_{21}^0) + a_{22}^0 \frac{L_2}{r(x; q)},
\end{aligned}
$$

$$(5.11)$$

where a_{ij}^0 are the entries of A^0. Using the finite element approximation $\tilde{u}^N(t, \vec{x}; q) = \sum_{j=1}^{N} u_j(t; q) \phi_j(\vec{x})$ where $\phi_j(\vec{x})$ is a piecewise affine two dimensional basis element, we may solve for the time dependent coefficients by solving the ordinary differential equation

$$p_V C(q) \frac{d}{dt} \vec{u}(t) + \alpha K(q) \vec{u}(t) = S_f \mathcal{I}_{[0,t_s]}(t) \vec{f},$$

$$(5.12)$$

where

$$
\begin{aligned}
C_{ij}(q) &= \frac{1}{L_2} \int_{\hat{\Omega}} \phi_j(\vec{x}) \phi_i(\vec{x}) r(x; q) \, d\vec{x} && \text{for } i, j = 1, 2, \ldots N \\
K_{ij}(q) &= \int_{\Omega} \nabla \phi_j(\vec{x}) \cdot B(\vec{x}; q) \nabla \phi_i(\vec{x}) \, d\vec{x} && \text{for } i, j = 1, 2, \ldots N \\
\vec{f}_i &= \int_{\omega_4} \gamma_{\omega_4}(\phi_i) \, d\xi_{\omega_4} && \text{for } i = 1, 2, \ldots N \\
\vec{u}_i(t) &= u_i(t) && \text{for } i = 1, 2, \ldots N.
\end{aligned}
$$

$$(5.13)$$

As in formulating $(u_D^{\mathrm{rand}}(q))_{ij}$ in (5.3), we use the average of the solution over intervals

of length ℓ (which represents the pixel length) in our model solution. We will use model solutions given by

$$U_{ij}(q) = \frac{1}{\ell} \int_{x_i}^{x_i+\ell} \tilde{u}^N(t_j, x, 0; q) \, dx \qquad (5.14)$$

where $\tilde{u}^N(t, \vec{x}; q)$ is the finite element solution of (5.12).

We will use $U_{ij}(q)$ as defined in (5.14) as a model solution in our data analyses. In all of our data analysis, we make the assumption that data are given by realizations of the random process $\boldsymbol{y}_{ij}$ which is defined as

$$\boldsymbol{y}_{ij} = U_{ij}(q_0) + \boldsymbol{\epsilon}_{ij}, \qquad (5.15)$$

where $\boldsymbol{\epsilon}_{ij}$ is a random variable that satisfies (5.16) below and q_0 is the "true" parameter value. The random variable (random error) $\boldsymbol{\epsilon}_{ij}$ is further assumed to have zero mean, be independent and have constant variance. More precisely, we assume

$$
\begin{aligned}
E(\boldsymbol{\epsilon}_{ij}) &= 0 \\
\mathrm{Var}(\boldsymbol{\epsilon}_{ij}) &= \sigma_0^2 \\
\mathrm{Cov}(\boldsymbol{\epsilon}_{ij}, \boldsymbol{\epsilon}_{kh}) &= 0 \text{ for } (i,j) \neq (k,h).
\end{aligned}
\qquad (5.16)
$$

As in Chapter 4, to check these assumption for $\mathbf{D}_{ij}^{\mathrm{rand}}$, we will also consider data generated using the finite element solution (5.12). Specifically, we will consider data generated using

$$\mathbf{D}_{ij}(q) = U_{ij}(q) + \sigma \boldsymbol{\beta}_{ij}, \qquad (5.17)$$

where as in (5.4), $\boldsymbol{\beta}_{ij} \sim \mathcal{N}(0, 1^2)$. The realizations of the random variable $\mathbf{D}_{ij}(q)$ are denoted $\mathrm{D}_{ij}(q)$.

We will consider two kinds of statistical procedures. We will consider a data compar-

ison technique to detect damage through a hypothesis test which is developed in [9]. We will then use ordinary least squares parameter estimation (as in Chapter 4) to estimate the parameter set (x_D, h_D, v_D).

5.2 Damage Detection

Both the hypothesis test methodology and OLS parameter estimation involve minimizing the ordinary least squares cost functional, which we recall from Section 4.2

$$J(q) = \sum_{i=1}^{m} \sum_{j=1}^{n} \left(U_{ij}(q) - \text{data}_{ij} \right)^2. \tag{5.18}$$

The term data_{ij} represents either of the realizations D_{ij} or $\text{D}_{ij}^{\text{rand}}$. Again, we emphasize that the function of the realization $J(q)$ is a realization of a function of a random variable

$$\mathbf{J}(q) = \sum_{i=1}^{m} \sum_{j=1}^{n} \left(U_{ij}(q) - \mathbf{data}_{ij} \right)^2. \tag{5.19}$$

where $\mathbf{data}_{ij}$ represents either the random process $\mathbf{D}_{ij}$ or the random process $\mathbf{D}_{ij}^{\text{rand}}$.

Damage detection may be considered using a hypothesis test. The case where there is no damage can be modeled with an ellipse E^D with a horizontal semi-axis length of zero. So when $h_D = 0$, we have that there is no damage in the sample.

We will formulate a hypothesis test using these two cases as our hypotheses. The null hypothesis (there is no damage) is given by $H_0 : h_D = 0$, and the alternative hypothesis (there is damage) is given by $H_A : h_D \neq 0$. We will call the set of parameters corresponding to the null hypothesis $\mathcal{Q}_H = \{q : h_D = 0, q \in \mathcal{Q}\}$. We will consider the full parameter set $q = (x_D, h_D, v_D, \alpha)$. Using methods described and developed in [7, 9],

we consider two parameter estimates

$$\hat{q} = \arg\min_{q \in \mathcal{Q}_H} J(q), \tag{5.20}$$

and

$$\tilde{q} = \arg\min_{q \in \mathcal{Q}} J(q), \tag{5.21}$$

where the parameter estimates are realizations of random variables. The two estimators are given by

$$\hat{\mathbf{q}} = \arg\min_{q \in \mathcal{Q}_H} \mathbf{J}(q), \tag{5.22}$$

and

$$\tilde{\mathbf{q}} = \arg\min_{q \in \mathcal{Q}} \mathbf{J}(q), \tag{5.23}$$

respectively. The estimates are realizations of the random estimators.

This model comparison methodology uses the test statistic $\boldsymbol{X}$ given by

$$\boldsymbol{X} = nm \left(\frac{\boldsymbol{J}(\hat{\boldsymbol{q}}) - \boldsymbol{J}(\tilde{\boldsymbol{q}})}{\boldsymbol{J}(\tilde{\boldsymbol{q}})} \right) \tag{5.24}$$

where nm is the total number of observations (there are n temporal nodes and m spatial nodes). The random variable $\boldsymbol{X}$ then has realizations X which are given by

$$X = nm \left(\frac{J(\hat{q}) - J(\tilde{q})}{J(\tilde{q})} \right), \tag{5.25}$$

where $\hat{q}$ is the corresponding realization of $\hat{\boldsymbol{q}}$ and $\tilde{q}$ is the corresponding realization of $\tilde{\boldsymbol{q}}$.

The results of [9] indicate that if H_0 is true then the distribution of the random variable $\boldsymbol{X}$ approaches a chi-square distribution with one degree of freedom (denoted $\chi^2(1)$) as nm

94

Pixel Set	x_i values
Left 11 Nodes	$x_i = \ell(i-1)$ for $i \in \{1, 2, \ldots 11\}$
Right 11 Nodes	$x_i = \ell(i-1) + 6\ell$ for $i \in \{1, 2, \ldots 11\}$
Evenly Spaced 11 Nodes	$x_i \in \{0, 2\ell, 5\ell, 6\ell, 7\ell, 9\ell, 10\ell, 12\ell, 13\ell, 15\ell, 16\ell\}$
All 17 Nodes	$x_i = \ell(i-1)$, for $i \in \{1, 2, 3 \ldots, 17\}$

Table 5.1: Pixel sets used throughout this chapter with $\ell = 0.57$

goes to infinity. Suppose we would like to reject our null hypothesis with 95% confidence, we calculate the corresponding significance level $\alpha = 0.05$ (note that confidence $= (1 - \alpha) \times 100\%$) and the corresponding threshold value τ where the probability $P(\boldsymbol{X} > \tau) = \alpha$. Using a $\chi^2(1)$ cumulative distribution function table, for $\alpha = 0.05$, we find $\tau = 3.84$. Then for any realization X with $X > 3.84$, we may reject with at least 95% confidence. The minimum value α^* at which the null hypothesis can be rejected for a realization X is called the p-value, that is

$$\text{p-value} = \alpha^* = \min P(\boldsymbol{X} > X).$$

The closer a p-value is to zero, the more confidence with which one may reject the null hypothesis.

We considered simulations using four sets of spatial nodes (corresponding to pixels) which are listed in Table 5.1. We used these values to generate the data D_{ij} and D_{ij}^{rand}. We considered eight different damages. In each example we assumed $y_D = 2.25$ was considered to be known. We used damages $(x_D, h_D, v_D) = (3, 1, 0.5)$, $(x_D, h_D, v_D) = (5, 1, 0.5)$, $(x_D, h_D, v_D) = (3, 2, 1)$, $(x_D, h_D, v_D) = (5, 2, 1)$, $(x_D, h_D, v_D) = (3, 0.5, 1)$, $(x_D, h_D, v_D) = (5, 0.5, 1)$, $(x_D, h_D, v_D) = (3, 0.5, 1.5)$ and $(x_D, h_D, v_D) = (5, 0.5, 1.5)$. In Tables 5.2-5.9, we summarize the results of this model comparison technique data sets

Table 5.2: $(x_D, h_D, v_D) = (3, 1, 0.5)$

Nodes	$n \times m$	Data	$J(\tilde{q})$	$J(\hat{q})$	X
Left	1012	**D**	0.433	0.225	9.368×10^2
		$\mathbf{D}^{\text{rand}}$	0.407	0.241	7.018×10^2
Right	1012	**D**	0.305	0.217	4.093×10^2
		$\mathbf{D}^{\text{rand}}$	0.38	0.25	5.309×10^2
Even	1012	**D**	0.399	0.221	8.136×10^2
		$\mathbf{D}^{\text{rand}}$	0.394	0.251	5.802×10^2
All	1564	**D**	0.615	0.336	1.294×10^3
		$\mathbf{D}^{\text{rand}}$	0.604	0.379	9.255×10^2

simulated with (5.4) and (5.17) using spatial nodes given in Table 5.1 and temporal nodes given by $t_j = 0.6 + \dfrac{1}{120}j$ for $j \in \{1, 2, \ldots 92\}$.

The threshold value of the statistic τ at which one may reject the null hypothesis with 99.9% confidence is $\tau = 10.8$. If $X > 10.8$ one may reject the null hypothesis with 99.9% confidence. The larger X is the more confidence there is in rejecting the null hypothesis. The values of X that resulted for our calculations were very large, indicating that for the examples we considered, for both kinds of data, one may reject the null hypothesis of "no damage" with 100% confidence. For each example that we considered in Tables 5.2–5.9, the value of the statistic X is several orders of magnitude higher than 10.8. The value of X varies between 10^2 and 10^5 in the simulations that we carried out. This value was sometimes larger and sometimes smaller for realizations of $\mathbf{D}_{ij}^{\text{rand}}$ than for realizations of $\mathbf{D}_{ij}$ but there is no clear pattern. This was true for all of the pixel sets that we considered.

Table 5.3: $(x_D, h_D, v_D) = (3, 2, 1)$

Nodes	$n \times m$	Data	$J(\tilde{q})$	$J(\hat{q})$	X
Left	1012	$\mathbf{D}$	33.4	0.255	1.316×10^5
		$\mathbf{D}^{\text{rand}}$	15	0.351	4.238×10^4
Right	1012	$\mathbf{D}$	11.6	0.238	4.848×10^4
		$\mathbf{D}^{\text{rand}}$	9.3	0.357	2.532×10^4
Even	1012	$\mathbf{D}$	22.4	0.239	9.393×10^4
		$\mathbf{D}^{\text{rand}}$	17.1	0.496	3.38×10^4
All	1564	$\mathbf{D}$	33.6	0.368	1.412×10^5
		$\mathbf{D}^{\text{rand}}$	25.6	0.656	5.952×10^4

Table 5.4: $(x_D, h_D, v_D) = (5, 1, 0.5)$

Nodes	$n \times m$	Data	$J(\tilde{q})$	$J(\hat{q})$	X
Left	1012	$\mathbf{D}$	0.468	0.225	1.096×10^3
		$\mathbf{D}^{\text{rand}}$	0.535	0.259	1.082×10^3
Right	1012	$\mathbf{D}$	0.456	0.214	1.146×10^3
		$\mathbf{D}^{\text{rand}}$	0.589	0.25	1.378×10^3
Even	1012	$\mathbf{D}$	0.412	0.223	8.592×10^2
		$\mathbf{D}^{\text{rand}}$	0.495	0.254	9.596×10^2
All	1564	$\mathbf{D}$	0.604	0.334	1.259×10^3
		$\mathbf{D}^{\text{rand}}$	0.75	0.386	1.477×10^3

Table 5.5: $(x_D, h_D, v_D) = (5, 2, 1)$

Nodes	$n \times m$	Data	$J(\tilde{q})$	$J(\hat{q})$	X
Left	1012	$\mathbf{D}$	27.5	0.243	1.135×10^5
		$\mathbf{D}^{\text{rand}}$	19.9	0.297	6.682×10^4
Right	1012	$\mathbf{D}$	28.7	0.228	1.265×10^5
		$\mathbf{D}^{\text{rand}}$	21.6	0.293	7.369×10^4
Even	1012	$\mathbf{D}$	15.2	0.237	6.404×10^4
		$\mathbf{D}^{\text{rand}}$	16.1	0.335	4.769×10^4
All	1564	$\mathbf{D}$	32.1	0.369	1.344×10^5
		$\mathbf{D}^{\text{rand}}$	24.2	0.531	6.98×10^4

Table 5.6: $(x_D, h_D, v_D) = (3, 0.5, 1)$

Nodes	$n \times m$	Data	$J(\tilde{q})$	$J(\hat{q})$	X
Left	1012	**D**	1.1	0.224	3.967×10^3
		D$^{\text{rand}}$	0.86	0.24	2.619×10^3
Right	1012	**D**	0.535	0.226	1.387×10^3
		D$^{\text{rand}}$	0.682	0.256	1.683×10^3
Even	1012	**D**	0.827	0.228	2.666×10^3
		D$^{\text{rand}}$	0.874	0.247	2.567×10^3
All	1564	**D**	1.25	0.354	3.941×10^3
		D$^{\text{rand}}$	1.37	0.392	3.904×10^3

Table 5.7: $(x_D, h_D, v_D) = (3, 0.5, 1.5)$

Nodes	$n \times m$	Data	$J(\tilde{q})$	$J(\hat{q})$	X
Left	1012	**D**	2.34	0.234	9.109×10^3
		D$^{\text{rand}}$	2.68	0.309	7.773×10^3
Right	1012	**D**	1.24	0.226	4.542×10^3
		D$^{\text{rand}}$	1.88	0.292	5.515×10^3
Even	1012	**D**	2.31	0.228	9.231×10^3
		D$^{\text{rand}}$	2.37	0.305	6.867×10^3
All	1564	**D**	2.8	0.353	1.087×10^4
		D$^{\text{rand}}$	3.59	0.488	9.948×10^3

Table 5.8: $(x_D, h_D, v_D) = (5, 0.5, 1)$

Nodes	$n \times m$	Data	$J(\tilde{q})$	$J(\hat{q})$	X
Left	1012	**D**	0.724	0.229	2.193×10^3
		D$^{\text{rand}}$	1.2	0.298	3.051×10^3
Right	1012	**D**	0.883	0.227	2.917×10^3
		D$^{\text{rand}}$	1.34	0.263	4.138×10^3
Even	1012	**D**	0.756	0.232	2.28×10^3
		D$^{\text{rand}}$	1.03	0.262	2.949×10^3
All	1564	**D**	1.15	0.356	3.478×10^3
		D$^{\text{rand}}$	1.55	0.404	4.434×10^3

Table 5.9: $(x_D, h_D, v_D) = (5, 0.5, 1.5)$

Nodes	$n \times m$	Data	$J(\tilde{q})$	$J(\hat{q})$	X
Left	1012	**D**	2.41	0.222	9.957×10^3
		D$^{\text{rand}}$	3.15	0.427	6.449×10^3
Right	1012	**D**	1.92	0.229	7.479×10^3
		D$^{\text{rand}}$	3.12	0.526	4.991×10^3
Even	1012	**D**	1.63	0.226	6.273×10^3
		D$^{\text{rand}}$	3.6	0.361	9.061×10^3
All	1564	**D**	2.43	0.347	9.368×10^3
		D$^{\text{rand}}$	5.35	0.541	1.392×10^4

5.3   Damage Characterization

Though model comparison can inform the existence of damage, we would also like to characterize the extent of damage. We will consider the ordinary least squares estimation procedure in order to characterize damage. Under certain conditions, this procedure can provide standard error estimates for the parameter estimates. Recall from Section 4.2, the OLS parameter estimate given by

$$\hat{q} = \arg\min_{q \in \mathcal{Q}} J(q) \tag{5.26}$$

where now we consider the parameter set $q = (x_D, h_D, v_D)$ and J is given by (5.18). The ordinary least squares error variance estimate is then given by

$$\hat{\sigma}^2 = \frac{J(\hat{q})}{nm - p} \tag{5.27}$$

where p is the number of parameters in the parameter set q, n is the number of temporal nodes and m is the number of spatial nodes (pixels).

The covariance matrix estimate is then given by

$$\Sigma(\hat{q}) = \hat{\sigma}^2 \left(\chi^T(\hat{q}) \chi(\hat{q}) \right)^{-1}, \tag{5.28}$$

where $\chi(\hat{q})$ is the matrix of sensitivities with entries

$$\chi_{i+m(j-1),k}(q) = \left. \frac{\partial}{\partial q_k} U_{ij}(\zeta) \right|_{\zeta=q}, \tag{5.29}$$

for $i = 1, 2, \ldots, m$, $j = 1, 2, \ldots, n$, and $k = 1, 2, \ldots p$. The details of the calculations of these sensitivities are given in Appendix A.2. The standard error estimate for the kth parameter is then given by,

$$\text{SE}(\hat{q}) = \sqrt{\Sigma_{kk}(\hat{q})}. \tag{5.30}$$

We will use a very large number of nodes so for all our parameter sets, the 95% confidence interval is given by

$$95\%\text{Confidence Interval} = (\hat{q} - 1.96 \, \text{SE}(\hat{q}), \hat{q} + 1.96 \, \text{SE}(\hat{q}))$$

and the 99% confidence interval is given by

$$99\%\text{Confidence Interval} = (\hat{q} - 2.58\text{SE}\,(\hat{q}), \hat{q} + 2.58 \, \text{SE}(\hat{q})).$$

This analysis is presented for the same realizations of the random processes $\mathbf{D}_{ij}$ and $\mathbf{D}_{ij}^{\text{rand}}$ as were used in the previous section (Section 5.2). Unlike the damage detection, there are significant differences in the results using realizations of $\mathbf{D}_{ij}$ versus realizations of $\mathbf{D}_{ij}^{\text{rand}}$. All three variables (x_D, h_D, v_D) appear to be well estimated using the realizations of $\mathbf{D}_{ij}$. However, there are many cases where using realizations of $\mathbf{D}_{ij}^{\text{rand}}$ yield values that

Table 5.10: The estimated geometries for $(x_D, h_D, v_D) = (3, 1, 0.5)$

Nodes	$n \times m$	Data	$\hat{\sigma}^2$	$(\hat{x}_D, \hat{h}_D, \hat{v}_D)$	$(\text{SE}(\hat{x}_D), \text{SE}(\hat{h}_D), \text{SE}(\hat{v}_D))$
Left	1012	$\mathbf{D}$	0.028	$(2.9, 0.941, 0.51)$	$(0.086, 0.25, 0.071)$
		$\mathbf{D}^{\text{rand}}$	0.03	$(3.84, 0.653, 0.59)$	$(0.073, 0.18, 0.099)$
Right	1012	$\mathbf{D}$	0.027	$(3.01, 1.01, 0.49)$	$(1.1, 1.4, 0.45)$
		$\mathbf{D}^{\text{rand}}$	0.031	$(4.09, 0.626, 0.58)$	$(0.084, 0.2, 0.12)$
Even	1012	$\mathbf{D}$	0.028	$(2.95, 0.948, 0.5)$	$(0.13, 0.41, 0.1)$
		$\mathbf{D}^{\text{rand}}$	0.031	$(3.88, 0.564, 0.64)$	$(0.083, 0.15, 0.12)$
All	1564	$\mathbf{D}$	0.024	$(2.93, 0.934, 0.51)$	$(0.08, 0.26, 0.07)$
		$\mathbf{D}^{\text{rand}}$	0.027	$(3.89, 0.596, 0.62)$	$(0.067, 0.14, 0.1)$

are significantly different than the true values. In some of these cases, the standard errors are large enough that a 99% confidence interval covers these values.

In Table 5.10 which presents the results using $(x_D, h_D, v_D) = (3, 1, 0.5)$, the estimate $(\hat{x}_D, \hat{h}_D, \hat{v}_D)$ is much closer to the "true" value for the data D_{ij} than that for the data $\mathrm{D}_{ij}^{\text{rand}}$. For this example using a realization of $\mathbf{D}_{ij}^{\text{rand}}$, for each set of pixels, the values $(\hat{h}_D, \hat{v}_D)$ are within the 95% confidence intervals though the estimated values are not close to the "true" value. The estimates of $\hat{x}_D$ for each set of pixels are not only far from the value $x_D = 3$ but the standard error $\text{SE}(\hat{x}_D)$ is small enough so that for each pixel set the 99% confidence interval does not contain the value $x_D = 3$.

We also considered the realizations D_{ij} and $\mathrm{D}_{ij}^{\text{rand}}$ for $(x_D, h_D, v_D) = (3, 2, 1)$ (see Table 5.11). Again for the results of using the realization D_{ij}, the parameter estimates are close to their "true" value and the standard errors are reasonable for all pixel sets. For this realization estimation of $\hat{x}_D$ using the right pixel set is not close to the value $x_D = 3$, however, the estimates for $\hat{x}_D$ using the other pixel sets are within 0.02 of the true value. For every set of pixels, the value $x_D = 3$ is covered by the 95% confidence interval. The right pixel set and the full pixel set ("All") have values of $\hat{h}_D$ close to

Table 5.11: The estimated geometries for $(x_D, h_D, v_D) = (3, 2, 1)$

Nodes	$n \times m$	Data	$\hat{\sigma}^2$	$(\hat{x}_D, \hat{h}_D, \hat{v}_D)$	$(\text{SE}(\hat{x}_D), \text{SE}(\hat{h}_D), \text{SE}(\hat{v}_D))$
Left	1012	$\mathbf{D}$	0.032	$(3.01, 1.99, 1)$	$(0.023, 0.059, 0.015)$
		$\mathbf{D}^{\text{rand}}$	0.048	$(3.02, 3.02, 0.76)$	$(0.041, 0.1, 0.012)$
Right	1012	$\mathbf{D}$	0.03	$(3.02, 2.01, 1)$	$(0.29, 0.41, 0.044)$
		$\mathbf{D}^{\text{rand}}$	0.045	$(3.6, 1.71, 0.93)$	$(0.27, 0.48, 0.072)$
Even	1012	$\mathbf{D}$	0.03	$(3.01, 1.99, 1)$	$(0.027, 0.068, 0.018)$
		$\mathbf{D}^{\text{rand}}$	0.052	$(3.02, 2.87, 0.78)$	$(0.044, 0.11, 0.017)$
All	1564	$\mathbf{D}$	0.026	$(3.01, 1.98, 1)$	$(0.021, 0.054, 0.015)$
		$\mathbf{D}^{\text{rand}}$	0.06	$(3.01, 1.94, 0.95)$	$(0.037, 0.1, 0.027)$

Table 5.12: The estimated geometries for $(x_D, h_D, v_D) = (5, 1, 0.5)$

Nodes	$n \times m$	Data	$\hat{\sigma}^2$	$(\hat{x}_D, \hat{h}_D, \hat{v}_D)$	$(\text{SE}(\hat{x}_D), \text{SE}(\hat{h}_D), \text{SE}(\hat{v}_D))$
Left	1012	$\mathbf{D}$	0.028	$(5.08, 1.04, 0.49)$	$(0.1, 0.47, 0.086)$
		$\mathbf{D}^{\text{rand}}$	0.032	$(5.87, 1.12, 0.51)$	$(0.19, 0.65, 0.11)$
Right	1012	$\mathbf{D}$	0.027	$(4.92, 0.944, 0.51)$	$(0.088, 0.26, 0.071)$
		$\mathbf{D}^{\text{rand}}$	0.031	$(5.4, 1.08, 0.51)$	$(0.089, 0.28, 0.067)$
Even	1012	$\mathbf{D}$	0.028	$(4.95, 0.934, 0.52)$	$(0.12, 0.37, 0.094)$
		$\mathbf{D}^{\text{rand}}$	0.033	$(5.5, 1.12, 0.51)$	$(0.11, 0.3, 0.073)$
All	1564	$\mathbf{D}$	0.024	$(5.05, 1.07, 0.48)$	$(0.092, 0.4, 0.072)$
		$\mathbf{D}^{\text{rand}}$	0.028	$(5.64, 1.39, 0.45)$	$(0.12, 0.41, 0.052)$

$h_D = 2$ which is covered by their respective 95% confidence intervals. The estimates $\hat{h}_D$ for the left and evenly spaced pixel set are both over estimates which are relatively far from the value $h_D = 2$ which is not covered by the 95% confidence interval. We see that the estimate $\hat{v}_D$ in this case is close to the value $v_D = 1$ for the full and right pixel sets while the estimate $\hat{v}_D$ is much smaller than $v_D = 1$ for the left and evenly spaced pixel sets.

The results of the OLS parameter estimation procedure for realizations of $\mathbf{D}^{\text{rand}}_{ij}$ with

Table 5.13: The estimated geometries for $(x_D, h_D, v_D) = (5, 2, 1)$

Nodes	$n \times m$	Data	$\hat{\sigma}^2$	$(\hat{x}_D, \hat{h}_D, \hat{v}_D)$	$(\text{SE}(\hat{x}_D), \text{SE}(\hat{h}_D), \text{SE}(\hat{v}_D))$
Left	1012	$\mathbf{D}$	0.03	$(4.99, 2.01, 1)$	$(0.037, 0.098, 0.02)$
		$\mathbf{D}^{\text{rand}}$	0.038	$(4.96, 1.99, 0.92)$	$(0.044, 0.12, 0.025)$
Right	1012	$\mathbf{D}$	0.029	$(5, 2, 1)$	$(0.027, 0.078, 0.018)$
		$\mathbf{D}^{\text{rand}}$	0.035	$(5.17, 2.31, 0.86)$	$(0.04, 0.1, 0.017)$
Even	1012	$\mathbf{D}$	0.03	$(5, 2.02, 1)$	$(0.027, 0.066, 0.017)$
		$\mathbf{D}^{\text{rand}}$	0.041	$(5.12, 2.22, 0.87)$	$(0.04, 0.1, 0.02)$
All	1564	$\mathbf{D}$	0.026	$(4.99, 2.01, 1)$	$(0.022, 0.058, 0.015)$
		$\mathbf{D}^{\text{rand}}$	0.038	$(5.1, 2.14, 0.89)$	$(0.031, 0.083, 0.017)$

$(x_D, h_D, v_D) = (5, 1, 0.5)$ in Table 5.12 are similar to the results with $(x_D, h_D, v_D) = (3, 1, 0.5)$. The estimates of $(\hat{h}_D, \hat{v}_D)$ are close to $(h_D, v_D) = (1, 0.5)$ and the standard errors $(\text{SE}(\hat{h}_D), \text{SE}(\hat{v}_D))$ are large enough that $(h_D, v_D) = (1, 0.5)$ is within two standard errors of the parameter estimate $(\hat{h}_D, \hat{v}_D)$ for all sets of pixels that we considered. The estimate $\hat{x}_D$ for the realization $\text{D}_{ij}^{\text{rand}}$ is much larger than $x_D = 5$ (though this effect is not as severe as for $x_D = 3$ in Table 5.10) and the standard errors are small so that for each set of pixels the value $x_D = 5$ is not covered by the resepective 95% confidence interval.

Using the realization $\text{D}_{ij}^{\text{rand}}$ with damage given by $(x_D, h_D, v_D) = (5, 2, 1)$ for each estimate, for each set of pixels, the estimates are within 0.22 of the "true" parameter value. Though these estimates are close to the parameter value, many of the standard error estimates are still so small that the "true" parameter value is not covered by the 99% confidence interval. For each set of pixels, the 99% confidence interval of $\hat{v}_D$ does not cover the value $v_D = 1$.

We also considered ellipses that do not have a vertical semi-axis which is much smaller than the horizontal semi-axis. In these examples, this ratio was not maintained in the parameter estimates which were computed using realizations of $\mathbf{D}_{ij}^{\text{rand}}$. In Table 5.14, we

Table 5.14: The estimated geometries for $(x_D, h_D, v_D) = (3, 0.5, 1)$

Nodes	$n \times m$	Data	$\hat{\sigma}^2$	$(\hat{x}_D, \hat{h}_D, \hat{v}_D)$	$(\text{SE}(\hat{x}_D), \text{SE}(\hat{h}_D), \text{SE}(\hat{v}_D))$
Left	1012	$\mathbf{D}$	0.028	$(3.05, 0.512, 0.97)$	$(0.037, 0.015, 0.047)$
		$\mathbf{D}^{\text{rand}}$	0.03	$(3.39, 0.987, 0.66)$	$(0.062, 0.16, 0.063)$
Right	1012	$\mathbf{D}$	0.028	$(2.88, 0.389, 1.2)$	$(0.066, 0.087, 0.51)$
		$\mathbf{D}^{\text{rand}}$	0.032	$(2.96, 0.476, 1.1)$	$(0.12, 0.032, 0.38)$
Even	1012	$\mathbf{D}$	0.028	$(2.99, 0.513, 0.97)$	$(0.047, 0.018, 0.068)$
		$\mathbf{D}^{\text{rand}}$	0.031	$(3.35, 0.962, 0.67)$	$(0.082, 0.22, 0.084)$
All	1564	$\mathbf{D}$	0.025	$(3.05, 0.492, 1)$	$(0.031, 0.014, 0.039)$
		$\mathbf{D}^{\text{rand}}$	0.028	$(3.41, 0.954, 0.67)$	$(0.061, 0.14, 0.061)$

present the results for $(x_D, h_D, v_D) = (3, 0.5, 1)$. The estimates of $(\hat{x}_D, \hat{h}_D, \hat{v}_D)$ for the realization $\mathbf{D}_{ij}$ are farther from the "true" value than in the previous examples. This implies that the geometry of these ellipses pose a problem in the parameter estimation problem. This effect is amplified for the realization $\mathbf{D}_{ij}^{\text{rand}}$. For the pixel sets "Left," "Even," and "All" the parameter estimation procedure produced an ellipse estimate with horizontal semi-axes longer than vertical semi-axes. Also, in these examples the estimate of the center $\hat{x}_D$ is larger than the value $x_D = 3$. The pixel set "Right" produced an estimate which was very close to the "true" value with each 95% confidence interval containing that "true" parameter value. The estimate using the realization of $\mathbf{D}_{ij}$ using the "Right" pixel set is the farthest from the true damage $(x_D, h_D, v_D) = (3, 0.5, 1)$ while the parameter estimate using the "Right" with realizations of $\mathbf{D}_{ij}^{\text{rand}}$ is the closest. This effect occurs because for data generated without pores, the "Right" pixels are the farthest from the damage centered at $x_D = 3$, so there is relatively little information in those pixel sets compared to the other pixel sets. For data generated using realizations of $\mathbf{D}_{ij}^{\text{rand}}$, the larger the distance from the bottom of the damage to the source boundary (ω_4), the larger the error associated with $(u_D^{\text{rand}})_{ij}$ so the "Right" pixel set contains the

Table 5.15: The estimated geometries for $(x_D, h_D, v_D) = (3, 0.5, 1.5)$

Nodes	$n \times m$	Data	$\hat{\sigma}^2$	$(\hat{x}_D, \hat{h}_D, \hat{v}_D)$	$(\text{SE}(\hat{x}_D), \text{SE}(\hat{h}_D), \text{SE}(\hat{v}_D))$
Left	1012	$\mathbf{D}$	0.029	$(2.97, 0.5, 1.5)$	$(3.9 \times 10^{-3}, 6.8 \times 10^{-3}, 0.015)$
		$\mathbf{D}^{\text{rand}}$	0.043	$(3.14, 1.1, 0.9)$	$(0.039, 0.099, 0.057)$
Right	1012	$\mathbf{D}$	0.028	$(2.97, 0.469, 1.6)$	$(0.015, 0.012, 0.06)$
		$\mathbf{D}^{\text{rand}}$	0.037	$(2.59, 0.546, 1.8)$	$(0.051, 0.045, 0.22)$
Even	1012	$\mathbf{D}$	0.029	$(2.95, 0.5, 1.5)$	$(5.5 \times 10^{-3}, 8.3 \times 10^{-3}, 0.017)$
		$\mathbf{D}^{\text{rand}}$	0.04	$(3.19, 1.1, 0.91)$	$(0.06, 0.14, 0.069)$
All	1564	$\mathbf{D}$	0.025	$(2.97, 0.506, 1.5)$	$(3.6 \times 10^{-3}, 6.4 \times 10^{-3}, 0.015)$
		$\mathbf{D}^{\text{rand}}$	0.035	$(3.18, 1.14, 0.88)$	$(0.039, 0.1, 0.051)$

least amount of error due to the approximation of $(u_D^{\text{rand}})_{ij}$ with U_{ij}. We see very similar results for the damage $(x_D, h_D, v_D) = (3, 0.5, 1.5)$ in Table 5.15.

When a damage with $v_D > h_D$ is placed in the horizontal center of the 10 by 2 rectangle, all of the pixel sets contain pixels directly below the center of the damage. Realizations of $\mathbf{D}_{ij}$ and $\mathbf{D}_{ij}^{\text{rand}}$ both yield relatively small standard errors compared to the difference between the parameter estimate and the true parameter set. It appears that in this case, the damage is not as well characterized. In Table 5.17 with $(x_D, h_D, v_D) = (5, 0.5, 1)$, the parameter estimates for the realization $\mathbf{D}_{ij}$ are closer to (5,0.5,1) than those of the realization $\mathbf{D}_{ij}^{\text{rand}}$. In many of these cases, the 95% confidence interval does not contain the true parameter value for this realization of $\mathbf{D}_{ij}$. Using the realization $\mathbf{D}_{ij}^{\text{rand}}$ in this example, the parameter estimates with pixel sets "Left" and "Right" maintain $\hat{v}_D > \hat{h}_D$ while parameter estimates with pixel sets "Even" and "All" invert this inequality resulting in $\hat{v}_D < \hat{h}_D$. The estimate of $\hat{x}_D = 6.18$ using the "Left" pixel set for the realization $\mathbf{D}_{ij}^{\text{rand}}$ is very far from $x_D = 5$ while the estimates of $\hat{x}_D$ for pixel sets "Right," "Even" and "All" are within 0.31 of $x_D = 5$. Though these estimates are different from

Table 5.16: The estimated geometries for $(x_D, h_D, v_D) = (5, 0.5, 1)$

Nodes	$n \times m$	Data	$\hat{\sigma}^2$	$(\hat{x}_D, \hat{h}_D, \hat{v}_D)$	$(\mathrm{SE}(\hat{x}_D), \mathrm{SE}(\hat{h}_D), \mathrm{SE}(\hat{v}_D))$
Left	1012	$\mathbf{D}$	0.029	$(4.98, 0.447, 1.1)$	$(0.021, 0.016, 0.036)$
		$\mathbf{D}^{\mathrm{rand}}$	0.038	$(6.18, 0.633, 1.1)$	$(0.061, 0.061, 0.07)$
Right	1012	$\mathbf{D}$	0.028	$(4.98, 0.439, 1.1)$	$(0.023, 0.016, 0.039)$
		$\mathbf{D}^{\mathrm{rand}}$	0.036	$(4.87, 0.729, 0.86)$	$(0.051, 0.065, 0.065)$
Even	1012	$\mathbf{D}$	0.029	$(4.99, 0.47, 1)$	$(0.031, 0.016, 0.051)$
		$\mathbf{D}^{\mathrm{rand}}$	0.034	$(5.31, 1.2, 0.62)$	$(0.086, 0.21, 0.061)$
All	1564	$\mathbf{D}$	0.025	$(4.98, 0.483, 1)$	$(0.027, 0.012, 0.042)$
		$\mathbf{D}^{\mathrm{rand}}$	0.027	$(5.29, 3.18, 0.41)$	$(0.13, 0.44, 0.016)$

Table 5.17: The estimated geometries for $(x_D, h_D, v_D) = (5, 0.5, 1.5)$

Nodes	$n \times m$	Data	$\hat{\sigma}^2$	$(\hat{x}_D, \hat{h}_D, \hat{v}_D)$	$(\mathrm{SE}(\hat{x}_D), \mathrm{SE}(\hat{h}_D), \mathrm{SE}(\hat{v}_D))$
Left	1012	$\mathbf{D}$	0.028	$(5.03, 0.482, 1.6)$	$(2.9 \times 10^{-3}, 6.4 \times 10^{-3}, 0.012)$
		$\mathbf{D}^{\mathrm{rand}}$	0.054	$(5.92, 0.641, 1.7)$	$(0.014, 6.9 \times 10^{-3}, 0.039)$
Right	1012	$\mathbf{D}$	0.029	$(4.97, 0.487, 1.5)$	$(4.7 \times 10^{-3}, 6.4 \times 10^{-3}, 0.014)$
		$\mathbf{D}^{\mathrm{rand}}$	0.053	$(4.75, 0.834, 1.2)$	$(0.035, 0.032, 0.047)$
Even	1012	$\mathbf{D}$	0.028	$(5, 0.491, 1.5)$	$(4 \times 10^{-3}, 7.3 \times 10^{-3}, 0.017)$
		$\mathbf{D}^{\mathrm{rand}}$	0.045	$(5.15, 1.28, 0.84)$	$(0.071, 0.14, 0.053)$
All	1564	$\mathbf{D}$	0.025	$(5, 0.491, 1.5)$	$(3.2 \times 10^{-3}, 5.9 \times 10^{-3}, 0.013)$
		$\mathbf{D}^{\mathrm{rand}}$	0.039	$(5.17, 1.42, 0.78)$	$(0.044, 0.12, 0.039)$

the "true" parameter value, the standard errors are relatively small, resulting in the "true" parameter value being many standard errors from the parameter estimate. Again, for the larger damage $(x_D, h_D, v_D) = (5, 0.5, 1.5)$, we see similar results in Table 5.17.

In summary, this approximation appears to work very well to detect damage while to characterize damage the homogenization approximation works well in some cases. This is dependent on shape of the damage (it appears to characterize damage with $h_D > v_D$ better than damage with $h_D < v_D$) and the choice of pixel set.

Chapter 6

Conclusions

In Chapter 2, we considered a model of heat on a porous domain. We developed a geometry generation algorithm using concepts from [13] and [30]. This was essential to automate the generation of random geometries. We used this algorithm to examine the numerical error associated with the finite element method for the heat equation, and to simulate perforated domains with and without elliptical damage.

After we developed this method of simulating data, we went on to consider an approximation using the results of homogenization theory in Chapter 3. We considered both graphical representations and the Frobenius norm of this error. We found that using the limit system which results from homogenization theory significantly decreases the computational time for perforated domains with 2, 5 and 10% porosity. The error associated with using the results of homogenization theory was smaller on average for lower porosity levels. Also, in the simulations that we performed, the homogenization approximation was closer in Frobenius norm more often to the solution of the heat equation on a randomly generated perforated domain than to the solution of the heat equation on a periodically perforated domain. In these examples, we also found that the error

associated with using the limit system which results from homogenization theory rather than the solution of the heat equation on a perforated domain was reasonable in the forward problem.

We went on to consider the effect of using the model derived from homogenization theory in statistical estimation procedures. We simulated data using both solutions of this system and the solution of the heat equation on perforated domains with 98% percent porosity. We added two kinds of noise. In Section 4.2 we considered the case with absolute added random noise and in Section 4.3 we considered data with added relative random noise. We used this simulated data to estimate coefficients in partial differential equation. We found that estimating α, the thermal diffusivity, is well posed while estimating γ, the heat loss in the direction orthogonal to the 2-D specimen is ill posed. For the well posed inverse problems, we found that there was little difference between using data generated using the solution of the heat equation on the randomly perforated domain than using the homogenization approximation. This suggests that for well posed parameters in the inverse problem, the error associated with the homogenization approximation does not affect the results ordinary least squares estimation procedure nor the results of the generalized least squares estimation procedure.

Finally, we considered using parameter estimation procedures to detect and characterize damage. We found that these techniques for the damages that we considered detected damage very well. In these examples, there was no clear difference between using data generated using the solution of the heat equation on a random domain, and data generated using the homogenization approximation. In characterizing elliptical damage, there does appear to be a difference in using data generated using the solution of the heat equation on a perforated domain rather than using the homogenization approximation in estimating the center and the size of the elliptical damage. As one would expect, the

estimates of the center and semi-axes lengths using data generated using the homogenization approximation were always closer to the true value than estimates of the center and semi-axes lengths using data generated using the solution of the heat equation on a perforated domain. The accuracy of the estimates of the center x coordinate, horizontal semi-axis and the vertical semi-axis (x_D, h_D, v_D) varied over the examples using data generated the solution of the heat equation on the randomly perforated domain. The examples with $h_D < v_D$ did not preserve this inequality in the estimates of h_D and v_D in most cases while in the examples with $h_D > v_D$ the inequality was preserved. When we estimated (x_D, h_D, v_D) using data generated using the solution of the heat equation on the perforated domain, we noticed significant differences between using different pixel sets. It appeared that some of the pixel sets were more sensitive to the error associated with using the homogenization approximation in the inverse problem. It is worthwhile to note that in most cases the estimated area of the damage was larger in the estimate than the area of the damage itself. This suggests that this estimation procedure may not estimate the center or the size correctly but it will not give an estimate that is smaller. These methods could be used as a first estimate of damage which could be further resolved using another nondestructive evaluation technique.

REFERENCES

[1] Charalambos D. Aliprantis and Owen Burkinshaw. *Principles of real analysis*. Elsevier North Holland, Inc., 1981.

[2] N. S. Bakhvalov and J Saint Jean Paulin. Homogenization for thermoconductivity in a porous medium with periods of different orders in the different directions. *Asymptotic Analysis*, 13(3), 1996.

[3] H. T. Banks, Brittany Boudreaux, Amanda Keck Criner, Krista Foster, Cerena Uttal, Thomas Vogel, and William P. Winfree. Thermal interrogation of porous materials. Technical Report CRSC-TR08-11, Center for Research in Scientific Computation, North Carolina State University, 2008.

[4] H. T. Banks, Brittany Boudreaux, Amanda Keck Criner, Krista Foster, Cerena Uttal, Thomas Vogel, and William P. Winfree. Thermal based damage detection in porous materials. *Inverse Problems in Science and Engineering*, 18, 2010.

[5] H T Banks, D. Cioranescu, A. K. Criner, and W P Winfree. Modeling the flash-heat experiment on porous domains. *Quarterly of Applied Mathematics*, 2010.

[6] H. T. Banks, D. Cioranescu, A. K. Criner, and W P Winfree. Modeling the flash-heat experiment on porous domains. Technical Report CRSC-TR10-06, Center for Research in Scientific Computation, North Carolina State University, May, 2010.

[7] H. T. Banks, M. Davidian, J.R. Samuels Jr., and Karyn L. Sutton. An inverse problem statistical methodology summary. Technical Report 1, Center for Research in Scientific Computation and Center for Quantitative Sciences in Biomedicine, 2008.

[8] H. T. Banks, Sava Dediu, and S. L. Ernstberger. Sensitivity functions and their uses in inverse problems. *Journal of Inverse and Ill-Posed Problems*, 15(7):683–708, 2007.

[9] H. T. Banks and B. G. Fitzpatrick. Statistical methods for model comparison in parameter estimation problems for distributed systems. *Journal of Mathematical Biology*, 28:501–527, 1990.

[10] H. T. Banks, N. L. Gibson, and W. P. Winfree. Void detection in complex geometries. Technical report, Center for Research in Scientific Computation, 2008.

[11] H T Banks, Fumio Kojima, and W P Winfree. Boundary estimation problems arising in thermal tomography. *Inverse Problems*, 6(6):897–921, 1990.

[12] H.T Banks, K. Holm, and F. Kappel. Comparison of optimal design methods in inverse problems. *Inverse Problems*, 2011.

[13] Kathleen L. Bihari. *Analysis of Thermal Conductivity in Composite Adhesives*. PhD thesis, North Carolina State University, 2001.

[14] Horatio Scott Carslaw and John Conrad Jaeger. *Conduction of Heat in Solids*. Oxford University Press, 1959.

[15] D. Cioranescu, A. Damlamian, and G. Griso. The periodic unfolding method in homogenization. *SIAM Journal of Mathematical Analysis*, 40(4):1585–1620, 2008.

[16] D. Cioranescu, A. Damlamian, and G. Griso. The periodic unfolding method in domains with holes, 2010; *to appear*.

[17] D. Cioranescu, P. Donato, and R. Zaki. Asymptotic behavior of elliptic problems in perforated domains with nonlinear boundary conditions. *Asymptotic Analysis*, 53(4):209–235, 2007.

[18] D. Cioranescu and J Saint Jean Paulin. *Homogenization of Reticulated Structures*, volume 136 of *Applied Mathematical Sciences*. Springer–Verlag, New York, 1999.

[19] Doina Cioranescu and Patrizia Donato. *An Introduction to Homogenization*, volume 17 of *Oxford lecture series in mathematics and its applications*. Oxford University Press, 1999.

[20] Doina Cioranescu, Patrizia Donato, and Rachad Zaki. The periodic unfolding method in perforated domains. *Portugaliae Mathematica*, 63(4):467–496, 2006.

[21] K. Elliott Cramer, William P. Winfree, Kenneth Hodges, Ajay Koshti, Daniel Ryan, and Walter W. Reinhardt. Status of thermal NDT of space shuttle materials at NASA. In *9th Joint FAA/DoD/NASA Conference on Aging Aircraft*, 2007.

[22] M. Davidian and D.M. Giltinan. *Nonlinear models for repeated measurement data*. Chapman & Hall, 1995.

[23] P. Donato and A. Nabil. Homogenization and correctors for the heat equation in perforated domains. *Ricerche di Matematica*, 50(1):115–144, 2001.

[24] Frank P. Incropera and David P. DeWitt. *Introduction to Heat Transfer*. John Wiley & Sons, Inc, 1996.

[25] The Mathworks, Inc. *Partial Differential Equation Toolbox 1: User's Guide*, 2008.

[26] W. J. Parker, R. J. Jenkings, C. P. Butler, and G. L. Abbott. Flash method of determining thermal diffusivity, heat capacity, and thermal conductivity. *Journal of Applied Physics*, 32(9):1679–1684, 1961.

[27] Peter J. Shull, editor. *Nondestructive Evaluation: Theory, techniques, and applications.* Marcel Dekker, Inc., 2001.

[28] Anna Stewart, Greg Carman, and Lance Richards. Nondestructive evaluation technique utilizing embedded thermal fiber optic sensors. *Journal of Composite Materials*, 37(24), 2003.

[29] Pavel Šolin. *Partial Differential Equations and the Finite Element Method.* John Wiley & Sons, Hoboken, NJ, 2006.

[30] Wenping Wang, Jiaye Wang, and Myung-Soo Kim. An algebraic condition for the separation of two ellipsoids. *Computer Aided Geometric Design*, 18(6):531 – 539, 2001.

[31] William P. Winfree, Eric I. Madaras, K. Elliot Cramer, Patricia A. Howell, Kenneth L. Hodges, Jeffrery P. Seebo, and John L. Grainger. NASA Langley inspection of rudder and composite tail of American Airlines flight 587. In *46th AIAA/ASME/ASCE/AHS/ASC Structures, Structural Dynamics and Materials Conference*, 2005.

APPENDIX

Appendix A

Sensitivities

A.1   Partial Differential Equation Sensitivities

We use the finite element method to numerically solve (4.1) and (4.2). Here, we will discuss the numerical solution of (4.2) and the sensitivity functions in (4.9); see [4] for discussion of the numerical solution of (4.1). The finite element method approximates the infinite dimensional solution of a partial differential equation with a finite dimensional approximation. The domain $(\widehat{\Omega})$ is discretized using the Delaunay triangulation. The finite dimensional solution is taken from the space of piecewise two dimensional affine functions, where the solution is affine on each mesh element (see [25], [29] and [5] for details). Specifically, in [5], we discussed the numerical approximation of U, the solution of (4.2), given by $u^N(t, \vec{x}) = \displaystyle\sum_{j=1}^{N} T_j(t)\phi_j(\vec{x})$ where $\phi_j(\vec{x})$ are piecewise affine basis element and $T_j(t)$ are their time dependent coefficients. The coefficients $T_j(t)$ are found by solving the ordinary differential equation for $\vec{T}(t)$ with entries $T_j(t)$

$$p_V M \frac{d}{dt}\vec{T}(t) + (\alpha K + \lambda D + p_V \gamma M)\vec{T}(t) = S_f \mathcal{I}_{[t_0, t_s]}(t)\vec{f}, \qquad (\text{A.1})$$

where M is an $N \times N$ positive definite matrix with elements $m_{ij} = \langle \phi_i, \phi_j \rangle$, K is an $N \times N$ positive definite matrix with elements $k_{ij} = \langle \nabla \phi_i, A^0 \nabla \phi_j \rangle$, D is an $N \times N$ matrix with components $d_{ij} = \int_{\partial \widehat{\Omega}} \phi_i \phi_j \, ds$, $\vec{f}$ is an N-vector with components $f_i = \int_{\omega_4} \phi_i(x, 0) dx$ and $\vec{T}$ is an N column vector. To approximate $U_{ij}(\theta^\#)$ in (4.3), we explicitly integrate the approximation $u^N(t_j, \vec{x})$ which is piecewise affine on the source boundary ω_4 so we use

$$U_{ij}(\theta^\#) \approx \frac{1}{l} \int_{x_i}^{x_i + \ell} u^N(t_j, s, 0; \theta^\#) \, ds.$$

Recall that in order to calculate the covariance matrices, we calculate the covariance matrix

$$\chi_{i+m(j-1),k}(\theta) = \left. \frac{\partial}{\partial \theta_k} U_{ij}(\zeta) \right|_{\zeta = \theta}.$$

Throughout both the generalized least squares and ordinary least squares parameter estimation procedures, it is tacitly assumed that we use numerical estimations with reasonable convergence and that the admissible set of parameter is compact and finite dimensional (see [9] and [7]). Given these assumptions, in both (4.11) and (4.25), we may estimate χ with the derivative of the numerical solution itself. Explicitly, we use

$$\chi_{i+m(j-1),k}(\theta) \approx \chi^N_{i+m(j-1),k}(\theta) = \left. \frac{\partial}{\partial \theta_k} \left(\int_{x_i}^{x_i + \ell} u^N(t_j, s, 0; \zeta) \, ds \right) \right|_{\zeta = \theta}. \tag{A.2}$$

Noting that the spatial nodes x_i and the interval width ℓ are parameter independent, we may move the derivative under the integral and replace u^N with its definition

$$\left. \frac{\partial}{\partial \theta_k} \left(\int_{x_i}^{x_i + \ell} u^N(t_j, s, 0; \zeta) \, ds \right) \right|_{\zeta = \theta} = \int_{x_i}^{x_i + \ell} \left. \frac{\partial}{\partial \theta_k} \sum_{j=1}^{N} T_j(t; \zeta) \phi_j(s, 0) \right|_{\zeta = \theta} ds$$

Now, recalling that the basis elements ϕ_j are independent of θ and only $T_j(t; \theta)$ are

dependent on $\theta = (\gamma, \alpha, \lambda)$ in (A.1), we have

$$\int_{x_i}^{x_i+\ell} \frac{\partial}{\partial \theta_k} \sum_{j=1}^{N} T_j(t;\zeta)\phi_j(s,0)\bigg|_{\zeta=\theta} ds = \int_{x_i}^{x_i+\ell} \sum_{j=1}^{N} \phi_j(s,0)\left(\frac{\partial}{\partial \theta_k}T_j(t;\zeta)\right)\bigg|_{\zeta=\theta} ds.$$

We need to solve for $\frac{\partial}{\partial \gamma}T_j(t;\zeta)$, $\frac{\partial}{\partial \alpha}T_j(t;\zeta)$, and $\frac{\partial}{\partial \lambda}T_j(t;\zeta)$. First, in order to calculate $\frac{\partial}{\partial \gamma}T_j(t;\theta)$, we differentiate (A.1) with respect to γ. Let $\vec{T}^\gamma(t)$ denote $\frac{\partial}{\partial \gamma}\vec{T}(t)$, and recall that M, K, D, $\vec{f}$ are independent of γ. By the chain rule, $\frac{\partial}{\partial \gamma}(p_V\gamma M\vec{T}(t)) = p_V\gamma M\vec{T}^\gamma(t) + p_V M\vec{T}(t)$, so differentiating (A.1) yields

$$p_V M\frac{d}{dt}\vec{T}^\gamma(t) + (\alpha K + \lambda D + p_V\gamma M)\vec{T}^\gamma(t) + p_V M\vec{T}(t) = \vec{0}_{N\times 1}. \tag{A.3}$$

In (A.3) above, M, K and D are as defined in (A.1), and $\vec{0}_{N\times 1}$ is the $N \times 1$ vector of zeros. The ordinary differential equation (A.3) has a term that involves $\vec{T}(t)$, so (A.3) and (A.1) must be solved simultaneously. Similarly, we take the derivative of (A.1) with respect to α to obtain

$$p_V M\frac{d}{dt}\vec{T}^\alpha(t) + (\alpha K + \lambda D + p_V\gamma M)\vec{T}^\alpha(t) + K\vec{T}(t) = \vec{0}_{N\times 1}, \tag{A.4}$$

which must also be solved with (A.1). Finally, we take the derivative of (A.1) with respect to λ to find the system of ordinary differential equations for $\vec{T}^\lambda$ below

$$p_V M\frac{d}{dt}\vec{T}^\lambda(t) + (\alpha K + \lambda D + p_V\gamma M)\vec{T}^\lambda(t) + D\vec{T}(t) = \vec{0}_{N\times 1}, \tag{A.5}$$

which also must be solved simultaneously with (A.1).

A.2 Damage Sensitivities

Recall from Section 5.1 the model of anisotropic heat flow through a damaged domain below,

$$
\begin{cases}
p_V \dfrac{\partial u^D}{\partial t} - \alpha \nabla \cdot (A^0 \nabla u^D) = 0 & \text{in } \mathcal{T} \times \hat{\Omega}^D(q) \\[2mm]
\alpha \dfrac{\partial u^D}{\partial \eta_{A^0}} = 0 & \text{on } \mathcal{T} \times (\omega_1 \cup \omega_2(q) \cup \omega_3) \\[2mm]
\alpha \dfrac{\partial u^D}{\partial \eta_{A^0}} = S_f \mathcal{I}_{[0,t_s]}(t) & \text{on } \mathcal{T} \times \omega_4 \\[2mm]
u^D(0, \vec{x}) = 0 & \text{for } \vec{x} \in \hat{\Omega}^D.
\end{cases}
\tag{A.6}
$$

As in previous chapters α is the thermal diffusivity, p_V is the proportion of the material in the porous domain (here, $p_V = 0.9$), A^0 is the anisotropy matrix associated with the results of homogenization theory, S_f is the intensity of the heat lamp and $\mathcal{I}_{[0,t_s]}(t)$ is the heaviside function. The geometry on which the partial differential equation (A.6) is defined is given by $\hat{\Omega}^D(q) = \hat{\Omega} \setminus E^D(q)$ where as before $\hat{\Omega} = \{(x,y) : 0 \leq x \leq L_1, \text{ and } 0 \leq y \leq L_2\}$ and the elliptical damage with center (x_D, y_D), horizontal semi-axis h_D and vertical semi-axis v_D is given by $E^D(q) = \{(x,y) : \left(\dfrac{x - x_D}{h_D}\right)^2 + \left(\dfrac{y - y_D}{v_D}\right)^2 < 1\}$. The boundaries $\omega_1, \omega_3, \omega_4$ are the left, right and bottom boundaries of $\hat{\Omega}$, respectively. The back boundary of $\hat{\Omega}^D$, $\omega_2^D(q)$ is parametrized by (x_D, y_D, h_D, v_D) with $y_D = 2.25$ fixed. The piecewise function r is given by

$$
r(x; q) = \begin{cases}
L_2 & \text{for } 0 \leq x \leq x_L(q) \\[2mm]
y_D - v_D \sqrt{1 - \left(\dfrac{x - x_D}{h_D}\right)^2} & \text{for } x_L(q) < x < x_R(q) \\[2mm]
L_2 & \text{for } x_R(q) \leq x \leq L_1,
\end{cases}
\tag{A.7}
$$

where the left end point $x_L(q)$ is given by $x_L(q) = x_D - h_D\sqrt{1 - \left(\dfrac{yD - L2}{v_D}\right)^2}$ and the right end point is given by $x_R(q) = x_D + h_D\sqrt{1 - \left(\dfrac{y_D - L_2}{v_D}\right)^2}$. The damaged back boundary of $\hat{\Omega}^D(q)$ is then given by $\omega_2^D(q) = \{(x,y) : 0 \le x \le L_1 \text{ and } y = r(x;q)\}$. In Section 5.1, we derived the weak formulation of (A.6) using the method of maps from [11] given by

$$\frac{p_V}{L_2}\int_{\hat{\Omega}} \frac{\partial}{\partial t}u(t,\vec{x};q)\phi(\vec{x})r(x;q)\,d\vec{x} \;-\; \alpha\int_{\hat{\Omega}} \nabla u(t,\vec{x};q)\cdot B(\vec{x};q)\nabla\phi(\vec{x})\,d\vec{x}$$

(A.8)

$$= \; S_f\mathcal{I}_{[0,t_s]}(t)\int_{\omega_4} \gamma_{\omega_4}(\phi)\,d\xi_{\omega_4}.$$

where $B(\vec{x};q)$ is a 2×2 matrix with entries

$$b_{11}(\vec{x};q) = a_{11}^0\frac{r(x;q)}{L_2}$$

$$b_{12}(\vec{x};q) = -a_{11}^0\,y\,\frac{r'(x;q)}{L_2} + a_{12}^0$$

$$b_{21}(\vec{x};q) = -a_{11}^0\,y\,\frac{r'(x;q)}{L_2} + a_{21}^0$$

$$b_{22}(\vec{x};q) = a_{11}^0\,y^2\frac{(r'(x;q))^2}{r(x;q)L_2} - \frac{r'(x;q)}{r(x;q)}y(a_{12}^0 + a_{21}^0) + a_{22}^0\frac{L_2}{r(x;q)}.$$

The finite element solution of (A.8) is given by solution of

$$p_V C(q)\frac{d}{dt}\vec{u}(t) + \alpha K(q)\vec{u}(t) = S_f\mathcal{I}_{[0,t_s]}(t)\vec{f},$$

(A.9)

118

where

$$C_{ij}(q) \;=\; \frac{1}{L_2} \int_{\hat{\Omega}} \phi_j(\vec{x})\phi_i(\vec{x})r(x;q)\,d\vec{x} \qquad \text{for } i,j = 1,2,\dots N$$

$$K_{ij}(q) \;=\; \int_{\Omega} \nabla\phi_j(\vec{x}) \cdot B(\vec{x};q)\nabla\phi_i(\vec{x})\,d\vec{x} \quad \text{for } i,j = 1,2,\dots N$$

$$\vec{f}_i \;=\; \int_{\omega_4} \gamma_{\omega_4}(\phi_i)\,d\xi_{\omega_4} \qquad\qquad \text{for } i = 1,2,\dots N \tag{A.10}$$

$$\vec{u}_i(t) \;=\; u_i(t) \qquad\qquad\qquad \text{for } i = 1,2,\dots N.$$

In order to calculate the sensitivities, we take the derivative of the weak formulation (A.11) with respect to q. Let's consider the first term of the right hand side

$$\frac{\partial}{\partial q}\left(\int_{\hat{\Omega}} \frac{p_V}{L_2}\frac{\partial}{\partial t}u(t,\vec{x};q)\phi(\vec{x})r(x;q) - \alpha\nabla u(t,\vec{x};q)\cdot B(\vec{x};q)\nabla\phi(\vec{x})\,d\vec{x} \right)$$

$$= \frac{\partial}{\partial q}\left(S_f \mathcal{I}_{[0,t_s]}(t) \int_{\omega_4} \gamma_{\omega_4}(\phi)\,d\xi_{\omega_4} \right), \tag{A.11}$$

where $q = (x_D, h_D, v_D)$. Noting that the term on the left hand side do not depend on q, we have that the left hand side is zero.

In order to calculate the first term, we must find

$$\frac{\partial}{\partial q}\int_{\hat{\Omega}}\frac{\partial}{\partial t}u(t,\vec{x};q)\phi(\vec{x})\frac{r(x;q)}{L_2}\,d\vec{x}=\int_0^{L_2}\frac{\partial}{\partial q}\left(\int_0^{L_1}\frac{\partial}{\partial t}u(t,\vec{x};q)\phi(\vec{x})\frac{r(x;q)}{L_2}\,dx\right)\,dy$$

$$=\int_0^{L_2}\left(\frac{\partial}{\partial q}\left(\int_0^{x_L(q)}\frac{\partial}{\partial t}u(t,\vec{x};q)\phi(\vec{x})\,dx\right)+\frac{\partial}{\partial q}\left(\int_{x_L(q)}^{x_R(q)}\frac{\partial}{\partial t}u(t,\vec{x};q)\phi(\vec{x})\frac{r(x;q)}{L_2}\,dx\right)\right.$$

$$\left.+\frac{\partial}{\partial q}\left(\int_{x_R(q)}^{L_1}\frac{\partial}{\partial t}u(t,\vec{x};q)\phi(\vec{x})\,dx\right)\right)\,dy.$$

Now, using Leibniz rule to differentiate the integrals with parameter dependent end points (see [1]),

$$=\int_0^{L_2}\left(\frac{\partial}{\partial q}(x_L(q))\frac{\partial}{\partial t}u(t,x_L(q),y;q)\phi(x_L(q),y)+\int_0^{x_L(q)}\frac{\partial}{\partial q}\left(\frac{\partial}{\partial t}u(t,\vec{x};q)\phi(\vec{x})\right)\,dx\right.$$

$$+\frac{\partial}{\partial q}(x_R(q))\frac{\partial}{\partial t}u(t,x_R(q),y;q)\phi(x_R(q),y)\frac{r(x_R(q);q)}{L_2}$$

$$-\frac{\partial}{\partial q}(x_L(q))\frac{\partial}{\partial t}u(t,x_L(q),y;q)\phi(x_L(q),y)\frac{r(x_L(q);q)}{L_2}$$

$$+\int_{x_L(q)}^{x_R(q)}\frac{\partial}{\partial q}\left(\frac{\partial}{\partial t}u(t,\vec{x};q)\phi(\vec{x})\frac{r(x;q)}{L_2}\right)\,dx$$

$$\left.-\frac{\partial}{\partial q}(x_R(q))\frac{\partial}{\partial t}u(t,x_R(q),y;q)\phi(x_R(q),y)+\int_{x_R(q)}^{L_1}\frac{\partial}{\partial q}\left(\frac{\partial}{\partial t}u(t,\vec{x};q)\phi(\vec{x})\right)\,dx\right)\,dy,$$

noting that $\frac{\partial}{\partial t}u(t,\vec{x};q)$ and $r(x;q)$ are continuous in x so the end point terms cancel each

other out and denoting $\frac{\partial}{\partial q} u = v^q$, we obtain

$$\int_0^{L_2} \left(\int_0^{x_L(q)} \frac{\partial}{\partial t} v^q(t, \vec{x}; q) \phi(\vec{x}) \, dx + \int_{x_L(q)}^{x_R(q)} \frac{\partial}{\partial t} v^q(t, \vec{x}; q) \phi(\vec{x}) \frac{r(x;q)}{L_2} \, dx \right.$$

$$+ \frac{1}{L_2} \int_{x_L(q)}^{x_R(q)} \frac{\partial}{\partial t} u(t, \vec{x}; q) \phi(\vec{x}) \frac{\partial}{\partial q} (r(x;q)) \, dx + \left. \int_{x_R(q)}^{L_1} \frac{\partial}{\partial t} v^q(t, \vec{x}; q) \phi(\vec{x}) \, dx \right) dy$$

$$= \int_0^{L_2} \int_0^{L_1} \frac{\partial}{\partial t} v^q(t, \vec{x}; q) \phi(\vec{x}) \frac{r(x;q)}{L_2} \, dx \, dy$$

$$+ \frac{1}{L_2} \int_0^{L_2} \int_{x_L(q)}^{x_R(q)} \frac{\partial}{\partial t} u(t, \vec{x}; q) \phi(\vec{x}) \frac{\partial}{\partial q} (r(x;q)) \, dx \, dy.$$

In order to calculate the second term of the left hand side, we must calculate

$$\frac{\partial}{\partial q} \left(\int_{\hat{\Omega}} \nabla u(t, \vec{x}; q) \cdot B(\vec{x}; q) \nabla \phi(\vec{x}) \, d\vec{x} \right).$$

In the previous calculation, the integrand was continuous. Several terms of $B(\vec{x}; q)$ are not continuous, so we will define $B(\vec{x}; q)$ in the piecewise fashion

$$B(\vec{x}; q) = \begin{cases} B_L(\vec{x}; q) & \text{for } 0 \leq y \leq L_2,\ 0 \leq x < x_L(q) \\ B_C(\vec{x}; q) & \text{for } 0 \leq y \leq L_2,\ x_L(q) \leq x < x_R(q) \\ B_R(\vec{x}; q) & \text{for } 0 \leq y \leq L_2,\ x_R(q) \leq x \leq L_1. \end{cases} \quad \text{(A.12)}$$

Here we should note that $B_L(\vec{x}; q) = B_R(\vec{x}; q) = A^0$. Using this notation we obtain

$$\frac{\partial}{\partial q} \int_{\hat{\Omega}} \nabla u(t, \vec{x}; q) \cdot B(\vec{x}; q) \nabla \phi(\vec{x}) \, d\vec{x}$$

$$= \int_0^{L_2} \frac{\partial x_L(q)}{\partial q} \nabla u(t, x_L(q), y; q) \cdot B_L(x_L(q), y; q) \nabla \phi(x_L(q), y) \, dy$$

$$- \int_0^{L_2} \frac{\partial x_L(q)}{\partial q} \nabla u(t, x_L(q), y; q) \cdot B_C(x_L(q), y; q) \nabla \phi(x_L(q), y) \, dy$$

$$+ \int_0^{L_2} \frac{\partial x_R(q)}{\partial q} \nabla u(t, x_R(q), y; q) \cdot B_C(x_R(q), y; q) \nabla \phi(x_R(q), y) \, dy$$

$$- \int_0^{L_2} \frac{\partial x_R(q)}{\partial q} \nabla u(t, x_R(q), y; q) \cdot B_R(x_R(q), y; q) \nabla \phi(x_R(q), y) \, dy$$

$$+ \int_0^{L_2} \int_0^{x_L(q)} \frac{\partial}{\partial q} \left(\nabla u(t, \vec{x}; q) \cdot B_L(\vec{x}; q) \nabla \phi(\vec{x}) \right) \, dx$$
$$+ \int_0^{L_2} \int_{x_L(q)}^{x_R(q)} \frac{\partial}{\partial q} \left(\nabla u(t, \vec{x}; q) \cdot B_C(\vec{x}; q) \nabla \phi(\vec{x}) \right) \, dx \, dy$$

$$+ \int_0^{L_2} \int_{x_R(q)}^{L_1} \frac{\partial}{\partial q} \left(\nabla u(t, \vec{x}; q) \cdot B_R(\vec{x}; q) \nabla \phi(\vec{x}) \right) \, dx \, dy$$

$$= \int_0^{L_2} \frac{\partial x_L(q)}{\partial q} \nabla u(t, x_L(q), y; q) \cdot \left(A^0 - B_C(x_L(q), y; q) \right) \nabla \phi(x_L(q), y) \, dy$$

$$+ \int_0^{L_2} \frac{\partial x_R(q)}{\partial q} \nabla u(t, x_R(q), y; q) \cdot \left(B_C(x_R(q), y; q) - A^0 \right) \nabla \phi(x_L(q), y) \, dy$$

$$+ \int_0^{L_2} \left(\int_0^{x_L(q)} \nabla v^q(t, \vec{x}; q) \cdot A^0 \nabla \phi(\vec{x}) \, dx + \int_{x_L(q)}^{x_R(q)} \nabla v^q(t, \vec{x}; q) \cdot B_C(\vec{x}; q) \nabla \phi(\vec{x}) \, dx \right) dy$$

$$+ \int_0^{L_2} \left(\int_{x_L(q)}^{x_R(q)} \nabla u(t, \vec{x}; q) \frac{\partial}{\partial q} (B_C(\vec{x}; q)) \nabla \phi(\vec{x}) \, dx + \int_{x_R(q)}^{L_1} \nabla v^q(t, \vec{x}; q) \cdot A^0 \nabla \phi(\vec{x}) \, dx \right) dy$$

$$= \int_0^{L_2} \frac{\partial x_L(q)}{\partial q} \nabla u(t, x_L(q), y; q) \cdot \left(A^0 - B_C(x_L(q), y; q) \right) \nabla \phi(x_L(q), y) \, dy$$

$$+ \int_0^{L_2} \frac{\partial x_R(q)}{\partial q} \nabla u(t, x_R(q), y; q) \cdot \left(B_C(x_R(q), y; q) - A^0 \right) \nabla \phi(x_L(q), y) \, dy$$

$$+ \int_0^{L_2} \int_0^{L_1} \nabla v^q(t, \vec{x}; q) \cdot B(\vec{x}; q) \nabla \phi(\vec{x}) \, dx \, dy$$
$$+ \int_0^{L_2} \int_{x_L(q)}^{x_R(q)} \nabla u(t, \vec{x}; q) \frac{\partial}{\partial q} (B_C(\vec{x}; q)) \nabla \phi(\vec{x}) \, dx \, dy$$

Combining the terms we obtain the weak formulation

$$
p_V \left(\int_{\hat{\Omega}} \frac{\partial}{\partial t} v^q(t, \vec{x}; q) \phi(\vec{x}) \frac{r(x; q)}{L_2} \, d\vec{x} + \frac{1}{L_2} \int_0^{L_2} \int_{x_L(q)}^{x_R(q)} \frac{\partial}{\partial t} u(t, \vec{x}; q) \phi(\vec{x}) \frac{\partial}{\partial q} (r(x; q)) \, dx \, dy \right)
$$

$$
+ \alpha \left(\int_0^{L_2} \frac{\partial x_L(q)}{\partial q} \nabla u(t, x_L(q), y; q) \cdot \left(A^0 - B_C(x_L(q), y; q) \right) \nabla \phi(x_L(q), y) \, dy \right.
$$

$$
+ \int_0^{L_2} \frac{\partial x_R(q)}{\partial q} \nabla u(t, x_R(q), y; q) \cdot \left(B_C(x_R(q), y; q) - A^0 \right) \nabla \phi(x_L(q), y) \, dy
$$

$$
+ \int_{\hat{\Omega}} \nabla v^q(t, \vec{x}; q) \cdot B(\vec{x}; q) \nabla \phi(\vec{x}) \, d\vec{x} + \int_0^{L_2} \int_{x_L(q)}^{x_R(q)} \nabla u(t, \vec{x}; q) \frac{\partial}{\partial q} (B_C(\vec{x}; q)) \nabla \phi(\vec{x}) \, dx \, dy \right)
$$

$$
= 0.
$$

Similar to our derivation of (A.9), we take $(\tilde{v}^q)^N = \sum_{j=1}^{N} v_j^q(t) \phi_j(\vec{x})$ to derive the system of ordinary differential equations

$$
C(q) \frac{d}{dt} \vec{v}^q(t) + \alpha K(q) \vec{v}^q(t) + p_V C_q(q) \frac{d}{dt} \vec{u}(t) + \alpha A_q(q) \vec{u} = \vec{0}, \tag{A.13}
$$

where $C(q)$, $K(q)$, $\vec{u}(t)$ are defined as in (A.10). The matrices $C_q(q)$, $A_q(q)$, $\vec{v}^q(t)$ and $\vec{0}$ are defined by

$$[C_q(q)]_{ij} \;=\; \frac{1}{L_2} \int_0^{L_2} \int_{x_L(q)}^{x_R(q)} \phi_j(\vec{x})\phi_i(\vec{x})\frac{\partial}{\partial q}(r(x;q))\, dx\, dy \qquad \text{for } i,j = 1,2,\ldots N$$

$$[A_q(q)]_{ij} \;=\; \int_0^{L_2} \frac{\partial x_L(q)}{\partial q}\nabla\phi_j(x_L(q),y)\cdot\left(A^0 - B_C(x_L(q),y)\right)\nabla\phi_i(x_L(q),y)\, dy$$

$$+\; \int_0^{L_2} \frac{\partial x_R(q)}{\partial q}\nabla\phi_j(x_R(q),y)\cdot\left(B_C(x_R(q),y) - A^0\right)\nabla\phi_i(x_R(q),y)\, dy$$

$$+\; \int_0^{L_2} \int_{x_L(q)}^{x_R(q)} \nabla\phi_j(\vec{x})\cdot\left(\frac{\partial}{\partial q}(B(\vec{x};q))\nabla\phi_i(\vec{x})\right)\, dx\, dy \quad \text{for } i,j = 1,2,\ldots N$$

$$[\vec{v}^q(t)]_j \;=\; v_j^q(t) \qquad \text{for } i,j = 1,2,\ldots N$$

$$[\vec{0}]_i \;=\; 0 \qquad \text{for } i = 1,2,\ldots N.$$

In order to solve $\vec{v}^q(t)$ in (A.13), one must first solve (5.12) for $\vec{u}(t)$ and obtain $\dfrac{d}{dt}\vec{u}(t)$ by calculating

$$\frac{d}{dt}\vec{u}(t) = \frac{1}{p_V}C(q)^{-1}\left(S_f \mathcal{I}_{[0,t_s]}(t)\vec{f} - \alpha K(q)\vec{u}(t)\right).$$

In Chapter 5 use model solutions given by

$$U_{ij}(q) = \frac{1}{\ell}\int_{x_i}^{x_i+\ell} \tilde{u}^N(t_j, x, 0; q)\, dx \tag{A.14}$$

where $\tilde{u}^N(t,\vec{x};q)$ is the finite element solution of (5.12). The sensivities of $U_{ij}(q)$, which we will denote $V_{ij}^q(q)$ are then given by

$$V_{ij}^q(q) \;=\; \frac{\partial U_{ij}(q)}{\partial q} = \frac{\partial}{\partial q}\left(\frac{1}{\ell}\int_{x_i}^{x_i+\ell} \tilde{u}^N(t_j,x,0;q)\,dx\right) = \frac{1}{\ell}\int_{x_i}^{x_i+\ell}\frac{\partial}{\partial q}\left(\tilde{u}^N(t_j,x,0;q)\right)\,dx$$

$$=\; \frac{1}{\ell}\int_{x_i}^{x_i+\ell}(\tilde{v}^q)^N\,dx.$$